Université de Montréal
et
Université de Provence

Distribution de la matière sombre dans les galaxies spirales

par
Sébastien Blais-Ouellette
Département de physique
Faculté des arts et des sciences
et
Observatoire de Marseille

Thèse présentée à la Faculté des études supérieures
en vue de l'obtention du grade de
Philosophiæ Doctor (Ph.D.)
en physique
et de
Docteur de l'Université de Provence

Juin, 2000

Université de Montréal
Faculté des études supérieures
et
Université de Provence

Cette thèse intitulée:

Distribution de la matière sombre dans les galaxies spirales

présentée par:

Sébastien Blais-Ouellette

a été évaluée par un jury composé des personnes suivantes:

Daniel Nadeau,	président-rapporteur
Claude Carignan,	directeur de recherche
Philippe Amram,	codirecteur
Jacques Boulesteix,	membre du jury
Joss Bland-Hawthorn,	examinateur externe

Thèse acceptée le: .....

Sommaire

Cette étude a pour objet central la distribution de la masse obscure dans les galaxies spirales. Utilisant l'exemple de NGC 5585, il est d'abord montré l'impact de la résolution spatiale insuffisante dans les observations radio en synthèse d'ouverture, observations jusqu'à maintenant tenues pour suffisamment précises et fiables. À l'aide d'observations Fabry-Perot de haute résolution, nous observons une correction importante de la partie montante de la courbe de rotation et par conséquence un changement majeur dans l'importance relative des composantes sombre et lumineuse dans la galaxie.

À partir de ce résultat, une étude systématique d'une dizaine de galaxies spirales est faite en ajoutant des observations Fabry-Perot aux données radio existantes. Une technique d'une grande malléabilité permet de modéliser la masse dans ces galaxies en utilisant diverses formes de halo sombre en plus des composantes gazeuse et stellaires.

Il apparaît clairement que les halos prédits par les simulations de l'évolution cosmologique de la masse sombre froide ne peuvent expliquer la dynamique actuelle des galaxies spirales tardives. En fait, la compatibilité cesse pour des galaxies ayant des vitesses de rotation inférieures à 100 $\mathrm{km\,s^{-1}}$ suggérant que les trop grandes densités centrales des simulations sont détruites par un phénomène inhibé par un grand potentiel gravitationel.

Par ailleurs, une théorie alternative à la masse obscure, la gravité newtonienne modifiée, apparaît incompatible avec les nouvelles données, ne pouvant expliquer les courbes de rotation de près de la moitié des galaxies de l'échantillon.

De plus, plusieurs corrélations apparaissent entre les paramètres de la modélisation de masse. Entre autres, il existe une relation directe entre la densité centrale des halos et leur rayon de coeur, deux paramètres jusqu'alors considérés comme indépendants. La distribution de la masse sombre peut donc être décrite par un seul paramètre.

Remerciements

Pour la confiance qu'ils m'ont accordée, pour m'avoir communiqué l'enthousiasme dans la rigueur, la puissance de l'intuition et la passion de savoir, je me dois de remercier mes directeurs de thèse, Claude Carignan et Philippe Amram.

Pour le plaisir des discussions enflammées et pour l'entraide des moments moins faciles, pour l'amitié, merci à Cédric, Malvina, Caroline, Marc, Marie-Claude, Jocelyn, René, Olivier, Loic, Luc et à tous mes collègues dont l'appui m'a été plus que précieux.

Merci à Christiane, à Yvon, qui m'ont permis non seulement d'être mais surtout d'être heureux.

Merci à Juan Jose Cobo, pour la soif de la connaisance et le goût de la science.

Et enfin, merci à Isabelle pour l'appui indéfectible dans les moments de grands doutes, pour le bonheur de vivre à ses côtés, pour l'amour. Merci d'exister.

Table des matières

Sommaire iii

Remerciements i

Liste des tableaux v

Liste des figures vii

Abréviations xi

Introduction 1

Les moyens d'observation 3

Cette thèse 4

1 L'instrument 6

1.1 L'interféromètre Fabry-Perot 6

1.1.1 L'optique 6

1.1.2 De l'image au spectre 7

1.1.3 Jouer de finesse 9

1.1.4 Le résultat 12

1.2 L'image prend forme 14

1.2.1 L'usuel 14

1.2.2 Les rayons cosmiques 14

1.2.3 Ciel nocturne 15

1.2.4 Corrections photométriques 15

1.2.5 L'origine replacée 17

1.2.6 En termes de vitesse 18

1.2.7 La courbe de rotation 19

1.2.8 Au télescope 20

2 Observations Fabry-Perot de NGC 5585 **22**

2.1 Introduction 24

2.2 Importance of the Rising Part of the Rotation Curve on the Parameters of the Mass Distribution 26

2.2.1 The Case of NGC 5585 26

2.2.2 The Case of NGC 3198 26

2.3 Fabry–Perot Observations and Reduction 29

2.3.1 Data analysis 30

2.4 HII Kinematics and Optical Rotation Curve 33

2.5 Mass Models and Parameters of the Mass Distribution 35

2.5.1 Mass Model from the Hα Rotation Curve 35

2.5.2 Mass Model from the Combined HI and Hα Rotation Curve 36

2.6 Summary and Conclusions 38

3 Déterminer la forme des halos sombres **41**

3.1 Introduction 43

3.2 New Fabry–Perot Observations 44

3.2.1 NGC 3109 45

3.2.2 IC 2574 48

3.3 Mass Models and Parameters of the Mass Distribution 50

3.3.1 Comparison of different models using standard gravity 50

3.3.2 Modified Newtonian Dynamics 57

3.4 Summary and Discussion 60

3.5 Conclusion 61

4 Agrandir l'échantillon **64**

4.1 Introduction 66

4.2 The Sample 67

4.3 Fabry–Perot Observations: Data Acquisition and Reduction 68

4.4 UGC 2259 70

4.5 NGC 2403 71

4.6 NGC 6946 77

4.7 NGC 5055 78

4.8 NGC 2841 79

4.9 NGC 5985 81

4.10 Discussion and Summary 81

4.11 Conclusions 82

5 MOND et les halos sombres à l'épreuve **85**

5.1 Introduction 87

5.2 MULTI-WAVELENGTH ROTATION CURVES 88

5.3 Mass models 94

5.3.1 CDM halos 94

5.3.2 MOND 98

5.4 Trends and Correlations 101

5.4.1 Halo Parameters 101

5.4.2 Dark Matter vs Luminous matter 104

5.5 Discussion and Summary 104

5.6 Conclusion 106

Conclusion **109**

Annexe **112**

A Tableaux reportés **112**

Liste des tableaux

I Parameters of the mass models of NGC 3198. 29

II Optical parameters of NGC 5585. 31

III Parameters of the Fabry–Perot observations. 32

IV Parameters of the mass models of NGC 5585. 38

V Parameters of the Fabry–Perot observations. 44

VI Parameters of NGC 3109. 45

VII Optical parameters of IC 2574. 48

VIII Parameters of the mass models 57

IX MOND parameters when using the best fitted a_0. 58

X Parameters of the sample. Columns 4,5,6,10 and 11 from the main reference unless otherwise specified. 67

XI Parameters of the Fabry–Perot observations. 69

XII Beam–to–galaxy size and beam smearing importance. R_B is the ratio between the Holmberg radius and the beam width while R_{vdB} is the scale length over the beam width. ΔV_{max} is the maximum velocity difference between the Hα and HI data in the rising part of the rotation curve. 82

XIII Parameters of the sample (including the galaxies from Paper I and II). From the main references unless specified. 89

XIV Parameters of the mass models 98

XV MOND parameters when using the best fitted a_0. 101

XVI Optical rotation curve of NGC 5585 at 5″ binning 112

XVII Optical rotation curve of NGC 3109 at 20″ binning from ROCUR. The two sides and the global rotational velocities are computed indlependently. The latter are corrected for asymetric drift. 114

XVIII Optical rotation curve of IC 2574 at 9.4″ binning from ADHOC. The two sides are computed independently and the total is their mean averaged by the number of points. The velocity dispersion and the number of points appear for both sides while the error is the two σ/N added in quadrature. 115

XIX Optical rotation curve of UGC 2259 at 2.6″ binning. 118

XX Optical rotation curve of NGC 2403 at 6.6″ binning. 119

XXI Optical rotation curve of NGC 6946 at 4.4″ binning. 122

XXII Optical rotation curve of NGC 5055 at 2.2″ binning. 125

XXIII Optical rotation curve of NGC 2841 at 4.4″ binning. 130

XXIV Optical rotation curve of NGC 5985 at 4″ binning. 132

XXV HI rotation curve of NGC 5985 at ∼10″ binning (30″ resolution). 134

Liste des figures

1 Parcours détaillé d'un rayon lumineux. 8

2 Fonction d'Airy. Les différentes courbes correspondent à différentes valeurs de finesse. 8

3 Présence simultanée de deux ordres d'interférence. Les deux systèmes sont séparés par n x ISL + ϵ'. 9

4 Schéma de la bande passante du filtre interférentiel et du Fabry-Perot. Le continuum transmis par le FP pour chaque canal est $\Delta L/\delta\lambda$ fois plus petit que celui transmis par le filtre. En résulte un pouvoir accru de détection monochromatique. 10

5 Illustration d'un profil créé en un pixel par la juxtaposition des canaux balayant l'intervalle spectral libre (Amram, 1991). 13

6 Superposition des anneaux provenant des raies OH à l'image de la galaxie. 16

7 *Top:* Best fit mass model for NGC 5585 using the HI rotation curve. The model parameters are: $(\mathcal{M}/\mathrm{L}_B)_\star = 0.3$, r_c 2.8 kpc and $\sigma = 53$ $\mathrm{km\,s^{-1}}$. *Bottom:* Dark–to–luminous mass ratio as a function of radius. 27

8 *Top:* Maximum disk mass model for NGC 5585, where the first two points of the HI rotation curve have been given zero weight. The model parameters are: $(\mathcal{M}/\mathrm{L}_B)_\star = 1.0$, $r_c = 3.5$ kpc and $\sigma = 52$ $\mathrm{km\,s^{-1}}$. *Bottom:* Dark–to–luminous mass ratio as a function of radius. 27

9 Best fit mass model for NGC 3198 using the HI rotation curve (Begeman, 1989), corrected for beam smearing. The model parameters are: $(\mathcal{M}/\mathrm{L}_B)_\star = 9.4$, $r_c = 17.2$ kpc and $\sigma = 85.6$ $\mathrm{km\,s^{-1}}$. 28

10 Best fit mass model for NGC 3198 using the HI (filled circles) rotation curve (Begeman, 1989) and the Hα (open circles) rotation curve (Corradi et al., 1991). The model parameters are: $(\mathcal{M}/\mathrm{L}_B)_\star = 8.5$, $r_c = 11.7$ kpc and $\sigma = 79.0$ $\mathrm{km\,s^{-1}}$. 28

11 Best fit mass model for NGC 3198 using the HI rotation curve of Bosma (1981), not corrected for beam smearing. The model parameters are: $(\mathcal{M}/\mathrm{L}_B)_\star = 2.8$, $r_c = 3.9$ kpc and $\sigma = 83.4$ $\mathrm{km\,s^{-1}}$. 30

12 *Left,* Real reflection of a star; *top right,* cut along the y axis of the real reflection; *bottom right,* cut along the y axis of the simulated reflection. . . 32

13 Velocity field and Hα image of NGC 5585. The X and the grey line indicate the kinematic center and the axis of separation between the approaching and receding sides. 34

14 Optical rotation curve of NGC 5585. 35

15 Best fit mass model for NGC 5585 using the Hα rotation curve at 5 $''$resolution. The model parameters are: $(\mathcal{M}/L_B)_\star = 0.8$, r_c =3.7 kpc and $\sigma = 48$ km s^{-1}. 37

16 Adopted best fit mass model for NGC 5585 using the Hα rotation curve for r $< 120''$ and the HI rotation curve for r $> 120''$. The model parameters are: $(\mathcal{M}/L_B)_\star = 1.0$, $r_c = 4.3$ kpc and $\sigma = 53.6$ km s^{-1}. 37

17 Velocity field and Hα image of NGC 3109. North is up and East is left. The X and the grey line indicate the kinematic center and the axis of separation between the approaching and receding sides. 46

18 *Top* Hα rotation curve of NGC 3109 (open circles) compared to the HI rotation curve (filled circles) from Jobin & Carignan (1990). The approaching and receding sides are respectively represented by the dashed and continuous lines; *bottom* variation of the position angle and inclination for the Hα curve. See text for details on curves and error bars. 49

19 Velocity field and Hα image of IC 2574. North is up and East is left. 51

20 Hα rotation curve of IC 2574 (open circles) compared to the HI rotation curve (filled circles) from Martimbeau et al. (1994). The approaching and receding sides of the Hα curve are respectively represented by the dashed and continuous lines. 52

21 Density profiles of the four models. *solid*: pseudo-isothermal sphere, *dot*: KKBP, *long dash*: Burkert, *short dash*: NFW. 53

22 Best fit mass models for NGC 3109 using the Hα rotation curve up to 2.7 kpc and the HI rotation curve for the rest. The dark halos density profiles are *top–left*: pseudo-isothermal sphere, *top–right*: KKBP, *bottom–left*: Burkert, *bottom–right*: NFW. 54

23 Mass models of IC 2574 using the HI rotation curve only. 54

24 Mass models of NGC 5585 using the Hα rotation curve up to 3.5 kpc and HI for the rest. 55

25 Mass models of NGC 3198 using the Hα rotation curve up to 2.9 kpc and HI for the rest. 55

26 Best fit mass models using the Modified Newtonian Dynamics. Four different values of a_0 are used. Dotted line: 1.2 $\times 10^{-13}$ km/s^2 (from Begeman et al., 1991), continuous line: best fit value (see Table IX), short dash: cH_0 = 6.8 $\times 10^{-13}$ km/s^2 and long dash: $c^2\sqrt{\Lambda}$ = 7.8 $\times 10^{-13}$ km/s^2. The filled circles represent the data used in the fits (HI +Hα for NGC 3109 and 5585 and HI only for IC 2574 and NGC 3198). The open circles indicates the Hα velocities unused in the fits. 59

27 Hα rotation curve of UGC 2259 (open circles) Approaching and receding sides from Hα data are indicated respectively by the dashed and continuous lines. The filled circles represent the HI rotation curve from Carignan et al. (1988). 70

28 Monochromatic images of the Hα flux of UGC 2259, NGC 2403 and NGC 6946. Noth is up, East is left. 72

29 Velocity fields of the same galaxies.The X and the grey line indicate the kinematic center and the axis of separation between the approaching and receding sides. 73

30 Monochromatic images of the Hα flux of NGC 5055, NGC 2841 and NGC 5985 74

31 Velocity fields of the same galaxies. The reddest part of NGC 2841 is based on [NII] (λ6548) (*see text*). 75

32 Rotation curves of UGC 2403. 76

33 rotation curve of NGC 6946 77

34 Rotation curves of NGC 5055. 78

35 Rotation curves of NGC 2841. 79

36 Hα Rotation curves of NGC 5985. 80

37 Decomposition of the brightness profile of NGC 5055. The dashed curve represents the final profile of the bulge contribution while the dotted line shows the fit to the disk profile. 91

38 Decomposition of the brightness profile of NGC 2841. The dashed curve represents the final profile of the bulge contribution while the dotted line shows the fit to the disk profile. 92

39 Decomposition of the brightness profile of NGC 5985. The dashed curve represents the final profile of the bulge contribution while the dotted line shows the fit to the disk profile. 93

40 Mass model of UGC 2259. The fit gives a unrealistic value of $(\mathcal{M}/L_B)_\star = 0$ for the disk. 94

41 Mass model of NGC 2403 95

42 Mass model of NGC 6946 95

43 Mass model of NGC 5055 96

44 Mass model of NGC 2841 96

45 Mass model of NGC 5985 97

46 Permitted inner logarithmic slope (γ) of the CDM halos. Start of arrows give the maximum allowed value at a 95% confidence level. Note that most of the N-body simulations give $\gamma \geq 1$. NGC 5055 has a maximum γ well above 2.5 and is not plotted. 99

47 Mass models using MOND law with $a_0 = 1.2 \times 10^{-13}$ (dotted line) and best fit a_0 (continuous line). The Newtonian contributions of the disk, bulge and gas are represented in blue, cyan and green respectively. 100

48 *Top:* MOND characteristic surface density ξ vs central surface brightness. a_0 is fixed at 1.2×10^{-10} m/s^2(Begeman et al., 1991); *middle:* same but the best fit value of a_0 is used; *bottom:* variation of the best fitted a_0 with the surface brightness. 102

49 Characteristic (central) density (ρ_0) vs characteristic (core) radius (r_0), taken as the two "independent" parameters in the mass models. 103

50 *Top:* the inner slope of the rotation curve vs surface brightness; *bottom:* the inner slope vs absolute magnitude 105

Abréviations

ADHOC	Analyse et Dépouillement Homogène des Observations Cigale
AIPS	Astronomical Image Processing System
AT	Australia Telescope
CCD	Charge Coupling Device
CDM	Cold Dark Matter
CFHT	Télescope Canada-France-Hawaï
DAO	Dominion Astrophysical Observatory
DDO	David Dunlap Observatory
FCAR	Fond pour la Formation des Chercheurs et l'Aide à la Recherche
FP	Fabry-Perot
FSR	Free Spectral Range
GHASP	Gassendi observations of Hα in SPiral galaxies
i	Inclination
IRAF	Image Reduction and Analysis Facility
ISL	Intervalle Spectral Libre
MACHO	MAssive Compact Halo Objects
$(\mathcal{M}/L_B)_\star$	Ratio Masse-Luminosité dans la bande Bleue
MOND	MOdified Newtonian Dynamics

MOS Multi-Object Spectrograph

MOSFP Multi-Object Spectrograph Fabry-Perot

NGC New General Catalog

NSERC Natural Sciences and Engineering Research Council of Canada

PA Position Angle

pc Parsec

pixel Picture Element

UGC Uppsala General Catalog

VLA Very Large Array

WIMPS Weakly Interactive Massive Particles

WHISP Westerbork observations of neutral Hydrogen in Irregular and SPiral galaxies

WSRT Westerbork Radio Synthesis Telescope

À mes étoiles à moi, Marie, Isabelle.

Introduction

Deux concepts clés sont à la base du paradigme actuel de la naissance et de l'évolution de notre univers. La découverte de l'expansion universelle (Hubble, 1929), fruit du Big Bang, et de l'existence d'une quantité importante de matière sombre et froide, dominant de beaucoup la masse baryonique à l'échelle de l'Univers, ont mené à un modèle cosmogonique cohérent. Cependant l'existence de cette matière sombre ne s'est révélée que graduellement, suivant l'évolution technologique des instruments d'observation. Sa nature exacte est devenue aujourd'hui un des sujets les plus épineux et fascinants de l'astrophysique contemporaine.

La mention la plus ancienne d'une divergence significative entre la masse dynamique et la masse lumineuse remonte à Zwicky (1933) qui, par la grande dispersion des vitesses des galaxies membres de l'amas de Coma, a déduit que la masse totale devrait être près de 50 fois la masse visible dans l'amas. Néanmoins, l'omniprésence de cette masse invisible n'a été réalisée qu'avec l'avènement des radiotélescopes possédant une résolution spatiale suffisante pour déterminer la vitesse de rotation des galaxies spirales proches à différents rayons et au-delà du disque optique. Freeman (1970) a entre autres montré que la rotation de NGC 300 et de M 31 ne suivait pas la décroissance quasi-képlerienne attendue d'un disque exponentiel. Parallèlement à ces découvertes et à d'autres observations à plus grande résolution (Rogstad and Shostak , 1972; Roberts and Rots , 1973), des simulations numériques Ostriker & Peebles (1973) montrèrent l'instabilité intrinsèque d'un disque galactique en rotation. Ils proposèrent, pour une stabilité accrue, l'ajout d'un halo sphéroïdal englobant le disque. Il n'en fallait pas plus pour identifier ces halos à la matière sombre et mettre au jour la conception actuelle de l'évolution de l'Univers.

S'il est maintenant généralement accepté que la masse sombre joue un rôle critique dans l'évolution cosmologique, sa nature demeure insaisissable. À ce jour, trois classes d'hypothèses attirent l'attention des chercheurs: (1) de la matière baryonique "ordinaire", sous forme d'objets compacts et sombres, forme l'essentiel de la masse sombre, (2) les lois de la gravité ne tiennent plus à l'échelle des galaxies, (3) la masse manquante est composée

de matière exotique, dont l'existence n'est encore qu'hypothétique.

La première proposition suppose l'existence d'astres de faible luminosité, tels les naines brunes, de vieilles naines blanches ou de mini trous noirs qui, sans avoir été directement détectés, pourraient représenter une fraction importante de la masse totale d'une galaxie. La densité totale de matière baryonique dans l'univers est toutefois limitée par la nucléosynthèse primordiale et par l'abondance actuelle de certains éléments de sorte que si l'ensemble de la masse sombre de l'univers était formée de baryons, notre compréhension même des mécanismes liés à sa naissance devrait être révisée. De plus, il existe une façon indirecte de détecter la présence de ces astres sombres. Lorsqu'un de ceux-ci se retrouve entre une étoile et nous, sa masse attirant la lumière, il agit telle une lentille, amplifiant pour nous momentanément la lumière de l'étoile. Mais de récentes études à grand déploiement comme l'expérience MACHO (Alcock et al. , 2000), ont montré que ces astres seuls ne peuvent expliquer que près de 30% de la masse sombre de notre propre galaxie.

La seconde hypothèse invoque des changements fondamentaux dans les lois qui gouvernent la gravité. Sous cette perspective, la masse sombre n'existe pas. C'est plutôt la relativité générale ou plus simplement la gravité newtonienne qui est modifiée pour augmenter la force gravitationnelle à grande échelle. Parmi ces propositions, la plus en vogue est certainement la "MOdified Newtonian Dynamics" (MOND Milgrom, 1 983b) qui prescrit une force de gravité indépendante du rayon pour de très faibles accélérations. Cette nouvelle loi peut s'interpréter aussi bien par une modification de la force que par un changement de l'inertie. Il ne s'agit par contre que d'une prescription adhoc qui ne s'inscrit encore dans aucune théorie générale de la gravité. De plus, ses prédictions à l'échelle des grandes structures de l'univers ou face à l'évolution cosmologique n'ont jamais été clairement confirmées.

La dernière hypothèse, la plus généralement véhiculée, stipule que cette masse sombre serait en fait constituée d'hypothétiques particules fondamentales. Ces objets n'auraient que peu d'interactions avec la matière ordinaire sinon par la force gravitationnelle via leur masse relativement importante, d'où leur nom générique de "Weakly Interactive Massive Particules" (WIMPs). Un des candidats les plus prometteurs est issu d'une extension du modèle standard subatomique qui prévoit, par la supposition d'une symétrie additionnelle, un partenaire dit supersymétrique à chaque particule du monde ordinaire. Parmi ces particules supersymétriques, les neutralinos sont à la fois massifs et neutres et conviendraient parfaitement au rôle joué par les WIMPs. Ces particules primordiales, nées du Big Bang, composeraient la majeure partie de la masse de l'univers connu.

Selon la théorie la plus vraisemblable, la phase expansioniste de l'Univers l'a laissé

très homogène sauf pour quelques légères mais essentielles fluctuations. Vue la nature exclusivement attractive de la gravité, cette distribution initialement uniforme de la matière aurait eu tôt fait de se morceler et de se condenser autour de ces légères surdensités. Comme l'univers est à ce moment en pleine expansion, sa densité décroît rapidement. Les premiers halos à se former sont donc plus denses et plus petits que les plus tardifs. Ces halos se seraient par la suite fusionnés suivant un processus hiérarchique où les petits ensembles en forment de plus grands qui à leur tour en forment de plus importants encore. C'est au coeur de ces surdensités que la matière baryonique se serait vue gravitationnellement entraînée et accumulée pour former les structures célestes aujourd'hui observées.

Comme le montrent les simulations numériques (e.g. Navarro et al., 1996b), plusieurs facteurs peuvent influencer le processus d'évolution cosmologique. La constante de Hubble, le spectre de puissance des fluctuations initiales et le taux d'accélération de l'expansion, incluant l'importance de la constante cosmologique, influent de façon importante sur la distribution en taille des halos de même que sur leur section efficace de rencontre. Toutes les simulations récentes montrent une évolution similaire. Dans les grands amalgames créés par la fusion hiérarchique, les petits halos, plus denses, ont tendance à "couler" vers le centre, créant des surdensités abruptes au coeur des halos (éventuellement des galaxies). De plus, en chaque grand halo, un nombre important de sous-structures persistent. Ces structures sont perçues comme les précurseurs des galaxies satellites observées autour de galaxies massives telle la Voie Lactée. Les observations montrent toutefois que le nombre de satellites est insuffisant par près d'un facteur 10. Il s'agit là d'un des deux problèmes majeurs auxquels fait face le scénario actuel. L'autre problème étant central à la présente étude, il y sera traité en détail.

Les moyens d'observation

Depuis 30 ans, les progrès de la radio-astronomie en synthèse d'ouverture ont permis l'observation, dans les galaxies spirales, de la cinématique de la composante d'hydrogène neutre (HI) dont le disque s'étend bien au-delà du disque lumineux. Cela permet de sonder le potentiel gravitationnel dans une région presque exempte de matière lumineuse où l'effet de la matière sombre est des plus dramatiques: au lieu de suivre une courbe Képlerienne descendante, les vitesses de rotation demeurent presque constantes même à plusieurs fois le rayon optique de la galaxie.

Ces courbes de rotation montrent que la matière lumineuse ne compte toujours

que pour peu dans la masse totale des galaxies. Si les parties internes des galaxies précoces et massives sont généralement dynamiquement dominées par les composantes stellaires, les galaxies naines irrégulières, à l'opposé, sont le plus souvent dominées par la matière sombre à tous les rayons (Carignan & Freeman, 1988). Les courbes de rotation de ces galaxies ne montent que très doucement, à l'image d'un corps solide en rotation, une indication que la densité centrale des halos est peu abrupte, sinon constante, en contradiction avec les simulations numériques.

Malheureusement, la résolution spatiale des observations radio ($\gtrsim$ 20 ″) est insuffisante pour établir avec confiance la cinématique des parties internes des galaxies. En effet, l'étalement du faisceau radio (ou "beam smearing") ne permet pas de bien distinguer les vitesses du gaz à différents rayons et cela peut artificiellement diminuer la pente interne des courbes de rotation. La façon la plus simple d'augmenter la résolution est d'observer la raie Balmer α (λ6562.8) de l'hydrogène ionisé en spectroscopie en longue fente ou mieux encore, en spectroscopie à intégrale de champ (Amram, 1991) à l'aide, par exemple, d'un interféromètre de type Fabry-Perot.

Cette thèse

Cette thèse a précisément pour but de mesurer, à l'aide d'observations Fabry-Perot, la cinématique à haute résolution d'un échantillon de galaxies spirales dont l'hydrogène neutre a déjà fait l'objet d'une étude cinématique.

Il s'agit ensuite d'estimer la part de chacune des composantes. Si les contributions des parties visibles sont directement déduites de leur ratio masse–luminosité (connu pour le gaz mais non pour les étoiles), un modèle est requis pour la contribution du halo de matière sombre car sa distribution est *a priori* inconnue. Ces modèles sont fournis par la théorie ou par les simulations cosmologiques et permettent ainsi de comparer ces simulations aux observations.

La thèse se divise en cinq parties. Dans le premier chapitre, l'instrument utilisé est décrit et les procédures de réduction de données sont expliquées. Le second chapitre est consacré aux galaxies spirales NGC 5585 et NGC 3198, de parfaits exemples de l'importance de l'effet de la résolution dans l'étude de la dynamique des galaxies. Deux autres galaxies spirales tardives, IC 2574 et NGC 3109, sont analysées au troisième chapitre. La modélisation y est élargie à plusieurs modèles de halo proposés dans la littérature et à l'utilisation d'une modification de la gravité (MOND) pouvant entre autres expliquer les courbes peu abruptes

des galaxies à faible brillance de surface (McGaugh & De Blok, 1998). Le chapitre quatre enrichit l'échantillon de six nouvelles galaxies qui se voient analysées au cinquième chapitre. Ce chapitre se consacre aussi à explorer la nature des corrélations, possiblement universelles (Persic et al., 1996), entre la distribution de la matière lumineuse et celle de la matière sombre. Suit la conclusion et les annexes contenant le détail des courbes de rotation des galaxies de l'échantillon.

Bibliographie

Alcock, C. and 59 colleagues 2000, ApJaccepted

Amram, P. 1991, PhD thesis, Université de Provence

Carignan, C. & Freeman, K. C. 1988, ApJ, 332, L33

Fukushige, T. & Makino, J. 1997, ApJ, 477, L9

Freeman, K. C. 1970, ApJ, 160, 811

Hubble,E. 1929, Proceedings of the National Academy of Sciences, 15, 168

McGaugh, S. S. & De Blok, W. J. G. 1998, ApJ, 499, 41

Milgrom, M. 1983, ApJ, 270, 365

Moore, B., Governato, F., Quinn, T., Stadel, J., & Lake, G. 1998, ApJ, 499, L5

Navarro, J. F., Frenk, C. S., & White, S. D. M. 1996, ApJ, 462, 563

—. 1997, ApJ, 490, 493

Ostriker, J. & Peebles, P. 1973, ApJ, 467

Persic, M., Salucci, P., & Stel, F. 1996, MNRAS, 281, 27

Roberts, M. S. and Rots, A. H. 1973, A&A, 26, 483

Rogstad, D. H. and Shostak, G. S. 1972, ApJ, 176, 315

Zwicky, F. 1933, Helv.Phys.Acta, 6, 110

Chapitre 1

L'instrument

1.1 L'interféromètre Fabry-Perot

Décrire en quelques pages toute la physique sous-jacente au fonctionnement du Fabry-Perot (FP) est une tâche illusoire dans le cadre de ce travail. Je m'attarderai donc davantage aux processus optiques macroscopiques dont découlent les propriétés de l'interféromètre. (Pour approfondir voir Vaughan, 1989; Hernandez, 1986; Reynolds, Develis & Thompson, 1989)

Le FP consiste, à la base, en deux lames semi-réfléchissantes parallèles recouvertes, sur leurs faces intérieures, d'un matériau ayant un facteur de réflexion élevé. Entre les deux se trouve un milieu d'indice de réfraction différent des lames, généralement de l'air.

1.1.1 L'optique

Pour obtenir une résolution spectrale uniforme sur un grand champ, le Fabry-Perot se doit d'être utilisé à l'infini. Pour une efficacité maximal au télescope, cela signifie l'utilisation d'un réducteur focal dont le faisceau parallèle est plus petit que l'étalon Fabry-Perot utilisé. Les lentilles L1 et L2 de la figure 1 agissent respectivement comme lentille de champ et de caméra, parties essentielles du réducteur focal.

La partie cruciale demeure évidemment l'étalon. La lumière pénètre par une des faces et est réfléchie plusieurs fois entre les lames. Chaque réflexion laisse s'échapper une fraction de la lumière et une interférence à ondes multiples a lieu entre tous ces rayons transmis déphasés de ϕ (figure 1).

La phase est égale à

$$\phi = \frac{2nd\cos\theta}{\lambda} * 2\pi,$$

où n est l'indice de réfraction, d la distance entre les lames et θ l'angle entre le rayon et la normale aux lames.

Elle sera identique pour chacun des rayons transmis lorsque le chemin optique parcouru entre les lames, $2nd\cos\theta$, sera un multiple entier de sa longueur d'onde. L'interférence y sera ainsi constructive, et la puissance transmise maximale.

Cela nous mène à l'équation fondamentale du FP: l'intensité transmise. Pour un étalon parfait, fait d'un matériau dont l'absorption est nulle, elle s'exprime comme,

$$I = \left(\frac{\tau}{1-\rho}\right)^2 \frac{1}{1+\frac{4F_\rho^2}{\pi^2}\sin^2\phi/2}$$

où τ est le coefficient de transmission, ρ le coefficient de réflexion et $F_\rho = \frac{\pi\sqrt{\rho}}{1-\rho}$ la finesse spatiale de l'interféromètre.

Elle sera maximale pour

$$\lambda p = 2nd\cos\theta$$

où p est un nombre entier représentant l'ordre d'interférence

À l'inverse, une distance parcourue multiple demi-entier de la longueur d'onde provoque des interférences destructives et un très faible taux de transmission.

L'énergie transmise maximale,

$$I_0 = (\frac{\tau}{1-\rho})^2$$

ne dépend que des coefficients de réflexion et de transmission.

1.1.2 De l'image au spectre

La fonction

$$\frac{1}{1+\frac{4F_\rho^2}{\pi^2}\sin^2\phi/2}$$

vue ci-haut n'est autre que la **fonction d'Airy** telle qu'illustrée à la figure 2. La phase, en abscisse, est déterminée par le chemin effectué par la lumière. Pour l'image d'une source monochromatique étendue et uniforme, seul l'angle d'éclairement fait varier ce chemin et crée, vue la symétrie axiale de l'étalon, un jeu d'anneaux concentriques. Alternativement, il est possible de balayer l'espace entre deux pics dit **intervalle spectral libre** ou **interfrange**, pour un angle fixe, en faisant varier la distance entre les lames (paramètre d ci-haut). Pour échantillonner le spectre, sont donc pris n interférogrammes, ou **canaux**, à intervalle d/n.

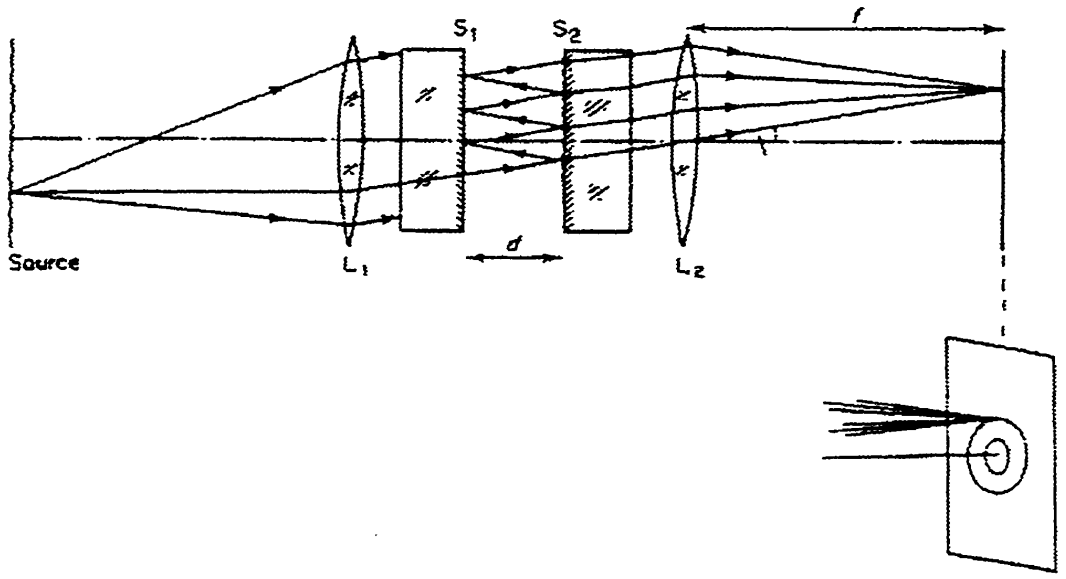

Figure 1: Parcours détaillé d'un rayon lumineux.

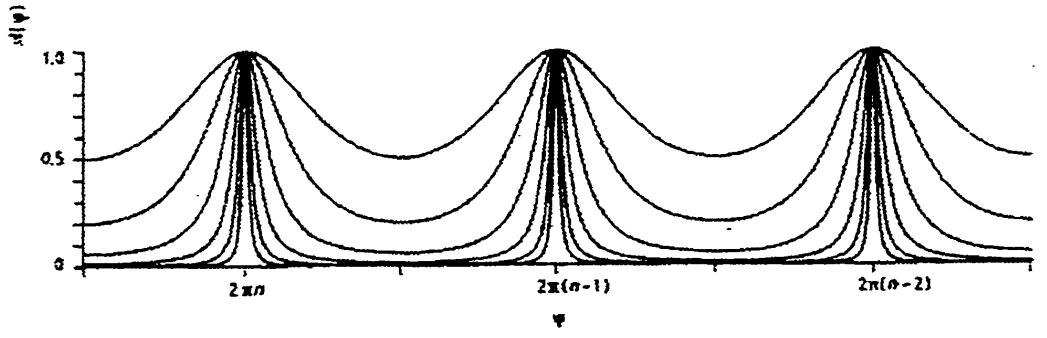

Figure 2: Fonction d'Airy. Les différentes courbes correspondent à différentes valeurs de finesse.

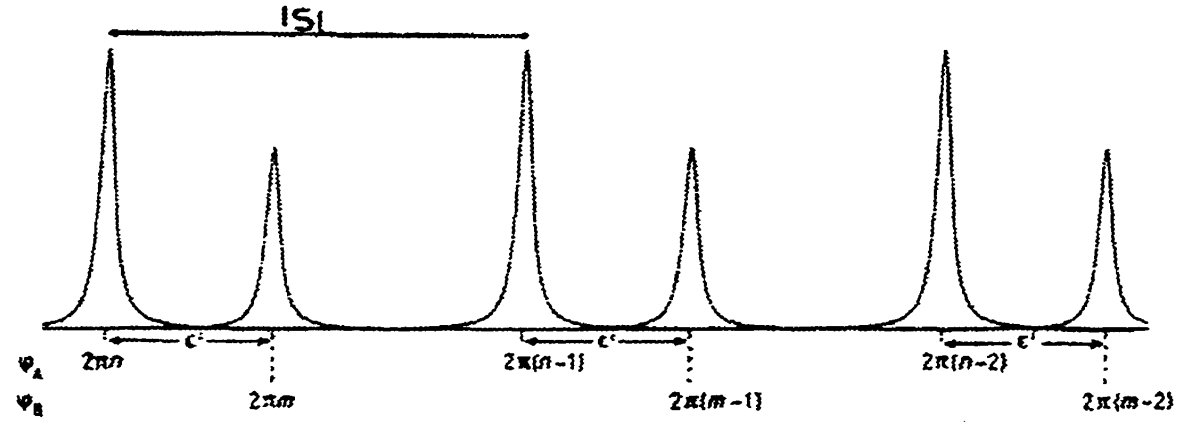

Figure 3: Présence simultanée de deux ordres d'interférence. Les deux systèmes sont séparés par n x ISL + ϵ'.

En procédant ainsi, on obtient, en chaque pixel, un spectre de la lumière émise en un point de la source. Cependant, comme un point-source n'est possiblement pas monochromatique, c'est plutôt la superposition des spectres de tous les ordres d'interférence qui apparaîtra sur l'appareil de mesure comme l'illustre la figure 3.

Pour isoler un seul intervalle spectral libre et ainsi lever l'ambiguïté sur l'ordre d'interférence, un filtre interférentiel dont la longueur d'onde centrale correspond à celle de la raie observée est installé en amont ou en aval de l'étalon. Le résultat en terme de bande passante est illustré à la figure 4.

Un effet pervers dû à la modulation du continuum par le filtre peut cependant apparaître si le continuum est important et si la largeur à mi-hauteur du filtre est comparable ou inférieure à l'intervalle spectral libre. Cette modulation de la lumière par le filtre crée l'équivalent d'une large raie d'émission. Celle-ci se superpose aux raies galactiques et peut rendre plus difficile la détermination des vitesses à partir des profils. Cependant, dans les cas qui nous occupent, le continuum est faible et le filtre est suffisament large et carré pour pouvoir négliger ces effets.

1.1.3 Jouer de finesse

Tout appareil de mesure ou de transformation de la lumière laisse sa trace en dégradant le signal lumineux, entre autres en laissant passer du "bruit" lumineux et en diminuant la résolution.

Le FP a plusieurs avantages et limitations lorsque vient le temps de comparer le rap-

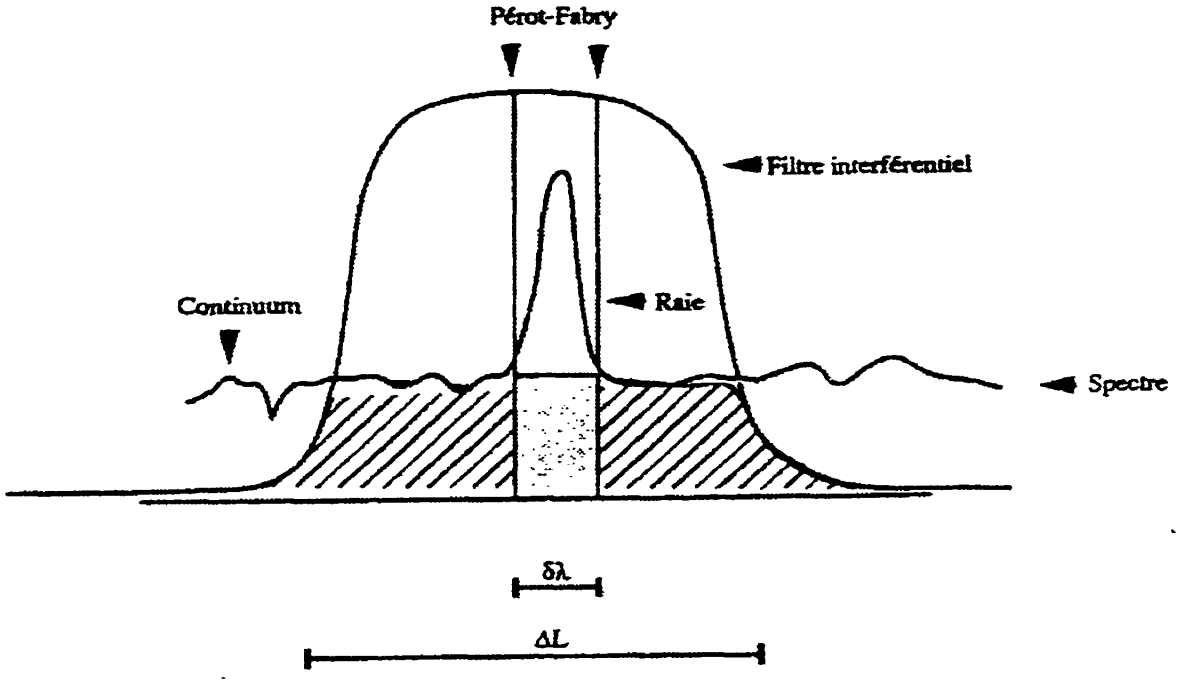

Figure 4: Schéma de la bande passante du filtre interférentiel et du Fabry-Perot. Le continuum transmis par le FP pour chaque canal est $\Delta L/\delta\lambda$ fois plus petit que celui transmis par le filtre. En résulte un pouvoir accru de détection monochromatique.

port signal sur bruit résultant de son utilisation à celui d'autres techniques spectroscopiques. Si on le compare aux spectrographes dispersifs, sa grande force est bien sûr d'avoir un spectre pour chacun des pixels de l'image plutôt que pour une ou plusieurs fentes sur le ciel. À titre de comparaison, pour obtenir un spectre d'une résolution donnée sur l'ensemble de l'image, un système FP balaiera une gamme de longueurs d'onde alors qu'il faudra déplacer la fente du spectrographe dispersif le long de l'image pour une couverture complète. À efficacité quantique et optique égale, le même temps devra être consacré à l'acquisition du cube (x,y,λ) de données avec les deux techniques (voir Bennett, 2000). Toutefois, étant donné la simplicité optique du FP, son efficacité est en principe beaucoup plus grande que le spectrographe conventionnel et, ajouté au fait que l'alignement successif précis des fentes sur le ciel est loin d'être trivial, le FP est un spectrographe à intégral de champ de beaucoup supérieur. Cela dit, si les objets d'intérêts sont dispersés dans le champ, il sera plus avantageux d'utiliser le spectrographe disperseur avec plusieurs fentes judiscieusement displosées.

Similairement, si on ne désire que quelques positions spectrales sur toute l'image, le FP procure un pouvoir de détection monochromatique non seulement plus élevé que le disperseur mais aussi plus élevé qu'un filtre à bande étroite (normalement plus large que la

bande passante du FP). En observant la figure 4, il est aisé de constater que pour une raie donnée, si seul était présent le filtre interférentiel, la lumière en un pixel proviendrait de la raie elle-même et du continuum de la largeur du filtre. La contamination de la raie serait donc proportionnelle à $\Delta L/\Delta\lambda$ où $\Delta\lambda$ est largeur de la raie d'émission. En ajoutant le FP, la largeur du continuum se réduit à n $\times\delta\lambda$ (ou n est le nombre d'ISL entrant dans le filtre et $\delta\lambda$ la bande passante du FP) et le bruit d'un facteur $\Delta L/n\delta\lambda$. À cela, il faut ajouter la possibilité d'ajuster le FP en longueur d'onde centrale et en bande passante, ce qui permet de centrer et de "résoudre" ou non la raie selon la nécessité.

Un autre facteur de dégradation de la qualité des spectres obtenus avec le FP est la variation continue de l'intensité du ciel nocturne dont les corrections sont traitées en détails à la section 1.2.4. Pour réduire cette source de bruit, l'idéal serait de prendre un grand nombre de spectres de courtes durées et ainsi moyenner les variations du ciel. Comme les observations FP sont typiquement de faible intensité, dû principalement à la bande spectrale très étroite, le bruit de lecture des détecteurs devient un élément décisif dans la qualité de l'information obtenue. Le rapport signal sur bruit peut s'écrire

$$\frac{S}{B} = \frac{\epsilon S}{\sqrt{\epsilon(S+C)+I_O}+n\times B_L}$$

où ϵ est l'efficacité quantique, S est le signal intégré de l'objet, C, celui du ciel, I_O, le courant d'obscurité, n, le nombre de poses et B_L, le bruit de lecture d'une pose. Avec les détecteurs refroidis d'aujourd'hui et les temps de pose d'au maximum quelques minutes, le courant d'obscurité peut être généralement négligé. Pour illustrer l'effet comparé du bruit de lecture et de l'efficacité quantique, le deux principaux types de détecteurs utilisé avec le FP sont pris en exemple. D'une part les CCD ont un haut rendement quantique (~80%) et un bruit de lecture d'au mieux 5 électrons pour un lecture relativement rapide. D'autre part les tubes à photocathodes ont un rendement quantique d'au plus 20% mais aucun bruit de lecture. Pour un rapport signal sur bruit de 3, en une seule pose et pour un bruit du ciel négligeable, le signal S nécessaire pour le CCD est de 40 photons alors qu'il en faut 45 pour le système à comptage. Par contre pour seulement deux séries de canaux, le signal nécessaire au comptage reste le même alors qu'il devient 64 pour le CCD. L'avantage des détecteurs à bruit nul pour une lecture répété apparaît donc clairement alors que les CCD sont plus performants pour une pose unique ou des flux plus élevés.

La résolution quant à elle dépend du rapport signal sur bruit et de la finesse. En effet, les défauts intrinsèques de l'étalon et la réflectivité limitée des lames élargissent la fonction d'Airy. La finesse se définit comme le rapport entre l'intervalle spectral libre et la

largeur à mi-hauteur de la raie d'Airy $\Delta_{ISL}/\delta\lambda$; la résolution en longueur d'onde est ainsi $R = \lambda/\delta\lambda = pF$.

Il existe plusieurs sources de dégradation de la finesse. Comme vu ci-haut, la finesse fonction de la réflectivité est

$$F_R = \frac{\pi\sqrt{\rho}}{1-\rho},$$

alors que celle qui relève de la planéité et du parallélisme des lames s'exprime comme,

$$F_D = \frac{\lambda}{2\delta d},$$

où δd est l'erreur quadratique moyenne sur l'espace d entre les lames.

et la finesse reliée au nombre fini de pixels est

$$F_I = \frac{1}{p \sin i \; \delta i}$$

où δi est le pouvoir de séparation angulaire du récepteur.

La finesse effective est ainsi donnée par

$$\frac{1}{F_E^2} = \frac{1}{F_R^2} + \frac{1}{F_D^2} + \frac{1}{F_I^2}$$

1.1.4 Le résultat

Sauf pour une particularité des couches diélectriques recouvrant les lames explicitée à la section 1.2.5, chaque espacement d entre les lames ne laisse passer qu'une longueur d'onde

$$\lambda = \frac{2nd\cos\theta}{p}$$

ne dépendant que de l'angle d'un point-source monochromatique. C'est ainsi qu'une source non uniforme n'éclairera qu'une partie du champ, son image, qui sera multipliée par le jeu d'anneaux correspondant à la longueur d'onde émise.

Une source telle une galaxie est cependant loin d'être une source monochromatique uniforme. Ainsi, chaque région émettant une longueur d'onde donnée sera multipliée par un jeu d'anneaux qui lui est propre. L'image finale sera donc formée de ces jeux d'anneaux superposés, modulés (encore!) par l'intensité de chaque point source.

En balayant un ISL entier, on obtient, en chaque pixel, un spectre de la raie émise en ce point source tel qu'illustré à la figure 5. Pour un échantillonnage suffisant, 2.2 x la finesse effective suivant le principe de Shannon (ou de Nyquist), il est possible d'obtenir une résolution élevée, de l'ordre de 15 000 à la raie Balmer α pour l'étalon principalement utilisé dans cette étude, sur un domaine spectral d'une dizaine d'Å.

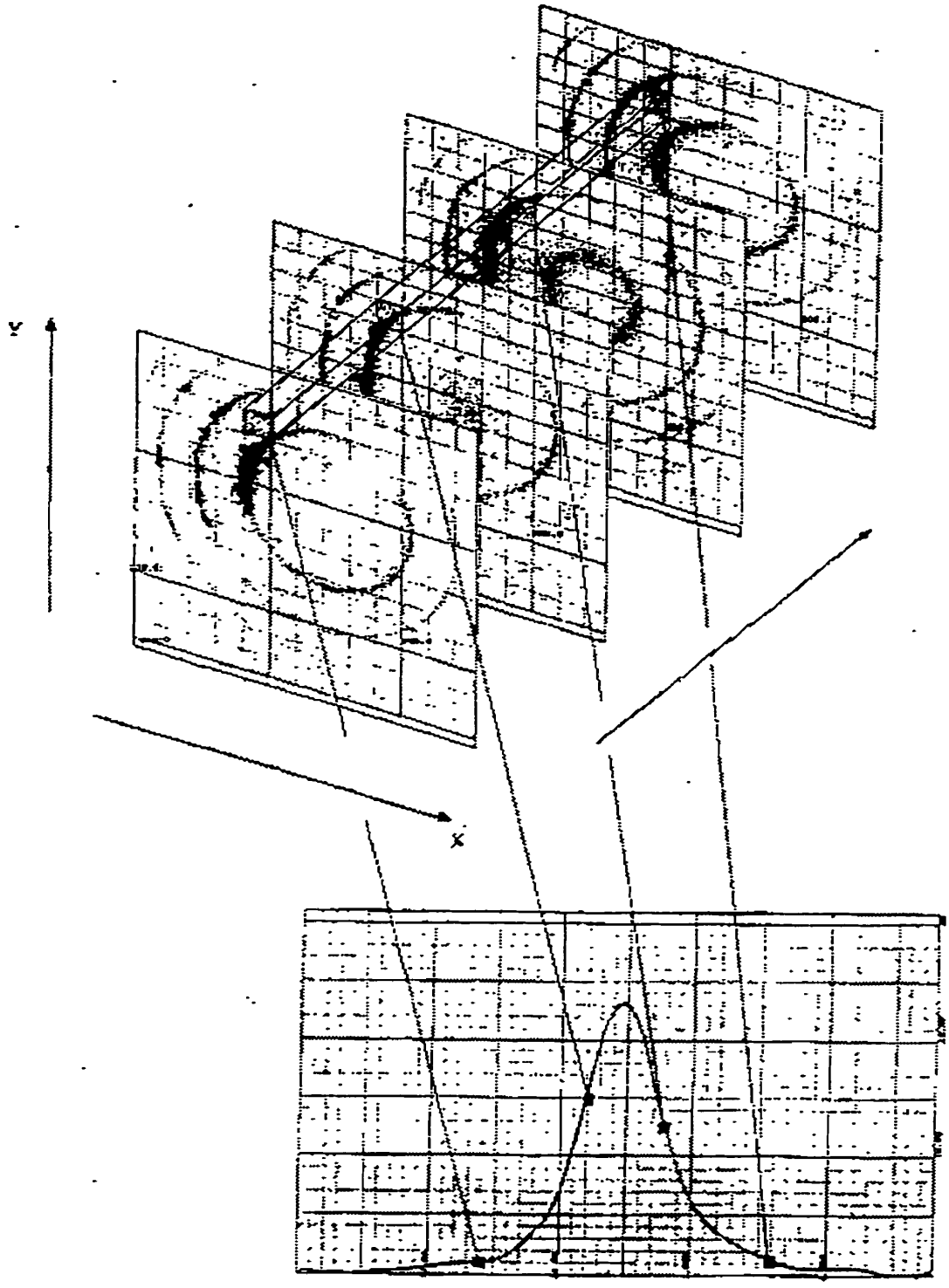

Figure 5: Illustration d'un profil créé en un pixel par la juxtaposition des canaux balayant l'intervalle spectral libre (Amram, 1991).

1.2 L'image prend forme

1.2.1 L'usuel

Soustraction du piédestal et division par le champ uniforme, voilà ce que, sous d'autres vocables, toute image doit subir pour minimiser les effets des biais du système opto-électronique d'acquisition utilisé dans cette étude. En effet, deux effets bien connus du CCD (Charge Coupling Device), un potentiel de départ en chaque pixel et une variation de sensibilité d'un pixel à l'autre nécessitent une correction.

Si la première opération se fait de la façon la plus régulière qui soit, la seconde nécessite quelques précisions du fait qu'elle peut se faire de plusieurs manières. En imagerie directe, le champ uniforme se prend sur le ciel de l'aube ou plus souvent, sur un écran éclairé par une lumière blanche étendue. Bien que ces sources soient suffisamment uniformes spatialement, elles contiennent le plus souvent des raies qui provoquent une structure annulaire sur chaque image. Il convient donc de prendre la moyenne d'une séquence couvrant un ISL pour obtenir une image représentative de la sensibilité du détecteur. Une autre solution consiste à retirer l'étalon du système optique, lequel, se trouvant dans le faisceau parallèle, n'induit de toute façon aucune dépendance spatiale dans l'intensité du faisceau. On gagne ainsi beaucoup de temps mais la première solution demeure préférable pour éviter tout changement dans l'appareil entre la prise des données et l'exposition au champ uniforme.

1.2.2 Les rayons cosmiques

Deux méthodes complémentaires rendent très efficace l'élimination des rayons cosmiques. La première, usuelle en imagerie, consiste à éliminer les pixels dont la différence en intensité avec les pixels adjacents est de plusieurs fois l'écart type de l'image. Cette méthode quoique relativement efficace, laisse passer plusieurs rayons cosmiques (entre autres ceux dont le signal est étendu sur plusieurs pixels).

La seconde méthode est similaire en ce qu'elle juge l'écart entre deux pixels mais cette fois de pixels adjacents sur le spectre plutôt que sur l'image, donc à la même coordonnée mais sur le canal qui précède ou qui suit. Comme il est très peu probable que deux rayons cosmiques arrivent au même endroit sur deux images subséquentes, cette façon de faire est très efficace même pour les cosmiques qui touchent plusieurs pixels.

En combinant les deux méthodes, il est possible d'éliminer la presque totalité des rayons cosmiques tout en étant tolérant sur l'écart permis et éviter ainsi d'exclure de bons

signaux.

1.2.3 Ciel nocturne

Les niveaux rotationnels des radicaux OH dont le ciel nocturne est peuplé causent une radiation polychromatique qui, à faible signal sur bruit, pollue le signal galactique. Ces radicaux s'assemblent en nuages stratifiés à quelque 85 km d'altitude et varient en forme et en intensité avec le temps, l'intensité augmentant avec l'épaisseur de l'atmosphère (elle évolue donc de façon inverse au signal). Le problème est ainsi amplifié lors de la correction pour la transparence du ciel. Si aucune correction photométrique n'est nécessaire, ces raies sont évaluées dans des régions éloignées de tout signal extra-atmosphérique et sont soustraites de l'ensemble de l'image (une fois la phase corrigée). Si, par contre, la photométrie nécessite quelques corrections, les deux phénomènes (corrections photométriques et raies du ciel) doivent être traités en parallèle.

1.2.4 Corrections photométriques

Le système interférométrique de Fabry-Perot est en fait un photomètre car on n'y mesure physiquement aucune position de raie mais plutôt des variations d'intensité dont sont déduites les longueurs d'onde des raies. Une normalisation photométrique de tous les canaux revêt donc une importance capitale.

Un désavantage du CCD par rapport à d'autres systèmes de moindre efficacité quantique (comme la caméra à comptage de photons) est son bruit de lecture non-nul qui rend très couteuses, en termes de rapport signal sur bruit, de courtes expositions répétées de la séquence entière des canaux. L'usage d'un système à comptage de photons permet de moyenner, par l'utilisation de cette méthode, les variations photométriques du ciel et de normaliser naturellement l'intensité des différents canaux. En CCD, il est donc nécessaire de corriger *a posteriori* les variations photométriques normalement en observant l'évolution du flux provenant d'étoiles de champs références.

Un grand nombre d'étoiles est cependant nécessaire pour obtenir une correction valable car les raies nocturnes, couvrant tout le champ, ont pour conséquence des anneaux d'interférence s'étendant sur l'ensemble de chaque image. Lors du balayage de l'interfrange, ces anneaux brillants font varier l'intensité des étoiles-étalons ne permettant l'utilisation de ces dernières pour la photométrie que si leur nombre est suffisant pour moyenner correctement les régions sombres et brillantes. À ceci on doit généralement ajouter la modulation dûe à la

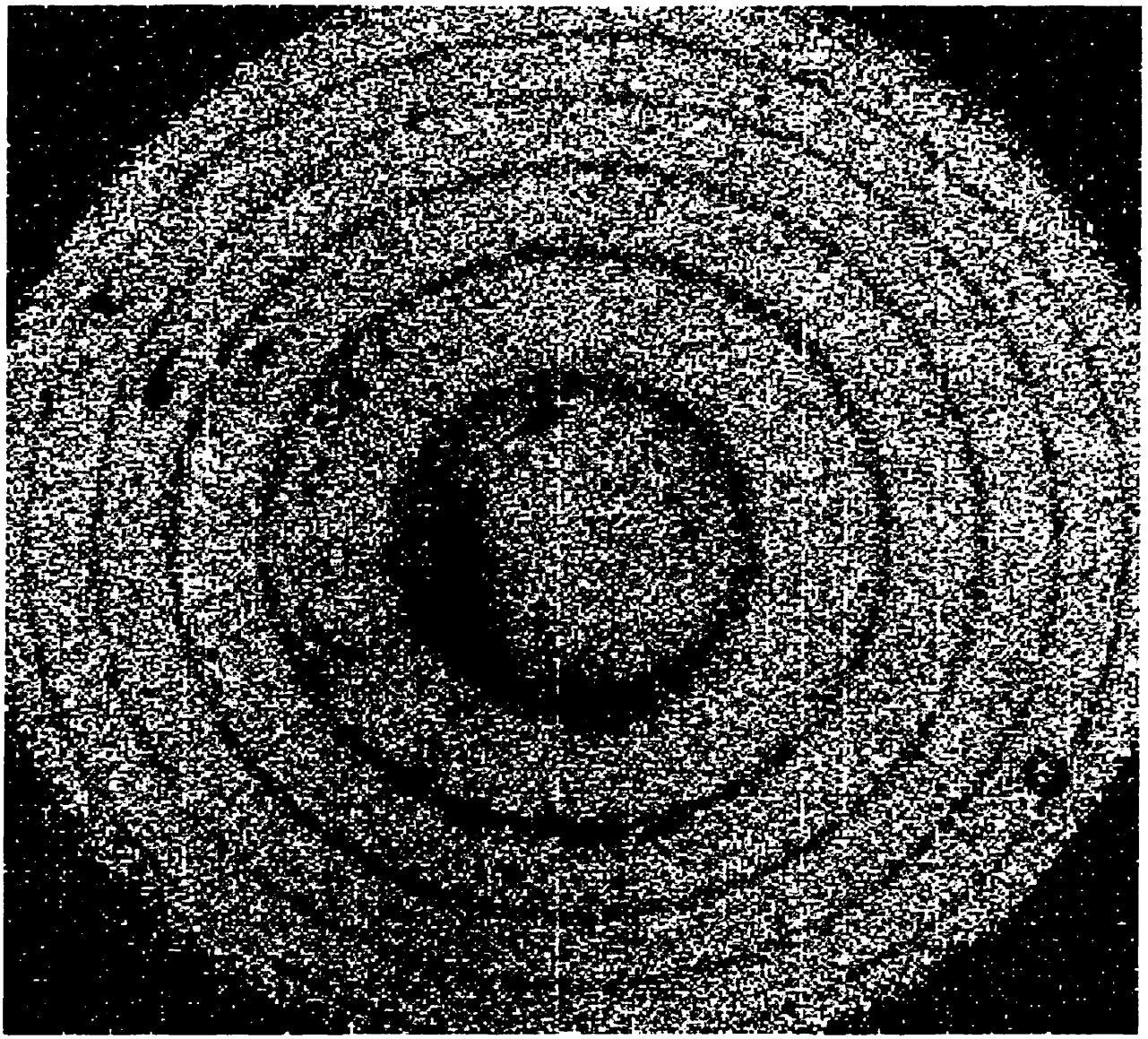

Figure 6: Superposition des anneaux provenant des raies OH à l'image de la galaxie.

bande passante finie du filtre, expliquée plus haut, qui peut ajouter à son tour une modulation annulaire de basse fréquence spatiale.

Pour faire ces corrections photométriques de façon plus efficace, une méthode simple consisterait à suivre le flux de l'étoile guide, dont le signal ne passe pas par le Fabry-Perot, à la même longueur d'onde que la raie observée. Ces variations pourraient être inscrites dans l'en-tête de chaque image et utilisées adéquatement lors du dépouillement. Un tel système est utilisé à l'observatoire Byurakan en Arménie avec un succès mitigé car il est en pratique très difficile d'observer l'étoile guide dans la même bande passante que l'objet d'étude.

Une alternative, développée au cours de cette thèse, consiste à d'abord soustraire les raies du ciel nocturne. Chaque image est divisée en anneaux de phase constante. L'intensité des raies nocturnes doit donc aussi être constante sur un anneau donné. En sommant les pixels d'un anneau qui sont exempts de signal autre que le ciel, on obtient l'intensité moyenne de la raie sur cet anneau. Il est donc maintenant aisé de soustraire ce signal parasite sur tout l'anneau y compris les régions couvrant l'objet d'étude. En répétant cela pour tous les anneaux, il en résulte des interférogrammes sans raies nocturnes et le flux des étoiles peut maintenant être utilisé pour corriger les variations de transparence du ciel. Cette méthode fonctionne si chaque anneau de phase constante possède une ou des régions de ciel pur. Cela pose évidemment problème si l'objet couvre le centre des anneaux.

Une autre alternative, développée par Jacques Boulesteix de l'Observatoire de Marseille, utilise les raies du ciel nocturne comme étalon de la transmission du ciel. En effet, si les radicaux OH progéniteurs des raies nocturnes sont situés au-delà des couches absorbantes de l'atmosphère, les raies devraient en moyenne varier selon la transparence du ciel. En mesurant l'intensité des raies dans des régions exemptes de signal extra-atmosphérique, il devient possible de normaliser le flux de l'ensemble des pixels. Il faut cependant garder en tête que la brillance du ciel varie de façon très différente de la transmission, souvent à l'inverse. Il faut donc qu'au moins une raie nocturne domine nettement le fond du ciel pour obtenir un correction valable.

1.2.5 L'origine replacée

L'origine en longueur d'onde du spectre obtenu en chaque pixel varie avec la distance parcourue par la lumière entre les lames de l'étalon. Comme cette distance augmente avec l'angle d'incidence, un retard variable de la phase de référence est introduit et demande à être corrigé pour déduire adéquatement les longueurs d'onde réelles des raies.

Une **carte de phase** est donc construite à partir d'une raie connue et stable. En mesurant la position observée de cette raie dans la séquence des canaux, nous identifions, en chacun des pixels, la longueur d'onde réelle d'un canal donné. Comme cette relation est différente pour chaque pixel, une matrice de la dimension de l'image contenant l'identification du canal de cette longueur d'onde est créée. Cette carte de phase est ensuite utilisée pour "rephaser" les observations et en faire de véritables **cartes en longueurs d'onde** où chaque canal nous image l'objet en une longueur d'onde très précise.

Si la raie d'étalonnage est près de la raie observée, cette méthode suffit à homogénéiser les origines des spectres. Il faut tout de même savoir que le Fabry-Perot introduit un autre effet de phase qui dépend cette fois uniquement de la longueur d'onde de la lumière incidente. Ce nouveau décalage spectral est dû au fait que la profondeur de pénétration dans les couches diélectriques qui recouvrent les lames semi-transparentes dépend de la longueur d'onde. Par conséquent, le chemin optique véritable dépend aussi de la longueur d'onde.

Ces couches diélectriques sont constituées d'une alternance de 5 couches de sphalérite (ZnS), de faible indice de réfraction, et de 4 couches de cryolithe (Na_3 Al Fe_6), d'indice élevé, et leur utilisation multiplie par trois l'efficacité du Fabry-Perot par rapport à des couches d'argent de même réflectivité. Chacune des couches a une épaisseur $\lambda_0/4$ élaborée pour mettre en phase les rayons qui la traversent depuis l'extérieur et ceux qui reviennent se réfléchir sur sa face intérieure. Ces multicouches se comportent donc comme une série de FP d'ordre 1. Lorsqu'on s'éloigne de λ_0, les rayons émergents ne sont plus en phase, un déphasage

$$\phi = 2n \cos\theta \frac{\lambda_0}{4\lambda}$$

qui dépend directement de λ_0/λ est introduit. Les corrections sont maintenant connues Le Coarer & Segrétain (1989) et incluses dans les programmes de correction de phase.

Une autre difficulté est introduite si un décalage spectral trop important est présent entre la raie observée et la raie d'étalonnage. Les couches diélectriques ne sont pas traversées aussi profondément par l'une et l'autre des raies et la distance effective entre les lames change avec la longueur d'onde. Heureusement, dans les cas qui nous intéressent, les raies d'étalonnage et les raies à l'étude sont suffisamment rapprochées pour pouvoir négliger ce problème.

1.2.6 En termes de vitesse

Une fois les profils débarrassés de leurs parasites, il reste à calculer la vitesse correspondante en chaque pixel contenant une raie émise par la galaxie. Sachant que

$$\frac{v}{c} = |\frac{\lambda - \lambda_0}{\lambda_0}|$$

où λ_0 est la longueur d'onde de la raie au repos et λ de la raie observée, v est la vitesse radiale et c la vitesse de la lumière,

tout le problème se résume à trouver la position précise de la raie. Deux méthodes s'offrent à nous pour y arriver: l'ajustement de fonctions théoriques telles des gaussiennes aux profils ou la détermination de barycentres pour ceux-ci. La première avenue est la plus sûre, si le rapport signal sur bruit le permet, car elle s'ajuste sur toute la raie. Malheureusement, l'échantillonnage minimal et le signal sur bruit mitigé ne nous permettent pas d'appliquer cette méthode en toute confiance.

C'est donc le calcul d'un barycentre qui sera retenu pour déterminer la vitesse associée. Le barycentre est calculé en divisant chaque pic (limité de chaque côté par un changement dans le signe de la pente du profil) en de petits éléments de surface. Le barycentre vérifie l'équation

$$A \cdot OP(x_b, y_b) - \sum_{i,j} a(i,j) \cdot OP(x_{i,j}, y_{i,j})$$

où A est l'aire de la raie, $a(i,j)$ celui de l'élément de surface i,j, O l'origine et P la position de l'élément considéré.

Pour ne conserver que les profils dont le signal sur bruit est suffisant, ne sont retenues que les raies dont l'ordonnée du barycentre est plus grande que $\alpha \times \sigma$ où σ est le bruit du continuum et α un paramètre arbitraire (au minimum 1.5).

1.2.7 La courbe de rotation

L'objet de l'étude en cours étant entre autres de déterminer la dynamique précise de galaxies spirales, l'information la plus intéressante ne réside pas tant en chacun des pixels pris individuellement mais en la cinématique globale des disques galactiques. Une fois que la vitesse du gaz a été mesurée en chaque élément de l'image, il est donc nécessaire de déterminer la vitesse de rotation de la galaxie à tout rayon i.e. la courbe de rotation.

Il est d'abord supposé que le gaz est en rotation circulaire dans un disque dont l'inclinaison peut varier avec la distance au centre. Il existe ensuite principalement deux méthodes pour déterminer la courbe de rotation. La première, développée pour les observations radios du gaz neutre (ROTCUR, Begeman, 1987), tente de minimiser la dispersion des vitesses du gaz à l'intérieur d'anneaux de centre et d'inclinaison arbitraire par rapport au plan de la galaxie. Le processus est itératif et cherche le χ^2 minimum en faisant varier les

paramètres de la courbe (centre, angles de position et d'inclinaison et vitesse circulaire). Une première minimisation est effectuée où tous les paramètres sont laissés libres, le nombre et la largeur des anneaux étant ajustés pour maximiser la résolution et minimiser l'incertitude en chaque anneau. Le centre de rotation trouvé ainsi est ensuite fixé et la procédure est appliquée de nouveau pour déterminer plus finement (avec des anneaux plus étroits) les angles de position et d'inclinaison et surtout, les vitesses de rotation circulaire.

Si l'inclinaison des anneaux est constante, c'est-à-dire si le disque galactique est peu gauchi, une seconde méthode[a] permettant une meilleure précision, est utilisée. Le principal outil de diagnostique est ici la comparaison directe entre les côtés approchant et fuyant du disque. Le centre dynamique et les angles de position et d'inclinaison sont déterminés pour un meilleur accord entre les deux côtés. Un champ de vitesse artificiel est ensuite construit selon ces paramètres en supposant une pure rotation circulaire. Ce champ est soustrait du champ observé pour mettre en évidence toute erreur dans la détermination des paramètres et surtout, tout écart à la circularité des orbites du gaz (e.g. barres galactiques).

La courbe de rotation ainsi obtenue est une représentation robuste, car moyennée azimutalement, de la cinématique d'un disque galactique et un outil indispensable pour l'étude des forces et des masses visibles et invisibles en action à l'intérieur des galaxies spirales.

1.2.8 Au télescope

Malgré la puisssance de toutes ces techniques d'analyse et de correction des données, l'optimisation des paramètres d'observations est plus que tout un gage d'information scientifique de qualité. Une bonne préparation est d'autant plus cruciale lorsque de précieuses nuits d'observation sur de grands télescopes ne sont octroyées qu'à raison de 2 ou 3 par année!

En outre, il convient de choisir des filtres interférentiels centrés sur la vitesse systémique de l'objet sous observation, suffisamment larges pour contenir l'ensemble des vitesses radiales mais assez restrictifs pour ne laisser passer qu'un ordre d'interférence dans une région donnée de l'objet.

À moins d'avoir de très bonnes conditions photométriques ou des sources à très haute brillance de surface, le critère premier dans le choix d'un détecteur est son faible bruit de lecture, même au sacrifice d'un peu d'efficacité quantique. Cela permettra de faire

[a] ADHOC: www-obs.cnrs-mrs.fr/interferometrie/interferometrie.html

plusieurs passage par objets et augmentera passablement la qualité des spectres obtenus.

References

Amram, P. 1991, PhD thesis, Université de Provence

Bennett, C. L. 2000, ASP Conf. Ser. 195: Imaging the Universe in Three Dimensions, 58

Le Coarer, E. L. & Segrétain, L. 1989, Rapport de stage, ENS de Lyon

Bland, J. and Tully, R. B. 1989, AJ, 98, 723

Hernandez, G. 1986, Fabry-Perot interferometers (Cambridge Studies in Modern Optics, Cambridge, University Press, 1986)

Plana, H. 1996, PhD thesis, Université de Provence

Reynolds, G. O., Develis, J. B. & Thompson, B. J. 1989, Bellingham: Society of Photo-Optical Instrumentation Engineers (SPIE), 1989, edited by Reynolds, George O.; DeVelis, John B.; Thompson, Brian J.,

Vaughan, J. M. 1989, The Fabry-Perot interferometer. History, theory, practice and applications (The Adam Hilger Series on Optics and Optoelectronics, Bristol: Hilger, 1989)

Chapitre 2

Observations Fabry-Perot de NGC 5585

ACCURATE DETERMINATION OF THE MASS DISTRIBUTION IN SPIRAL GALAXIES. I. Fabry-Perot Observation of NGC 5585

SÉBASTIEN BLAIS–OUELLETTE

Département de physique and Observatoire du mont Mégantic, Université de Montréal, C.P. 6128, Succ. centre ville, H3C 3J7 Montréal, Qué., Canada; and

IGRAP, Observatoire de Marseille, 2 Place Le Verrier, F–13248 Marseille Cedex 04, France;

e–mail: blaisous@llnl.gov

CLAUDE CARIGNAN[a]

Département de physique and Observatoire du mont Mégantic, Université de Montréal, C.P. 6128, Succ. centre ville, H3C 3J7 Montréal, Qué., Canada; e–mail: carignan@astro.umontreal.ca

PHILIPPE AMRAM

IGRAP, Observatoire de Marseille, 2 Place Le Verrier, F–13248 Marseille Cedex 04, France;

e–mail: amram@observatoire.cnrs-mrs.fr

STÉPHANIE CÔTÉ[a]

Institut Herzberg d'Astrophysique, Conseil National de Recherche du Canada, 5071 West Saanich Road, V8X 4M6, Victoria, BC, Canada; stephanie.cote@hia.nrc.ca

Published in The Astronomical Journal, 118:2123-2131, 1999 November

Using the example of the Sd galaxy NGC 5585, it is shown that high resolution 2–D HII kinematical data are necessary to determine accurately the parameters of the mass (luminous & dark) distribution in spirals. New CFHT Fabry–Perot Hα observations are combined with low resolution (20 ″) Westerbork HI data to study its mass distribution. Using the combined rotation curve and best fit models, it can be seen that $(\mathcal{M}/L_B)_\star$ of the luminous disk goes from 0.3 using only the HI rotation curve, to 0.8 using both the optical and the radio data. This reduces the dark–to–luminous mass ratio in NGC 5585 by $\sim 30\%$ through increasing the dark matter halo core radius by nearly the same amount. This shows the importance of the inner, rising part of the rotation curve for the accurate determination of the parameters of the global mass (luminous & dark) distribution and suggests that such a fine tuning of the rotation velocities using high resolution 2–D HII kinematics is necessary to look at correlations between the parameters of the dark matter component and other properties of galaxies.

[a]Visiting Astronomers, Canada–France–Hawaii Telescope, operated by the National Research Council of Canada, the Centre National de la Recherche Scientifique de France, and the University of Hawaii.

2.1 Introduction

In the last 25 years, a large number of rotation curves were derived for spiral (Sp) and dwarf irregular (dIrr) galaxies from 2–D HI kinematics obtained with synthesis instruments such as the Westerbork (WSRT) array, the Very Large Array (VLA), and the Australia Telescope (AT) (for a good review of the first 20 years, (see e.g. Ashman, 1992). In many galaxies, especially late–type spirals and dwarf irregulars, the HI extends much further out than the optical and thus than the HII emission. An argument often used is that, since the HI rotation curve probes the gravitational potential in the dark matter dominated region, it is best suited to derive the parameters of the mass distribution and especially of the dark matter halo. However, as will be shown, the parameters of the mass models (and especially of the dark matter distribution) are very sensitive not only to the flat part of the rotation curve (best probed by the HI observations) but also to the rising inner part, which can be derived with greater precision using 2–D Hα observations (see e.g. Amram et al., 1992, 1994, 1995, 1996). This is also well illustrated by (Swaters, 1999) who clearly shows the impact of varying the position of the first few velocity points (within the uncertainties due to beam smearing) on the parameters of the mass models even in the dark matter dominated dwarfs.

What is now regarded as the classical method to study the mass distribution (Van Albada et al., 1985; Carignan & Freeman, 1985) is illustrated in Fig.7a, which shows the analysis of the mass distribution of NGC 5585 using its HI rotation curve (Côté et al., 1991). See also (Begeman, 1987; Broeils, 1992) for many more examples. First, the rotation curve is obtained by fitting a "tilted–ring" model to the HI velocity field in order to represent the warp of the HI disk, which is almost always present. The accuracy of the model representation is then checked by looking at the residual (data − model) map (Warner et al., 1973; Sancisi & Allen, 1979). Then the luminosity profile in the reddest band available to probe the mass dominant population is transformed into a mass distribution for the stellar disk, assuming a constant value of $(\mathcal{M}/\mathrm{L}_B)_\star$ (Casertano, 1983; Carignan & Freeman, 1985). For the contribution of the gaseous component, the HI radial profile scaled by 1.33 is used to account for He. The difference between the observed rotation curve and the computed contribution to the curve of the luminous (stars & gas) component is thus the contribution of the dark component, which can be represented by an isothermal halo (Carignan & Freeman, 1985) or some other functional form (e.g. Lake & Feinswog, 1989). The model of Fig.7a allows us to study the dark–to–luminous mass ratio as a function of radius, as shown in Fig.7b. Naturally, this is for standard gravity. Some alternative models, such as MOND, have also been explored (Milgrom, 1983b; Sanders, 1996; McGaugh & De Blok, 1998).

The example of NGC 5585 shows the importance of an accurate determination of the rising part of the rotation curve, since this is the part that mainly constrains the values of two of the three free parameters of the mass model; namely, the mass–to–light ratio of the luminous stellar disk $(\mathcal{M}/L_B)_\star$ and the core radius r_c. The third parameter, the one dimensional velocity dispersion σ of the dark isothermal halo is mainly constrained by the outer part of the rotation curve. The HI observations, often optimized for maximum sensitivity in the outer parts, have in most of the published studies a resolution of only 20–45 $''$ (higher resolution is naturally possible by adding longer baselines when there is sufficient HI flux). Attempts have been made to correct for the effect of "beam smearing", which can be very important in the inner parts because of the strong velocity gradient (sometimes combined with a strong radial distribution gradient) across the large HI beam. This is examined using as an example the Sc galaxy NGC 3198.

Another point that needs to be stressed is that full 2–D HII kinematical data are necessary for this work and that 1–D long–slit spectroscopy is not sufficient. This is due to the fact that the photometric parameters (we are mainly concerned with the position angle PA and photometric center in this case) used to position the slits on the galaxies can sometime be quite different from the kinematical parameters. Naturally, if the slit is positioned with a slightly wrong PA, the velocities will necessarily be underestimated. This is well illustrated for the case of the rotation curves of galaxies in clusters in Whitmore et al. (1988) for the 1–D long–slit, and in Amram et al. (1996) for 2–D Fabry–Perot.

The importance of the rising part of the rotation curve on the parameters for both the luminous and dark matter distributions is illustrated by two examples in section 2. Section 3 describes the new CFHT Fabry–Perot (FP) observations and data reduction of the NGC 5585 data. The HII kinematics and the optical rotation curve are discussed in Section 4, while the mass models and the parameters of the mass distribution are given in Section 5. Finally, Section 6 gives a summary of the results and draws general conclusions from this study.

2.2 Importance of the Rising Part of the Rotation Curve on the Parameters of the Mass (Luminous & Dark) Distribution

It has always been thought that the problem of "beam smearing" was important mainly in early–type spirals, where the strong gradient due to the presence of the bulge was attenuated in low resolution HI data and where it was obvious that higher resolution data were necessary to see the true kinematics resulting from the centrally concentrated luminous mass distribution. In what follows, it will be shown that, while the effect of beam smearing in late–type spirals may be less dramatic, it can nevertheless have a significant impact on the derived parameters of both the luminous and the dark mass distributions.

2.2.1 The Case of NGC 5585

To show the importance of the first few points of the rotation curve in a galaxy such as NGC 5585, a model was constructed giving no weight to the first two points of the HI curve (Fig.8*Top*). This model mimics a difference of less than 10 $''$ with the real position of the first two points, a very plausible effect of the large radio beams. In this model, the $(\mathcal{M}/L_B)_\star$ of the stellar disk goes from 0.3 (Fig.7) to 1.0 (Fig.8a), with the result that the mass of the stellar disk goes from ~20% of the gaseous disk to a comparable mass. More importantly is that the dark matter halo is less centrally concentrated with a dark–to–luminous mass ratio going from 9.5 (Fig.7b) to 6.3 (Fig.8b) at the last measured point of the rotation curve. This is a difference of more than 30% in the dark–to–luminous mass ratio for a difference of less than 10 $''$ in the position of the first two points of the curve. As illustrated in Fig.7b & Fig.8b, the global distribution of the dark component is also totally different. This is why we think that the ideal rotation curve to study the mass distribution in galaxies should combine the high resolution of Hα FP observations in the inner parts to the high sensitivity of the low resolution HI observations in the outer parts.

2.2.2 The Case of NGC 3198

Begeman (1989) published a Westerbork HI rotation curve of NGC 3198, where he attempted to correct for the effect of beam smearing. Theoretically, one should be able to calculate this effect by convolving the rapidly dropping HI density profile and the rising rotation curve inside the width of the beam. In the inner parts, his rotation velocities are

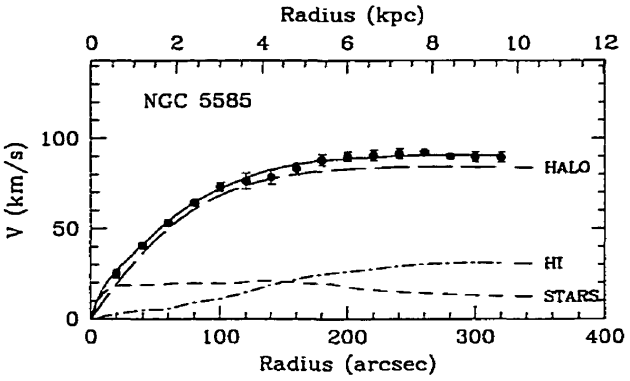

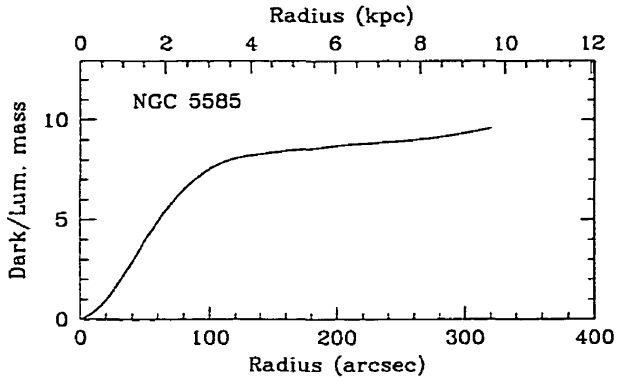

Figure 7: *Top:* Best fit mass model for NGC 5585 using the HI rotation curve. The model parameters are: $(\mathcal{M}/L_B)_\star = 0.3$, r_c 2.8 kpc and $\sigma = 53$ km s^{-1}. *Bottom:* Dark–to–luminous mass ratio as a function of radius.

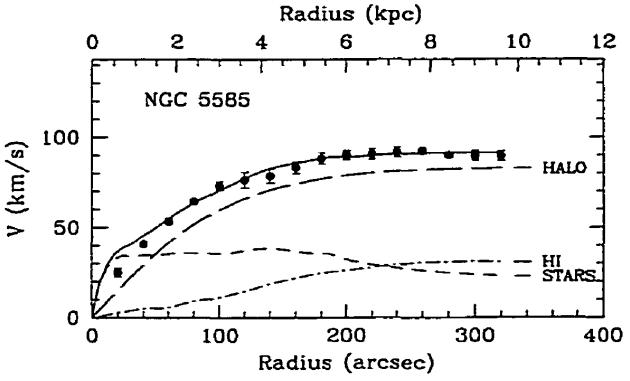

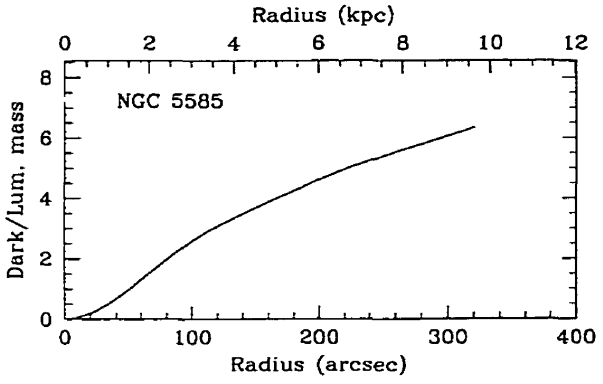

Figure 8: *Top:* Maximum disk mass model for NGC 5585, where the first two points of the HI rotation curve have been given zero weight. The model parameters are: $(\mathcal{M}/L_B)_\star = 1.0$, $r_c = 3.5$ kpc and $\sigma = 52$ km s^{-1}. *Bottom:* Dark–to–luminous mass ratio as a function of radius.

systematically larger (up to 26 km s^{-1} at 30 ″) than the values derived in a previous HI study by (Bosma, 1981). If the corrections are accurate, one would expect that there should be very little gain in using high resolution Hα data. Fig.9 and Table I show the best–fit model using the beam smearing corrected HI data. It can be seen that for r < 3 kpc and r > 15 kpc, the model gives a good representation of the data. However, around 4 kpc, the model velocity is larger by ~ 10 km s^{-1} compared to the measured velocity.

A best-fit model (Fig.10) was obtained by combining Begeman's HI data with the FP Hα kinematical data of Corradi et al. (1991). We see that while the agreement between the two sets of data appears good over all, the optical velocities are somewhat smaller in the steep rising part of the rotation curve. As can be seen in Table I, the dark–to–luminous mass

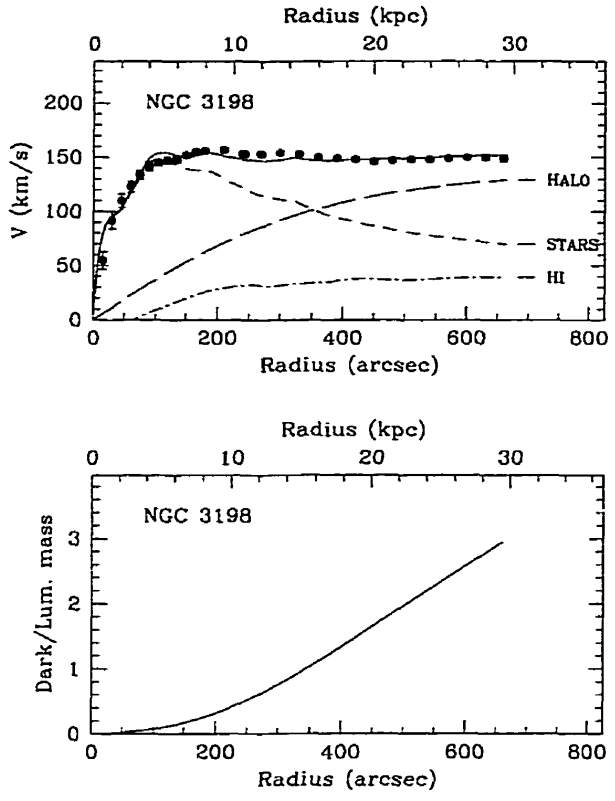

Figure 9: Best fit mass model for NGC 3198 using the HI rotation curve (Begeman, 1989), corrected for beam smearing. The model parameters are: $(\mathcal{M}/L_B)_\star = 9.4$, $r_c = 17.2$ kpc and $\sigma = 85.6$ km s^{-1}.

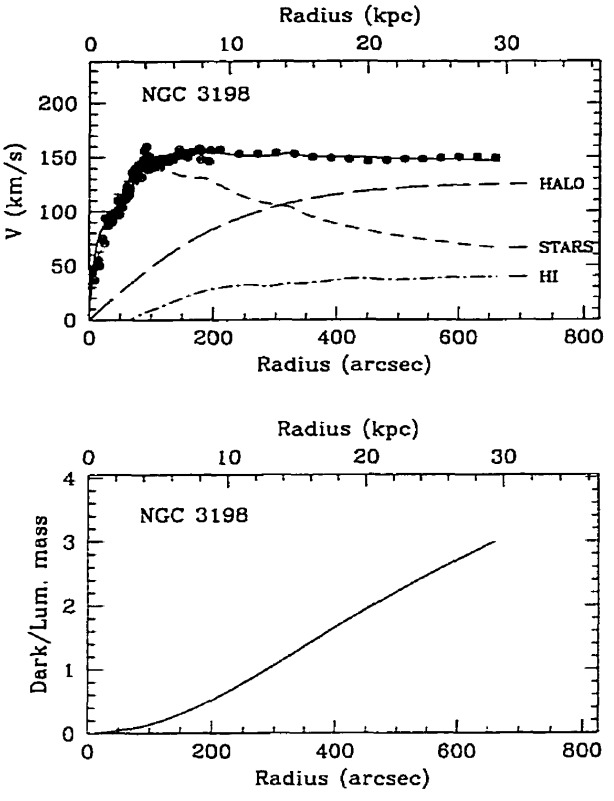

Figure 10: Best fit mass model for NGC 3198 using the HI (filled circles) rotation curve (Begeman, 1989) and the Hα (open circles) rotation curve (Corradi et al., 1991). The model parameters are: $(\mathcal{M}/L_B)_\star = 8.5$, $r_c = 11.7$ kpc and $\sigma = 79.0$ km s^{-1}.

ratio at the last measured point has changed very little between the two models (2.9 $\rightarrow$ 3.0), but the shape of the halo has changed substantially, becoming more centrally concentrated with r_c going from 17.2 to 11.7 kpc, again a change of more than 30%. The apparently small difference in velocity ($\sim$ 5 km s^{-1}) results in an increase of the dark halo central density ρ_0 by nearly a factor of 2 (0.004 $\rightarrow$ 0.008). This suggests that Begeman (1989) may have overestimated his beam smearing corrections.

It is instructive also to compare this result with the earlier Bosma data, which were not corrected for beam smearing, as is the case for most HI data. NGC 3198 is an Sc galaxy, in which the velocity gradient is much smaller than in Sa or Sb galaxies and one would have thought that the effect of beam smearing should not be that dramatic. Fig.11 shows the best

Table I: Parameters of the mass models of NGC 3198.

		ROTATION CURVE		
Parameter		HI [a]	Combined HI [a] and Hα	HI [b]
Luminous disk component:				
$(\mathcal{M}/L_B)_\star$	$(\mathcal{M}_\odot/L_\odot)$	9.4 ±0.2	8.5 ±0.3	2.8 ±0.5
$\mathcal{M}_\star$	$(\mathcal{M}_\odot)$	3.2×10^{10}	2.9×10^{10}	9.6×10^9
$\mathcal{M}_{HI+He}$	$(\mathcal{M}_\odot)$	6.5×10^9	6.5×10^9	6.5×10^9
Dark halo component:				
r_c	(kpc)	17.2 ±1.0	11.7 ±1.0	3.9 ±0.1
σ	$(\mathrm{km\,s^{-1}})$	85.6 ±2.0	79.0 ±1.5	83.4 ±1.0
ρ_0	$(\mathcal{M}_\odot\,\mathrm{pc^{-3}})$	0.004	0.008	0.076
At R_{HO} $r \simeq 13$ kpc:				
ρ_{halo}	$(\mathcal{M}_\odot\,\mathrm{pc^{-3}})$	0.002	0.002	0.002
$\mathcal{M}_{dark+lum}$	$(\mathcal{M}_\odot)$	6.2×10^{10}	6.6×10^{10}	6.6×10^{10}
$(\mathcal{M}/L_B)_{dyn}$		18	19	19.5
$\mathcal{M}_{dark}/\mathcal{M}_{lum}$		0.76	1.1	4.3
At the last measured point $r \simeq 29$ kpc:				
ρ_{halo}	$(\mathcal{M}_\odot\,\mathrm{pc^{-3}})$	0.0005	0.0004	
$\mathcal{M}_{dark+lum}$	$(\mathcal{M}_\odot)$	1.5×10^{11}	1.4×10^{11}	
$(\mathcal{M}/L_B)_{dyn}$		44	41	
$\mathcal{M}_{dark}/\mathcal{M}_{lum}$		2.9	3.0	

[a] Begeman (1989)
[b] Bosma (1981)

fit model using that data set. We see that the mass distribution is completely different, with a much smaller disk and a dark halo that dominates completely for $r \geq 1$ kpc. The result is that, with differences ≤ 10 $\mathrm{km\,s^{-1}}$ for $0 \leq r \leq 6$ kpc, the dark component has nearly 10 times higher central density, which results in an increase of the dark–to–luminous mass ratio from ~ 1 to ~ 4.

Many more examples could be discussed, but we think that the examples above show clearly that high resolution Hα data are necessary to compute accurately the parameters of both the luminous and dark mass distributions.

2.3 Fabry–Perot Observations and Reduction

Table II gives the optical parameters of NGC 5585 and Table III lists the complete observing parameters. The FP observations of the Hα emission line were obtained in February 1994 at the Canada–France–Hawaii Telescope (CFHT). The FP etalon (CFHT1) was

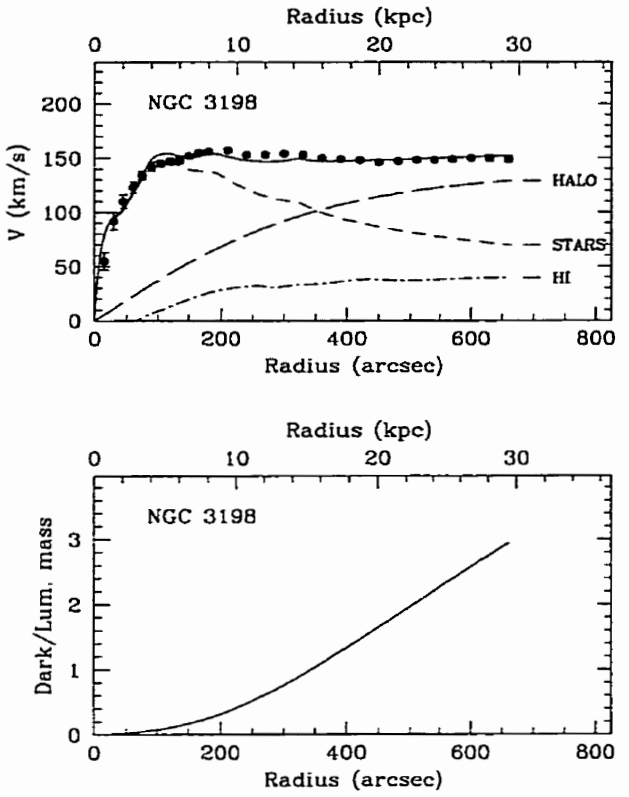

Figure 11: Best fit mass model for NGC 3198 using the HI rotation curve of Bosma (1981), not corrected for beam smearing. The model parameters are: $(\mathcal{M}/\mathrm{L}_B)_\star = 2.8$, $r_c = 3.9$ kpc and $\sigma = 83.4\ \mathrm{km\,s^{-1}}$.

installed in the CFHT's Multi–Object Spectrograph (MOS). A narrow–band filter ($\Delta\lambda =$ 10 Å), centered at $\lambda_0 = 6570$ Å (nearly at the systemic velocity of NGC 5585, $\mathrm{V}_{sys} \approx 305$ $\mathrm{km\,s^{-1}}$), was placed in front of the etalon. The available field with no vignetting was $\approx$ $8.5' \times 8.5'$, with $0.34''$ pix $^{-1}$. The free spectral range of 5.66 Å ($258\ \mathrm{km\,s^{-1}}$) was scanned in 27 (+1 overlapping) channels, giving a sampling of 0.2 Å ($9.2\ \mathrm{km\,s^{-1}}$) per channel. Eight minute integration was spent at each channel position.

2.3.1 Data analysis

Following normal de–biasing and flat–fielding with standard IRAF procedures, a robust 3-D cosmic–ray removal routine, that tracks cosmic rays by spatial (pixel–to–pixel) and spectral (frame–to–frame) analysis, was applied.

Table II: Optical parameters of NGC 5585.

Parameter	Value
Morphological Type[a]	SABd
RA (J2000.0)	$14^h\ 19^m\ 48^s.1$
Dec (J2000.0)	56°43′44″
l	214°.95
b	56°.73
Adopted distance (Mpc)[b]	6.2
	($1' \simeq 1.8$ kpc)
Mean axis ratio, $q = b/a$[c]	0.61 ±0.01
Inclination($q_0 = 0.12$), i[c]	53 °±1 °
Isophotal major diameter, D_{25}[c]	5.27 ′
Major axis PA[c]	99 °±1°
Exponential scale length (kpc)[c]	1.4
Holmberg radius, R_{HO}[c]	3.62 ′
Absolute magnitude, M_B[c]	−17.5
Total luminosity, L_B	$1.5 \times 10^9\ L_\odot$
Helio. radial velocity ($km\,s^{-1}$)[a]	305 ±3

[a]de Vaucouleurs et al. (1991).
[b]$H_0 = 75\ km\,s^{-1}\,Mpc^{-1}$.
[c]Côté, Carignan, & Sancisi (1991).

Since FP systems have multiple optical surfaces, some defocalised ghost reflections can be present (Bland-Hawthorn, 1995), especially since the etalon was not tilted. To get rid of these reflections we composed a "ghost image" by using the ghost reflection of a bright star in the field (Figure 12) and numerically simulating a similar but scaled reflection for every pixel in the field. This image was then subtracted from the original. This procedure removes very efficiently all the reflected continuum and adequately but not perfectly (~80%) the monochromatic emission.

The presence of strong night sky lines combined with photometric variations (transparency, seeing) from one exposure to another led us to proceed to a first background subtraction on each of the 27 non-redundant frames (now assembled in a 3-D cube). This background includes continuous, diffuse light and monochromatic emission from atmospheric OH radicals and from geocoronal Hα. All these backgrounds vary both spatially and temporally. Using the radial symmetry of the FP, the sky was evaluated by azimuthally summing rings of constant phase where the galaxy signal had been masked. The computed background was then removed in each ring.

A neon calibration lamp (λ6598.95 Å) was used to fix the zero point at each pixel. To be totally device independent, the theoretical position of a sky emission line was then

Table III: Parameters of the Fabry–Perot observations.

Parameter	Value
Date of observations	February 20, 1994
Telescope	3.6 m CFHT
Instrumentation:	
Focal plane instrument	MOSFP
CCD detector	2048×2048 Loral3, $\sigma = 8\,e^{-1}$
Filter	$\lambda_0 = 6570$ Å, $\Delta\lambda = 10$ Å
Fabry–Perot etalon	Scanning QW1162 (CFHT1)
Interference order	1155 @ λ_{NEON}
Mean Finesse in the field	12
Calibration lamp	Neon ($\lambda = 6598.95$ Å)
Duration	
Per channel	8 min/channel
Total	3 h 45 min
Spatial Parameters:	
Field size	$8.5' \times 8.5'$
Pixel scale	$0.34''$ pix^{-1}
Spectral Parameters:	
Number of channels	27
Free spectral range	5.66 Å (258 km s^{-1})
Sampling	0.2 Å (9.2 km s^{-1})/channel

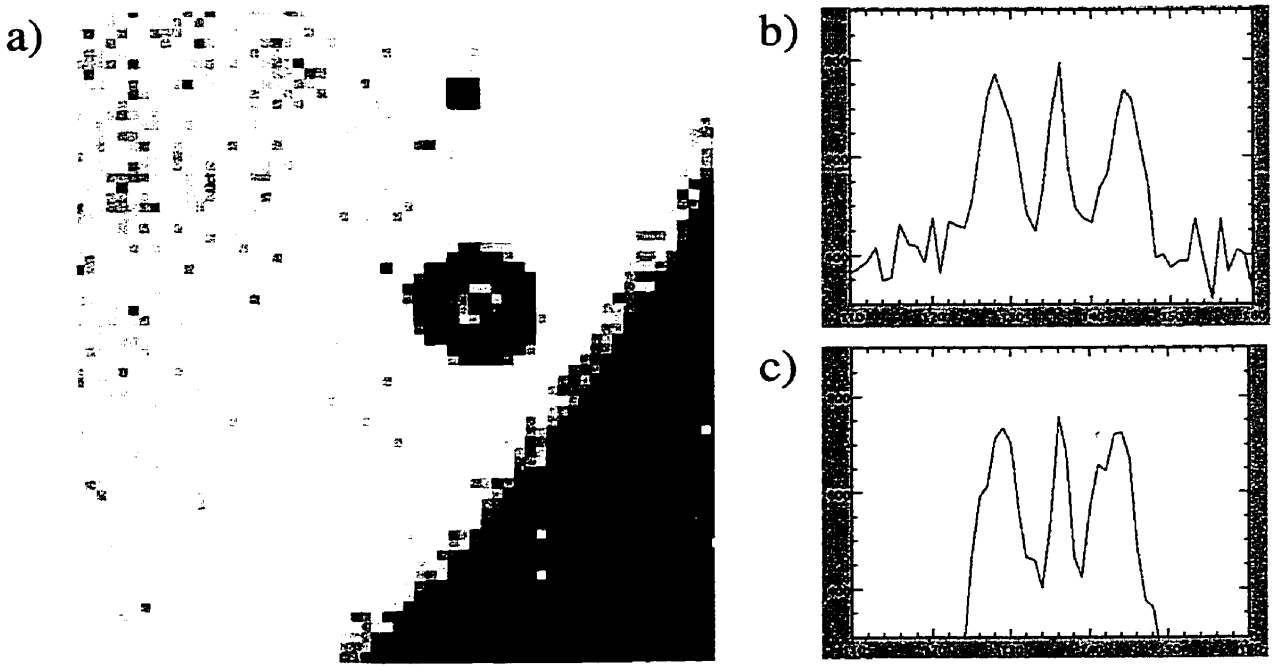

Figure 12: *Left*, Real reflection of a star; *top right*, cut along the y axis of the real reflection; *bottom right*, cut along the y axis of the simulated reflection.

used to fine-tuned the phase (wavelength origin) at each pixel in order to get a particular wavelength on an exact x-y plane. Due to limited free spectral range, this telluric line is a composite of geocoronal Hα (λ6562.74 or 517 $\mathrm{km\,s^{-1}}$) and an OH line (λ6568.78 or 532 $\mathrm{km\,s^{-1}}$). Since there is no way to determine the relative contribution of each line, we are left with some uncertainties on the systemic velocity of the galaxy, but this does not affect the relative velocities and the rotation curve.

In order to get sufficient signal–to–noise throughout the image, two different Gaussian smoothings (σ=2.5 and 3.5 pixels) were performed on the cube using the ADHOC package[a]. Velocity maps were then obtained using the intensity weighted means of the Hα peaks to determine the radial velocity for each pixel. A final variable resolution velocity map was constructed (Figure 13) using higher resolution for regions with originally higher signal-to-noise.

2.4 HII Kinematics and Optical Rotation Curve

The rotation curve has been obtained from the velocity field following two different methods. The first estimate was made using the task ROCUR (Begeman, 1987; Côté et al., 1991) in the AIPS package, where annuli in the plane of the galaxy (ellipses in the plane of sky) are fitted to the velocity field, minimizing the dispersion inside each ring. In this way, the center, systemic velocity, position angle and inclination are evaluated. Secondly, the ADHOC package was used to fine–tune these parameters by direct visualization and comparison with a residual velocity field. The optical rotation curve at 5″ resolution is given in Table XVI and Figure 14. Note that there are two common ways to represent the uncertainties on a rotation curve: the error on the mean ($\sigma/\sqrt{N}$)) and the velocity difference of the receding and approaching sides weighted by the number of points on each side, a method often used for HI rotation curves. To be conservative, we took the maximum of the two values.

At intermediate radii, the receding side of the galaxy is still affected by residual sky emission. This is caused by the lack of regions with pure sky signal in the most central interference rings, making the measurement of the sky emission lines less accurate and only partially subtracted. The final effect here is to lower the rotation velocities between 2 and 4 kpc in radius. As we will see, this is in the region where it is possible to rely with confidence on the HI data, because of the shallower fall of HI density and the slower rise of the rotation curve that make beam smearing negligible.

[a] www-obs.cnrs-mrs.fr/adhoc/adhoc.html

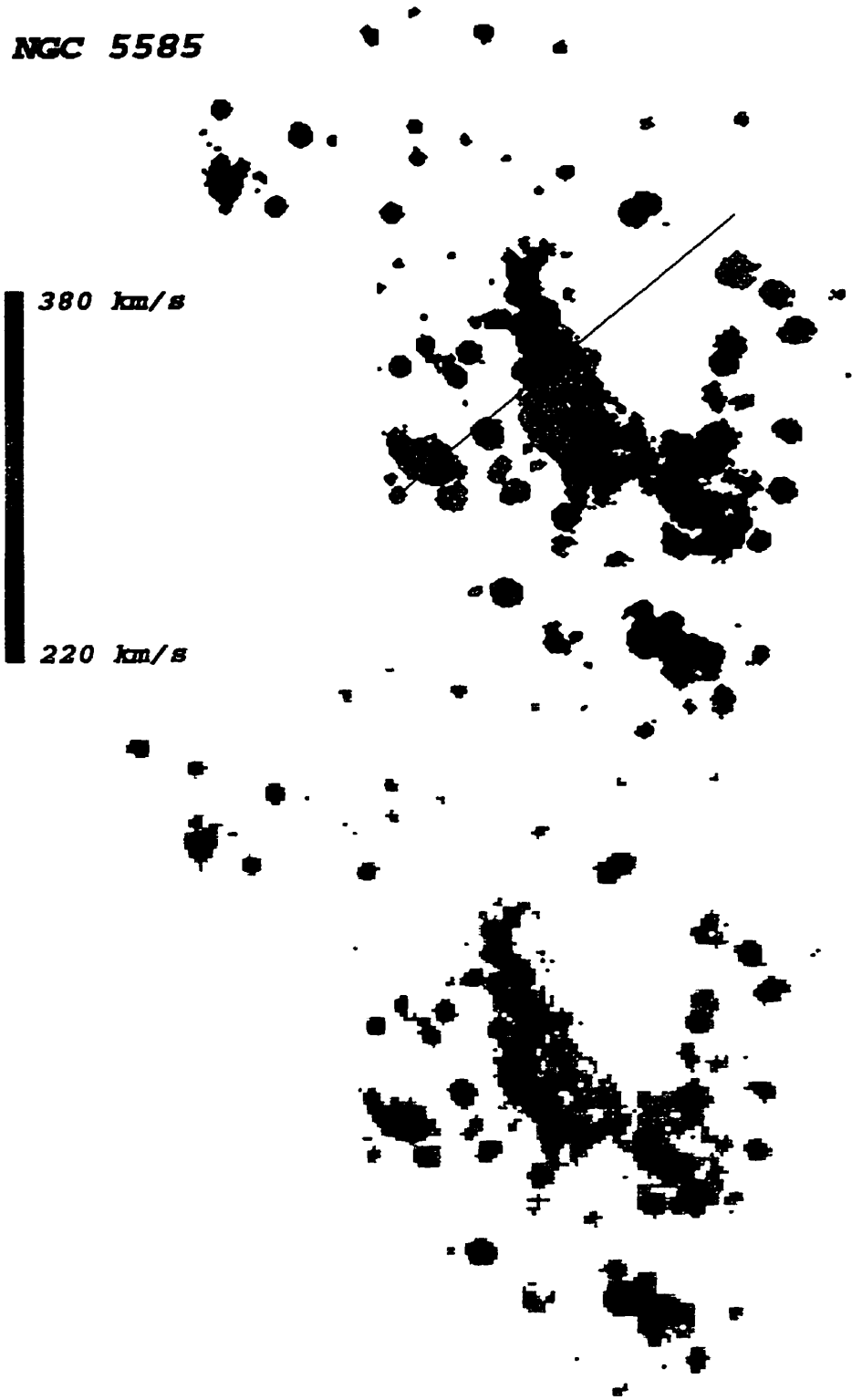

Figure 13: Velocity field and Hα image of NGC 5585. The X and the grey line indicate the kinematic center and the axis of separation between the approaching and receding sides.

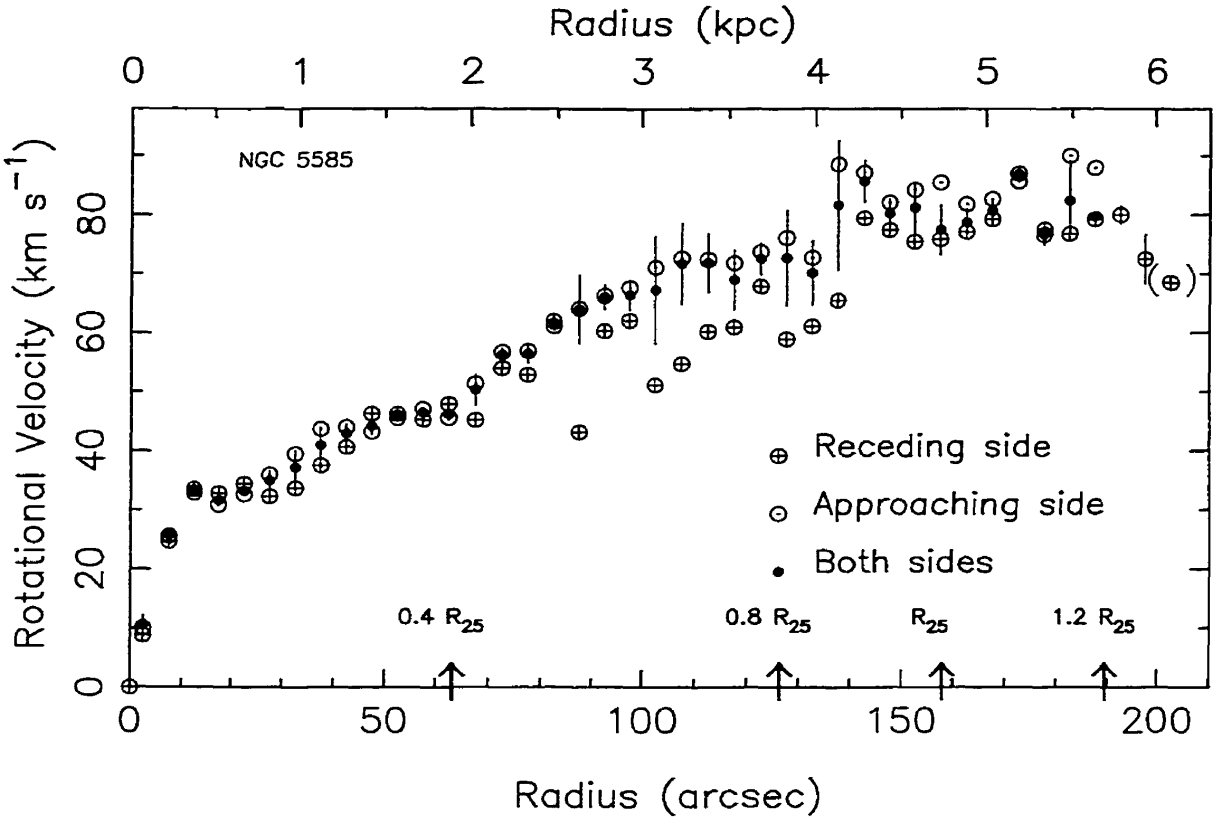

Figure 14: Optical rotation curve of NGC 5585.

2.5 Mass Models and Parameters of the Mass Distribution

The models used are described in Carignan & Freeman (1985). However, instead of being "maximum disk" models, they are "best–fit" models. A χ^2 minimization technique is used in the three–parameter space of the model. Namely, those parameters are: $(\mathcal{M}/L_B)_\star$ of the stellar disk, the core radius r_c and the one–dimensional velocity dispersion σ of the dark isothermal halo. Alternatively, one can use the central density $\rho_0 = 9\sigma^2/4\pi G r_c^2$. The surface photometry and the HI kinematics are from Côté et al. (1991).

2.5.1 Mass Model from the Hα Rotation Curve

The best–fit mass model for the Hα rotation curve at 5″ resolution is shown in Fig.15. It can be seen that there is a clear sign of the disk mass in the rotation curve, which is well fitted. In fact, the best–fit model is essentially a maximum disk model. The mass–to–light ratio of the stellar disk goes from 0.3 using the HI data to 1.0 using the Hα data, which

causes the halo to become less centrally concentrated. For the dark halo, the parameters are $r_c = 4.1$ kpc, $\rho_0 = 0.023\ \mathcal{M}_\odot\,pc^{-3}$ and $\sigma = 49.1\ km\,s^{-1}$, which represent a decrease of ρ_0 of more than 50%. Interestingly, the Hα rotation curve provides a much better fit to the MOND model ($a_0 = 1.2\times10^{-8} cms^{-2}$, $M^*/L_B = 0.5$) than the HI curve alone (see figure 1 of Sanders, 1996). However, the little kink seen at radius $\simeq$1 kpc could indicate the transition between the disk dominated region and the halo dominated region, which would exclude alternative gravitational theories based on luminous matter only. This feature could also be the dynamical signature of an inner bar, but the 2-D velocity field does not show evidence of non-circular motions.

It is interesting to look at the shape of the different components as a function of radius for this Hα rotation curve, derived out to $\sim$1.3 R_{25} (herein defined as RC3 $D_{25}/2$) or $\simeq 3.3' \simeq 6.0$ kpc. In massive spirals, the stellar disk usually dominates the mass distribution for $r < R_{25}$. Typical $\mathcal{M}_{dark}/\mathcal{M}_{lum}$ are between 0.5 to 1.0 at that radius. This is certainly not the case here with $\mathcal{M}_{dark}/\mathcal{M}_{lum} \simeq 4.0$ at the last measured point of the rotation curve. Moreover, at the last point, there is almost as much luminous mass in gas as in stars. So, for a dwarf spiral such as NGC 5585, the mass distribution is much more reminiscent of what is seen in dIrr (e.g. DDO 154: Carignan & Freeman 1988, Carignan & Beaulieu 1989; DDO 170: Lake, Shommer, & van Gorkom 1990) than in massive Sp galaxies (e.g. NGC 6946: Carignan et al. 1990; NGC 3198: van Albada et al. 1985). Other late–type Sp such as IC 2574 (Martimbeau et al., 1994) and NGC 3109 (Jobin & Carignan, 1990), both of type Sm, also have a strong contribution from dark matter even in the inner parts but show solid-body HI rotation curves.

2.5.2 Mass Model from the Combined HI and Hα Rotation Curve

Table IV gives the parameters of the mass models constructed using only the HI rotation curve, only the Hα curve, and the combined HI & Hα curve. For our adopted mass model of NGC 5585, we combine the high resolution of the Hα data in the inner parts with the high sensitivity of the HI data in the outer parts. Since we are making a best–fit model, one has to understand that, because of the higher resolution, there are more HII data points than HI data points. This means that the optical data would tend to have a higher weight than the radio data. Since optical velocities are derived from high S/N data out to a radius of 120″ and since Fig. 9 of (Côté et al., 1991) shows that this is the region where the HI parameters are not well defined, we decided to use for the final model the Hα data for $r < 120''$ and the HI data for $r > 120''$.

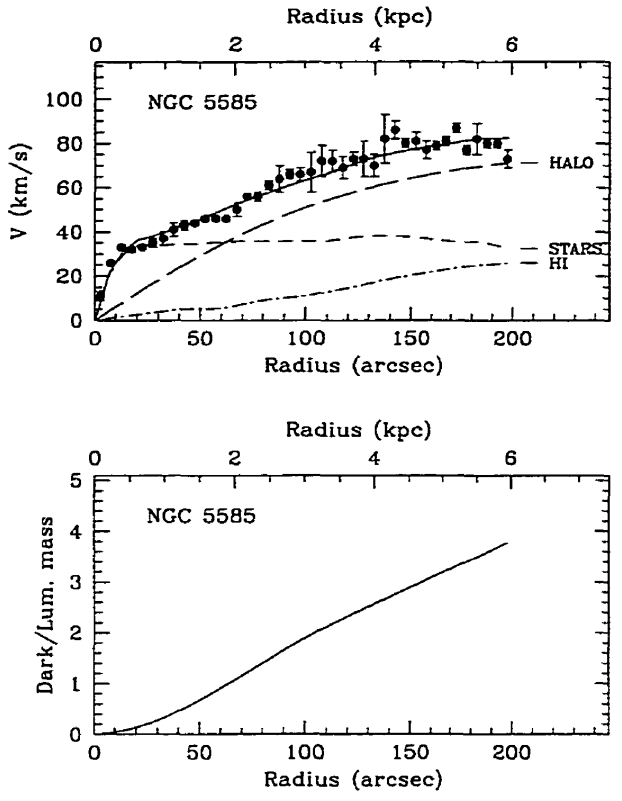

Figure 15: Best fit mass model for NGC 5585 using the Hα rotation curve at 5 "resolution. The model parameters are: $(\mathcal{M}/\mathrm{L}_B)_\star = 0.8$, r_c =3.7 kpc and $\sigma = 48$ km s^{-1}.

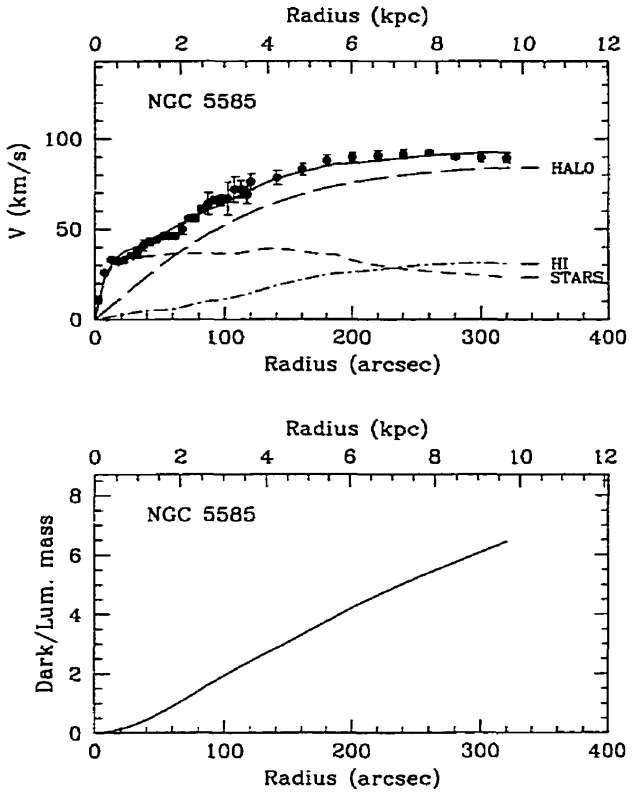

Figure 16: Adopted best fit mass model for NGC 5585 using the Hα rotation curve for r $< 120''$ and the HI rotation curve for r $> 120''$. The model parameters are: $(\mathcal{M}/\mathrm{L}_B)_\star = 1.0$, $r_c = 4.3$ kpc and $\sigma = 53.6$ km s^{-1}.

This adopted model is shown in Fig.16. The parameters of the model are: $(\mathcal{M}/\mathrm{L}_B)_\star$ = 1.0, $\mathrm{r_c} = 4.3$ kpc, $\rho_0 = 0.024\ \mathcal{M}_\odot\,\mathrm{pc}^{-3}$ and $\sigma = 53.6$ km s^{-1}. As expected, σ is very similar in the combined HI & Hα curve as in the HI rotation curve. This is the case because this parameter is a measure of the maximum amplitude of the rotation curve, which is mainly defined by the HI data in the outer parts. However, the two other parameters $(\mathcal{M}/\mathrm{L}_B)_\star$ for the stellar disk and ρ_0 of the dark halo (which are coupled) have nearly the same values as those derived with the Hα curve. Again, this is because $(\mathcal{M}/\mathrm{L}_B)_\star$ of the luminous stellar disk, and hence the scaling parameter of the dark halo r_c, is mainly constrained by the HII data in the inner parts. Interestingly, because this newly derived central density is significantly lower, this means that this late-type galaxy's dark halo is even less concentrated; therefore this exacerbates the discrepancy between observed rotation curves and those predicted by

Table IV: Parameters of the mass models of NGC 5585.

		ROTATION CURVE		
Parameter		HI	Hα	Combined HI and Hα
Luminous disk component:				
$(\mathcal{M}/L_B)_\star$	$(\mathcal{M}_\odot/L_\odot)$	0.3 ±0.3 [a]	1.0 ±0.1	1.0 ±0.1
$\mathcal{M}_\star$	$(\mathcal{M}_\odot)$	3.3×10^8	1.1×10^9	9.9×10^8
$\mathcal{M}_{HI+He}$	$(\mathcal{M}_\odot)$	1.4×10^9	1.4×10^9	1.4×10^9
Dark halo component:				
r_c	(kpc)	2.8 ±0.3	4.1 ±0.4	4.3 ±0.4
σ	$(\mathrm{km\,s^{-1}})$	52.9 ±2.0	49.1 ±2.0	53.6 ±1.6
ρ_0	$(\mathcal{M}_\odot\,\mathrm{pc^{-3}})$	0.060	0.023	0.024
At R_{HO} $r = 6.5$ kpc:				
ρ_{halo}	$(\mathcal{M}_\odot\,\mathrm{pc^{-3}})$	0.0035		0.0041
$\mathcal{M}_{dark+lum}$	$(\mathcal{M}_\odot)$	1.2×10^{10}		1.1×10^{10}
$(\mathcal{M}/L_B)_{dyn}$		10.6		10.1
$\mathcal{M}_{dark}/\mathcal{M}_{lum}$		8.7		4.6
At the last measured point $r = 9.6$ kpc:				
ρ_{halo}	$(\mathcal{M}_\odot\,\mathrm{pc^{-3}})$	0.0013		0.0017
$\mathcal{M}_{dark+lum}$	$(\mathcal{M}_\odot)$	1.7×10^{10}		1.8×10^{10}
$(\mathcal{M}/L_B)_{dyn}$		15.7		16.4
$\mathcal{M}_{dark}/\mathcal{M}_{lum}$		9.5		6.6

[a] The difference in $(\mathcal{M}/L_B)_\star$ between this paper and Côté et al. (1991) comes from using a different Galactic extinction value, $A_B = 0.0$ (RC3).

standard CDM halo simulations , which are already too concentrated for late-type and dwarf galaxies (see, e.g., Navarro 1996 but also Kravtsov et al. 1998).

2.6 Summary and Conclusions

The importance of an accurate determination of the rising part of a rotation curve using full 2–D high resolution FP observations is well illustrated by the example of NGC 5585. The principal conclusions follow.

1. The parameters of the mass distribution of both the dark and the luminous components are very sensitive to the rising part of the rotation curve (the first few velocity points) not only in early-type spirals, where the velocity gradient is large in the inner parts, but also in late-type spirals, which have a much shallower gradient. The sensitivity is especially important when the contributions of dark and luminous matter are comparable.

2. With the example of NGC 3198, it is shown that it is very difficult to correct

theoretically for the beam smearing effect seen in radio data.

3. Full 3-D spectroscopy, obtained with Fabry-Perot spectroscopy, is to be preferred to long–slit spectroscopy in order to derive properly the orientation parameters (namely, the rotation center and the position angle) and hence not underestimate the rotational velocities.

4. Combining new Hα CFHT FP data with Westerbork HI data reduced the ratio $\mathcal{M}_{dark}/\mathcal{M}_{lum}$ by $\simeq$ 30% via a decrease of the central density by nearly a factor of 3 for the late-type spiral NGC 5585. If such large errors are common, one could imagine that it could mask any physical correlation between the parameters of the dark and the luminous matter.

5. Finally, the optimal rotation curve is clearly a combination of 2–D high resolution spectroscopy for the inner part of spiral galaxies and high sensitivity radio observations for the outer regions.

We would like to thank the staff of the CFHT for their support during the FP data acquisition and Daniel Durand from DAO who helped with data acquisition. We also warmly thank Jacques Boulesteix for fruitfull discussion on Fabry-Perot reduction and Anthony F.J. Moffat for useful comments. CC acknowledges grants from NSERC (Canada) and FCAR (Québec).

References

Amram, P., Balkowski, C., Boulesteix, J., Cayatte, V., Marcelin, M., & Sullivan, III, W. 1996, A&A, 310, 737

Amram, P., Boulesteix, J., Marcelin, M., Balkowski, C., Cayatte, V., & Sullivan, W. 1995, A&AS, 113, 35

Amram, P., Le Coarer, E., Marcelin, M., Balkowski, C., Sullivan, W. T., I., & Cayatte, V. 1992, A&AS, 94, 175

Amram, P., Marcelin, M., Balkowski, C., Cayatte, V., Sullivan, III, W., & Le Coarer, E. 1994, A&AS, 103, 5

Ashman, K. M. 1992, PASP, 104, 1109

Begeman, K. 1987, PhD thesis, Rijksuniversiteit Groningen

Begeman, K. G. 1989, A&A, 223, 47

Bland-Hawthorn, J. 1995, in ASP Conf. Ser. 71: IAU Colloq. 149: Tridimensional Optical Spectroscopic Methods in Astrophysics, 72

Bosma, A. 1981, AJ, 86, 1791

Broeils, A. 1992, PhD thesis, Rijksuniversiteit Groningen

Carignan, C., Charbonneau, P., Boulanger, F., & Viallefond, F. 1990, A&A, 234, 43

Carignan, C. & Freeman, K. C. 1985, ApJ, 294, 494

Casertano, S. 1983, MNRAS, 203, 735

Corradi, R. L. M., Boulesteix, J., Bosma, A., Amram, P., & Capaccioli, M. 1991, A&A, 244, 27

Côté, S., Carignan, C., & Sancisi, R. 1991, AJ, 102, 904

Jobin, M. & Carignan, C. 1990, AJ, 100, 648

Kravtsov, A. V., Klypin, A. A., Bullock, J. S., & Primack, J. R. 1998, ApJ, 502, 48

Lake, G. & Feinswog, L. 1989, AJ, 98, 166

Lake, G., Schommer, R. A., & Van Gorkom, J. H. 1990, AJ, 99, 547

Martimbeau, N., Carignan, C., & Roy, J.-R. 1994, AJ, 107, 543

McGaugh, S. S. & De Blok, W. J. G. 1998, ApJ, 499, 41

Milgrom, M. 1983, ApJ, 270, 365

Navarro, J. F., Eke, V. R., & Frenk, C. S. 1996, MNRAS, 283, L72

Sancisi, R. & Allen, R. J. 1979, A&A, 74, 73

Sanders, R. H. 1996, ApJ, 473, 117

Swaters, R. 1999, in ASP Conf. Ser. 182: Galaxy Dynamics - A Rutgers Symposium, 369

Van Albada, T. S., Bahcall, J. N., Begeman, K., & Sancisi, R. 1985, ApJ, 295, 305

Warner, P. J., Wright, M. C. H., & Baldwin, J. E. 1973, MNRAS, 163, 163

Whitmore, B. C., Forbes, D. A., & Rubin, V. C. 1988, ApJ, 333, 542

Chapitre 3

Déterminer la forme des halos sombres

ACCURATE DETERMINATION OF THE MASS DISTRIBUTION IN SPIRAL GALAXIES. II. Testing the Shape of Dark Halos

SÉBASTIEN BLAIS–OUELLETTE
Département de physique and Observatoire du mont Mégantic, Université de Montréal, C.P. 6128, Succ. centre ville, Montréal, Québec, Canada. H3C 3J7 and
Observatoire de Marseille, 2 Place Le Verrier, F–13248 Marseille Cedex 04, France
e–mail: blaisous@llnl.gov

PHILIPPE AMRAM
Observatoire de Marseille, 2 Place Le Verrier, F–13248 Marseille Cedex 04, France
e–mail: amram@observatoire.cnrs-mrs.fr

CLAUDE CARIGNAN[a]
Département de physique and Observatoire du mont Mégantic, Université de Montréal, C.P. 6128, Succ. centre ville, Montréal, Québec, Canada. H3C 3J7
e–mail: carignan@astro.umontreal.ca

Submitted to Astronomical Journal

New high resolution CFHT Fabry–Perot data, combined with published VLA 21 cm observations are used to determine the mass distribution of NGC 3109 and IC 2574. The multi-wavelength rotation curves allow to test with confidence different dark halo functional forms from the pseudo-isothermal sphere to some popular halo distributions motivated by N-body simulations. It appears that density distributions with an inner logarithmic slope ≤ -1 are very hard to reconcile with rotation curves of late type spirals. Modified Newtonian Dynamics (MOND) is also considered as a potential solution to missing mass and tested the same way. The new higher resolution data show that MOND can reproduce in details the rotation curve of IC 2574 but confirm its difficulty to fit the kinematics of NGC 3109.

[a]Visiting Astronomer, Canada–France–Hawaii Telescope, operated by the National Research Council of Canada, the Centre National de la Recherche Scientifique de France, and the University of Hawaii.

3.1 Introduction

Over the last 30 years, rotation curves have been a very efficient tool to study the mass distribution in spiral galaxies. They clearly brought to light the important discrepancy between the luminous mass and the gravitational mass that has led to the supposition of a large amount of dark matter in the Universe. The now commonly accepted picture is that this unseen matter takes the form of large halos in the center of which galaxies are embedded. Alternatively, the gravitational attraction could deviate from the pure Newtonian force at very low acceleration so that no dark matter is necessary.

The resolution reached by N-body simulations of the cosmic evolution of dark halos (Navarro et al., 1996b, 1997; Fukushige & Makino, 1997; More et al., 1998; Kravtsov et al., 1998) allows one to predict the inner part of halo density profiles. In theory, these profiles could be directly compared to the ones deduced from modeling the rotation curves. Unfortunately, the sensitivity of the rotation curves to the exact density profile of the halos is quite low and one must use the highest sensitivity and the highest resolution possible to arrive at useful comparisons (Blais-Ouellette et al., 1999, hereafter paper I).

This study investigates primarily, in the context of Newtonian gravitation, the density profile of the dark halos of two late type spiral galaxies: NGC 3109 and IC 2574. As late type, their bulge is minimal making them well suited objects for sensitive mass distribution studies because of the reduced uncertainties due to the negligible spheroid contribution in the inner parts. Mass models of NGC 3109 based on radio observations have already been presented by Jobin & Carignan (1990) while the dark matter distribution in IC 2574 have been studied by Martimbeau et al. (1994). New high resolution Fabry-Perot observations of the Hα emission line are used in combination with the published 21 cm data to form accurate multi–wavelength rotation curves. These curves are used to model the mass distribution in the galaxies. The models include a stellar disk, a gaseous component and a dark spherical halo.

Moreover, NGC 3109 has often been presented as a test for the Modified Newtonian Dynamics (Milgrom, 1983b). As noted in Broeils (1992), the inner part of the rotation curve is crucial to draw any conclusion on the MOND fit to this galaxy. Therefore, the mass models of the two galaxies based on the MOND assumption are presented as well.

The CFHT Fabry-Perot observations are described in Section 3.2 while the mass models of the two galaxies, to which we add NGC 5585 and NGC 3198 from paper I, are discussed in Section 3.3

3.2 New Fabry–Perot Observations

Table V: Parameters of the Fabry–Perot observations.

Dates of observations	February 21 and 22, 1994
Telescope	3.6 m CFHT
Instrumentation:	
Focal plane instrument	MOSFP
CCD detector	2048×2048 Loral3, $\sigma = 8\,e^{-1}$
Fabry–Perot etalon	Scanning QW1162 (CFHT1)
Interference order	1155 @ λ_{NEON}
Mean Finesse in the field	12
Calibration lamp	Neon ($\lambda = 6598.95$ Å)
Duration	
NGC 3109	
Per channel	7.28 min/channel
Total	3 h 24 min
Filter	$\lambda_0 = 6565.5$ Å, $\Delta\lambda = 12$ Å
IC 2574	
Per channel	8.05 min/channel
Total	3 h 45 min
Filter	$\lambda_0 = 6559.5$ Å, $\Delta\lambda = 12$ Å
Spatial Parameters:	
Field size	$8.5' \times 8.5'$
Pixel scale	$0.314''\,pix^{-1}$
Spectral Parameters:	
Number of channels	27
Free spectral range	5.66 Å (258 km s^{-1})
Sampling	0.21 Å (9.6 km s^{-1})/channel

The Fabry-Perot observations of the Hα emission line were obtained in February 1994 at the Canada–France–Hawaii Telescope (CFHT). The etalon (CFHT1) was installed in the CFHT's Multi–Object Spectrograph (MOS). A narrow–band filter ($\Delta\lambda \approx 12$ Å), centered at $\lambda_0 = 6565.5$ Å for NGC 3109 ($V_{sys} \approx 402$ km s^{-1}) and at $\lambda_0 = 6559.5$ Å for IC 2574 ($V_{sys} \approx 53$ km s^{-1}), was placed in front of the etalon. The available field with no vignetting was $\approx 8.5' \times 8.5'$, with $0.314''\,px^{-1}$. The free spectral range of 5.66 Å (259.5 km s^{-1}) was scanned in 27 (+1 overlapping) channels, giving a sampling of 0.21 Å (9.6 km s^{-1}) per channel. Eight minutes integration were spent at each channel position. Table V lists the complete observing parameters.

Following normal de–biasing and flat–fielding with standard IRAF procedures, a robust 3-D cosmic–ray removal routine, that tracks cosmic rays by spatial (pixel–to–pixel) and spectral (frame–to–frame) analysis, was applied. Ghost reflections were then removed using the technique described in Paper I.

With the ADHOC software package[a], photometric variations were corrected using the mean night sky (background + emission lines) to calculate the corrections to apply to each frame.

Then, a calibration based on a neon lamp (λ6598.95 Å) was used to fix the zero point of the spectrum at each pixel.

3.2.1 NGC 3109

Table VI: Parameters of NGC 3109.

Parameter	Value
Morphological Type[a]	SBm
RA (J2000.0)	$10^h\ 03^m\ 06\overset{s}{.}6$
Dec (J2000.0)	-26°09′32″
l	262 °.10
b	23 °.07
Adopted distance (Mpc)[b]	1.36
	($1' \simeq 0.396$ kpc)
Mean axis ratio, q = b/a[c]	0.28 ±0.02
Inclination, i[c]	75 °±2 °
Isophotal major diameter, D_{25}[c]	14.4 ′
Major axis PA[c]	93 °±2°
Exponential scale length (kpc)[c]	1.2
Holmberg radius, R_{HO}[c]	13.3 ′
Absolute magnitude, M_B[c]	−16.35
Total luminosity, L_B	$5.19 \times 10^8\ L_\odot$
Helio. radial velocity ($km\,s^{-1}$)[c]	404 ±3

[a]De Vaucouleurs et al. (1991)
[b]Musella et al. (1997)
[c]Jobin & Carignan (1990)

Table VI gives the optical parameters of NGC 3109. In order to get sufficient signal–to–noise throughout the velocity fields, two different Gaussian spatial smoothings (σ=3.5 and 5 pixels) were performed on the cube (all the channels). Velocity maps were then obtained from the intensity weighted means of the Hα peaks to determine the radial velocity for each pixel. Final variable resolution velocity map (Fig. 17, top) was built keeping higher resolution for regions with originally higher signal-to-noise. The full resolution Hα image is also shown on the lower part of Fig. 17.

The rotation curve was obtained from the velocity field using two different methods. The first estimate was made using the task ROCUR (Begeman, 1987; Côté et al., 1991) in

[a]http://www-obs.cnrs-mrs.fr

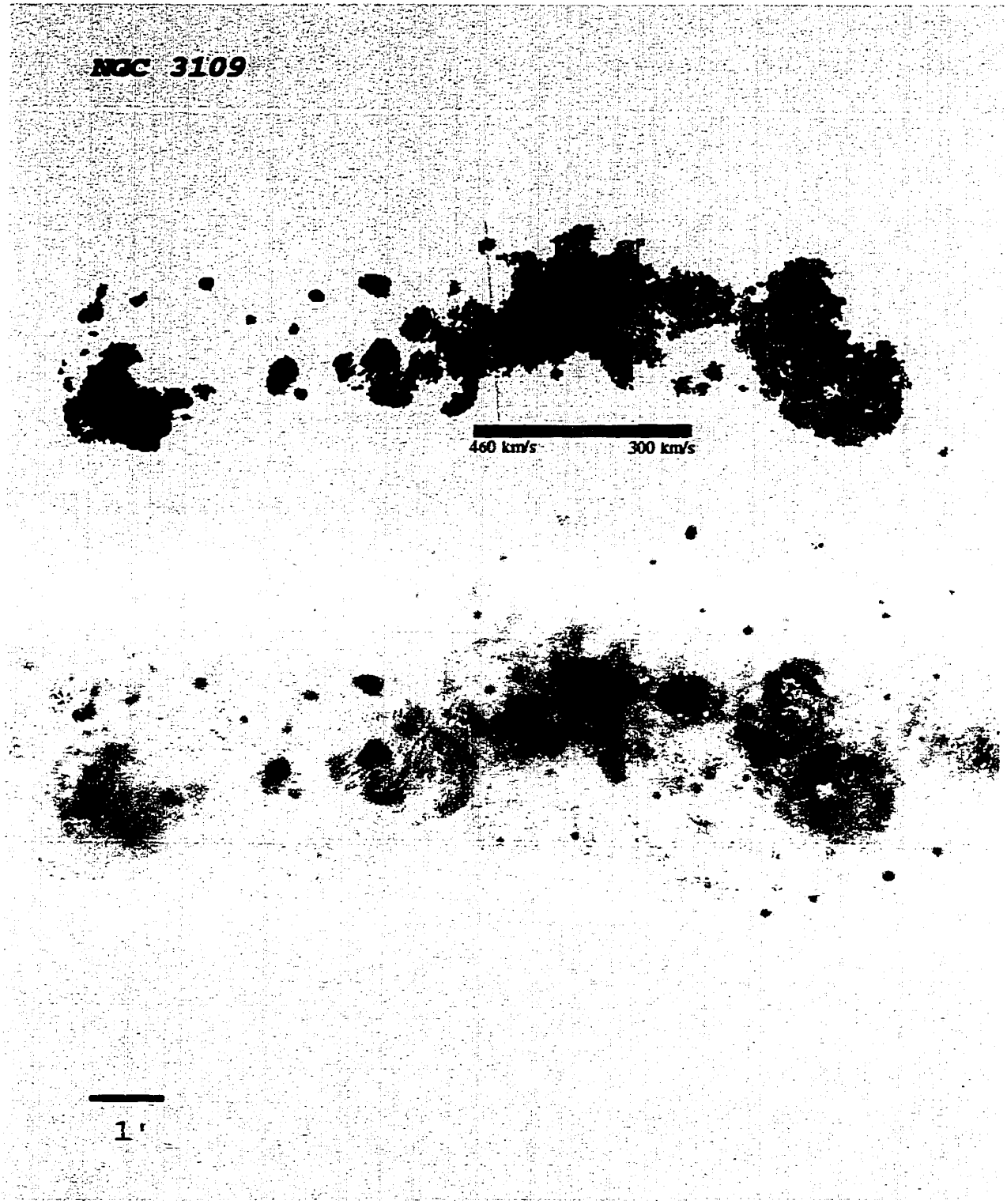

Figure 17: Velocity field and Hα image of NGC 3109. North is up and East is left. The X and the grey line indicate the kinematic center and the axis of separation between the approaching and receding sides.

the AIPS package, where annuli, tilted with respect to the plane of the galaxy (ellipses in the plane of sky), are fitted to the velocity field, minimizing the dispersion inside each ring. The dynamical center, systemic velocity, position angle and inclination were estimated this way. Secondly, the ADHOC package was used to fine–tune these parameters by comparison of both sides of the galaxy and examination of the residual velocity field (see Amram et al., 1992, for the detailed method). Systemic velocity was found to be 402 $\mathrm{km\,s^{-1}}$, very close to the value of 404 $\mathrm{km\,s^{-1}}$ found with the HI observations of Jobin & Carignan (1990). Since a warp is clearly present even in the optical velocity field, the final rotation curve was derived with ROCUR leaving the inclination and the position angle free to vary. In this context, the slightly high value of the first velocity point can be understood by the poor determination of the inclination in the center of the galaxy. Table XVII gives the full rotation curve at 20″ resolution while Fig. 18 illustrates the rotation curve as well as the variation of inclination and position angle. Following Jobin & Carignan (1990), the rotation curve was corrected for asymmetric drift.

To the present date, no convention on the way to represent the errors on rotation curves exists in the literature. Error bars are often simply given as the velocity dispersion in the ring used at each radius. However, the hot gas is known to be more sensitive to its environment than the cold gas. Turbulence, local density variations (like spiral arms, bars, etc.) and winds from stars and supernovae of the young stellar forming regions in which the ionized gas is found, increase its dispersion. This can lead to the paradox where the fewer points you have (as in long–slit observations) the lower is your dispersion and the smaller are your error bars. As a more direct probe of the uncertainties on the measured potential, the difference between the two sides of the galaxy is instead often used. Some authors will add the error due to uncertainties on inclination and/or position angles.

To clearly differentiate the source of errors, the error bars shown here indicate the error on the mean in each ring ($\sigma/\sqrt{N}$) while the solutions for each side of the galaxy are represented by lines (continuous for the receding side and dashed for the approaching). Their difference is a good estimate of the assymetry and large scale non–circular motions.

The velocity field of NGC 3109 shows many bubble–like features probably due to intense star formation especially close to the center of the galaxy. The effect of Hα bubbles are normally of two kinds: first, if the front and back sides of a bubble are equally intense and the medium transparent, a broadened or even, depending of the resolution, a doubled Hα line could be seen. The true gravitational rotation can still be deduced by averaging the two peaks. However, in many cases only the front side of an expanding bubble can be seen,

making it difficult to retrieve the true rotational velocities.

In the case of NGC 3109, analysis of the velocity field shows a small deviation from circular motion in the inner part of the galaxy. The velocity of the single innermost point of the rotation curve is slightly affected.

Despite some internal peculiar velocities, apparently well averaged out, a relatively good agreement can be seen between the two sets of data. The HI velocities (where no beam smearing correction has been applied) were just slightly underestimated in the inner part. This is not really surprising considering that beam smearing effects should diminish as the slope of the inner rotation curve lowers for a given beam width. The multi–wavelength rotation curve is thus composed of the Hα data points up to 410 $''$ and of HI velocities for the rest.

3.2.2 IC 2574

Table VII: Optical parameters of IC 2574.

Morphological Type[a]	SABm
RA (J2000.0)	$10^h\ 28^m\ 21\overset{s}{.}2$
Dec (J2000.0)	68°24′43″
l	140 °.21
b	43 °.60
Adopted distance (Mpc)[b]	3.0
	($1' \simeq 0.8$ kpc)
Mean axis ratio, q = b/a[b]	0.48 ±0.06
Inclination, i[b]	75 °±3 °
Isophotal major diameter, D_{25}[b]	9.76 ′
Major axis PA[b]	52 °±6°
Exponential scale length (kpc)[b]	2.2
Holmberg radius, R_{HO}[b]	8.63 ′
Absolute magnitude, M_B[b]	−16.77
Total luminosity, L_B	$7.94 \times 10^8\ L_\odot$
Helio. radial velocity ($km\,s^{-1}$)[b]	58 ±3

[a]De Vaucouleurs et al. (1991)
[b]Martimbeau et al. (1994)

A similar reduction procedure was applied to IC 2574 and the velocity field is shown juxtaposed to the monochromatic image in Fig. 19. The first evidence is that IC 2574 is more disrupted than NGC 3109. With such a patchy velocity field, a determination of a reliable rotation curve with an iterative method based on velocity dispersion in annuli turned out to be impossible. Direct calculation of the rotation velocity for each pixel was thus done using fixed values for the position angle and the inclination. The dynamical parameters were found

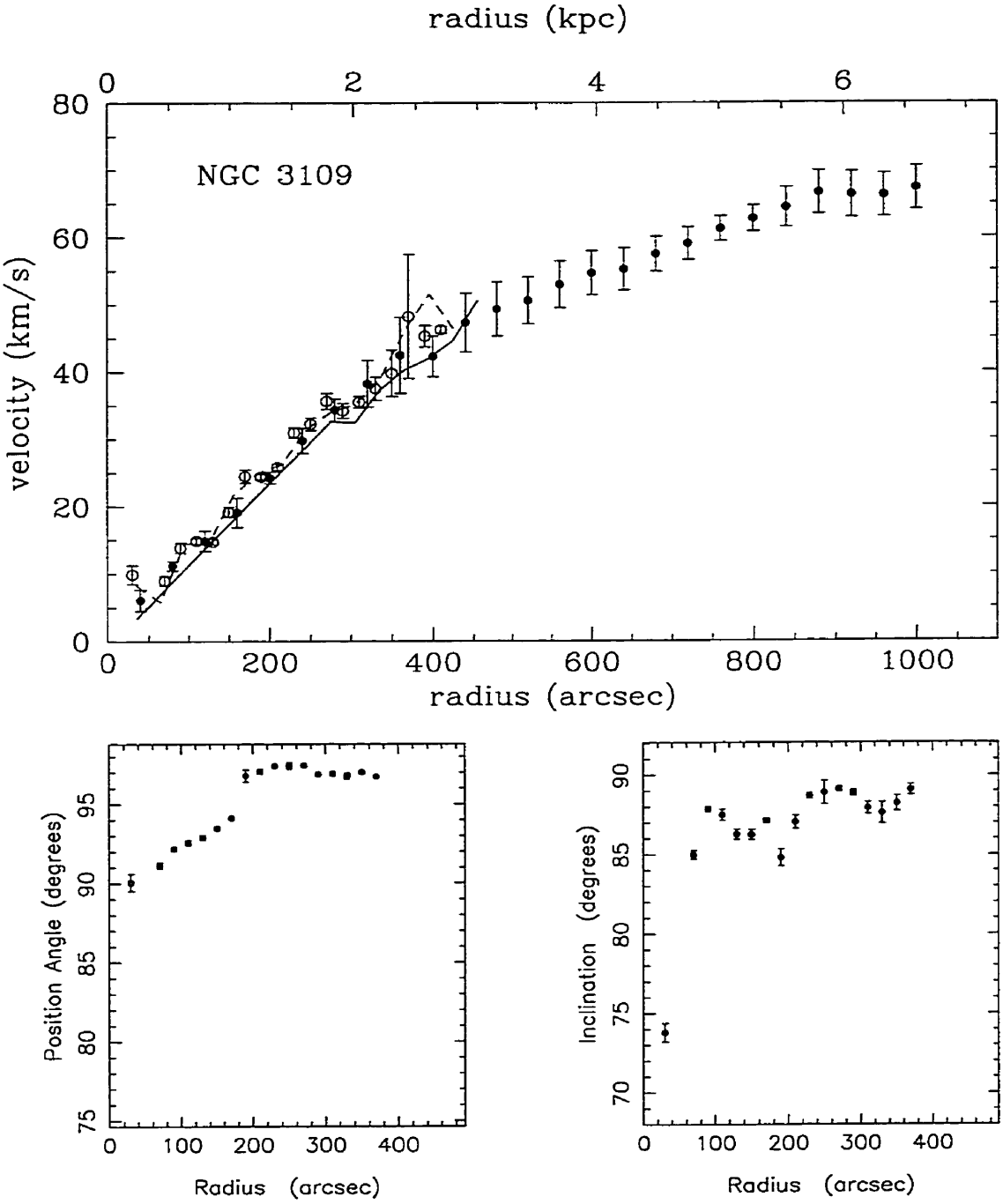

Figure 18: *Top* Hα rotation curve of NGC 3109 (open circles) compared to the HI rotation curve (filled circles) from Jobin & Carignan (1990). The approaching and receding sides are respectively represented by the dashed and continuous lines; *bottom* variation of the position angle and inclination for the Hα curve. See text for details on curves and error bars.

by comparing the two sides of the galaxy and by analyzing the residual field. The obtained rotation curve is presented in Table XVIII based on a systemic velocity of 53 $\mathrm{km\,s^{-1}}$, a position angle of 52°and an inclination of 75°, almost identical to the parameters found by Martimbeau et al. (1994) from the HI observations.

The Hα rotation curve follows more or less the same kind of perturbations as those seen in the HI curve. For example, when one compares the two sides of the HI curve in the Fig. 8 of Martimbeau et al. (1994): (i) the effect of a giant bubble can clearly be seen at both wavelengths around 240″ on the approaching side; (ii) the giant north–eastern OB association clearly shows up between 7′ and 10′ of the receding side; (iii) on another hand, some probable non-circular motions are seen around 100″ in the Hα but do not show up in the HI .

Since the Hα data show no sign of beam smearing effect, there would be no reason here to use the disrupted Hα curve instead of the 21 cm data as probe of the gravitational potential of the galaxy.

3.3 Mass Models and Parameters of the Mass Distribution

3.3.1 Comparison of different models using standard gravity

The method used in this paper to model the mass distribution is a slight generalization of the one described in Carignan & Freeman (1985).

The luminosity profile, if possible in the near infrared to probe the mass dominant stellar component, is transformed into a mass distribution for the stellar disk, assuming a variable but radially constant mass–to–light ratio ($(\mathcal{M}/\mathrm{L}_B)_\star$) (Casertano, 1983; Carignan & Freeman, 1985). For the contribution of the gaseous component, the HI radial profile is used, scaled by 1.33 to account for He. The difference between the observed rotation curve and the contribution to the curve from the luminous (stars & gas) component is thus the contribution of the dark component which can be represented by a dark spherical halo. There are therefore three free parameters, the $(\mathcal{M}/\mathrm{L}_B)_\star$ for the disk, and two parameters for the dark halo: the central density ρ_0 and the core radius r_c. A best fit routine minimizes de χ^2 in the three dimension parameter space.

Many studies approximate later type spirals such as NGC 3109 and IC 2574 as being totally made of dark matter, neglecting the stellar and gaseous components. This is a good approximation down to a certain radius. However, the innermost parts of the rotation

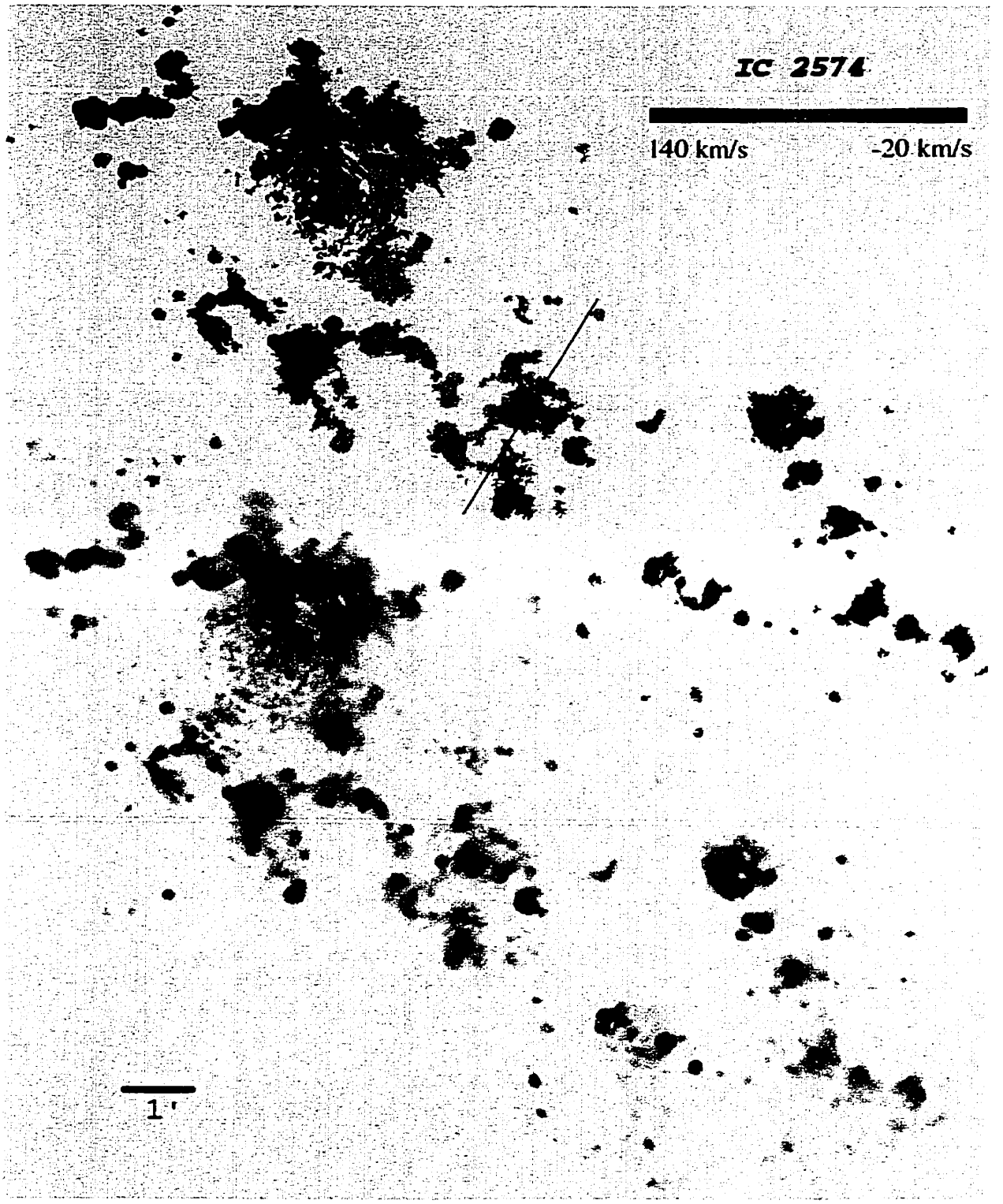

Figure 19: Velocity field and Hα image of IC 2574. North is up and East is left.

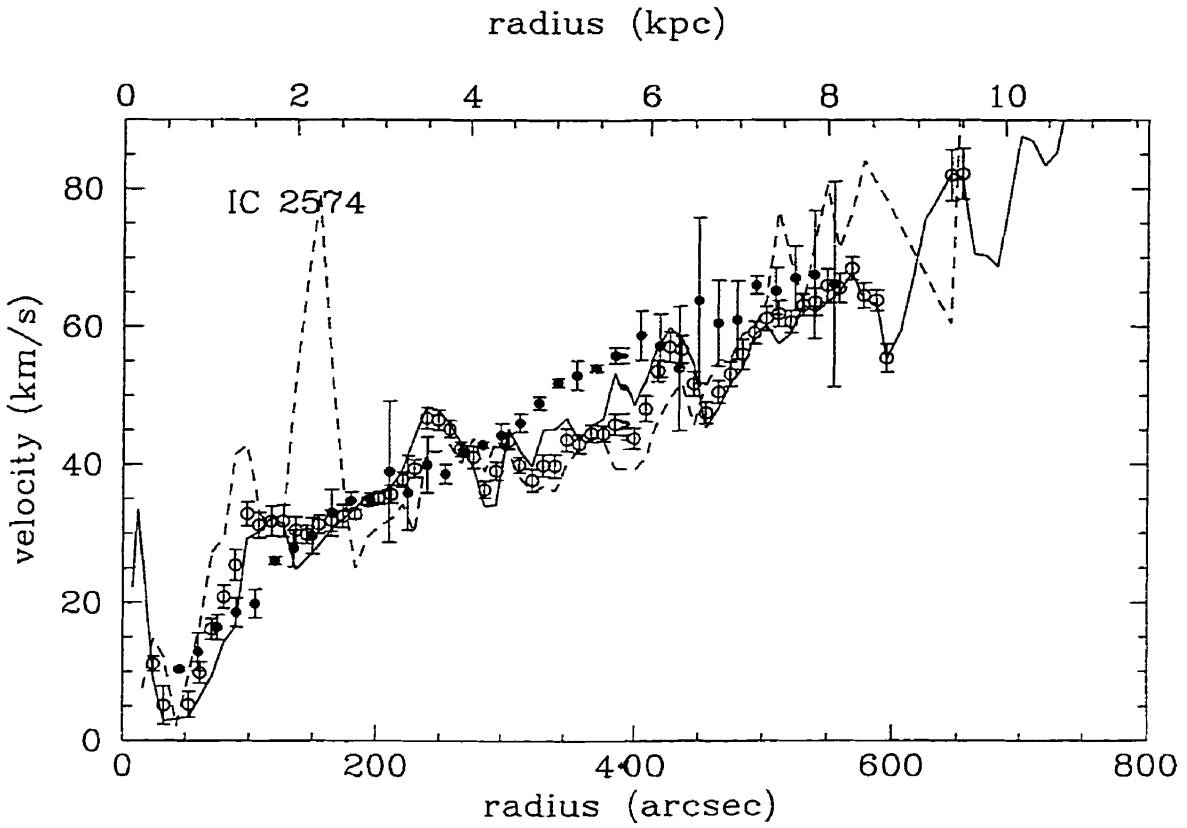

Figure 20: Hα rotation curve of IC 2574 (open circles) compared to the HI rotation curve (filled circles) from Martimbeau et al. (1994). The approaching and receding sides of the Hα curve are respectively represented by the dashed and continuous lines.

curves are crucial to test the shape of the density profiles. Best fit models that include the contributions of gas and stars are therefore used to avoid an overestimation of the dark halo contribution.

Following Kravtsov et al. (1998, hereafter KKBP) and Zhao (1996), we use an even broader family of density profiles for the halo:

$$\rho(r) = \frac{\rho_0}{(c + (r/r_0)^\gamma)\,(1 + (r/r_0)^\alpha)^{(\beta-\gamma)/\alpha}} \tag{3.1}$$

where ρ_0 and r_0 are characteristic density and radius, c=1 forces the presence of a flat density core and α, β and γ are shape parameters.

One can either fit the value of (c, α, β, γ) to a particular density profile or set them to a desired value: (1, $\alpha \neq 0$, 2, 2) for a pseudo–isothermal sphere (Begeman, 1987); (0, 1, 3, 1) for a NFW type halo (Navarro et al., 1996b); (1, 2, 3, 1) for halos with flat density

cores proposed by Burkert (1995) or (0, 2, 3, 0.2) as proposed by KKBP. These four density profiles are presented in Fig. 21. Profiles with non-constant density cores ($lim_{r\to 0}(\rho) \neq \rho_0$), are defined as cuspy. For these profiles, the inner slope is given by $-\gamma$, the outer slope by β while α controls the turnover point.

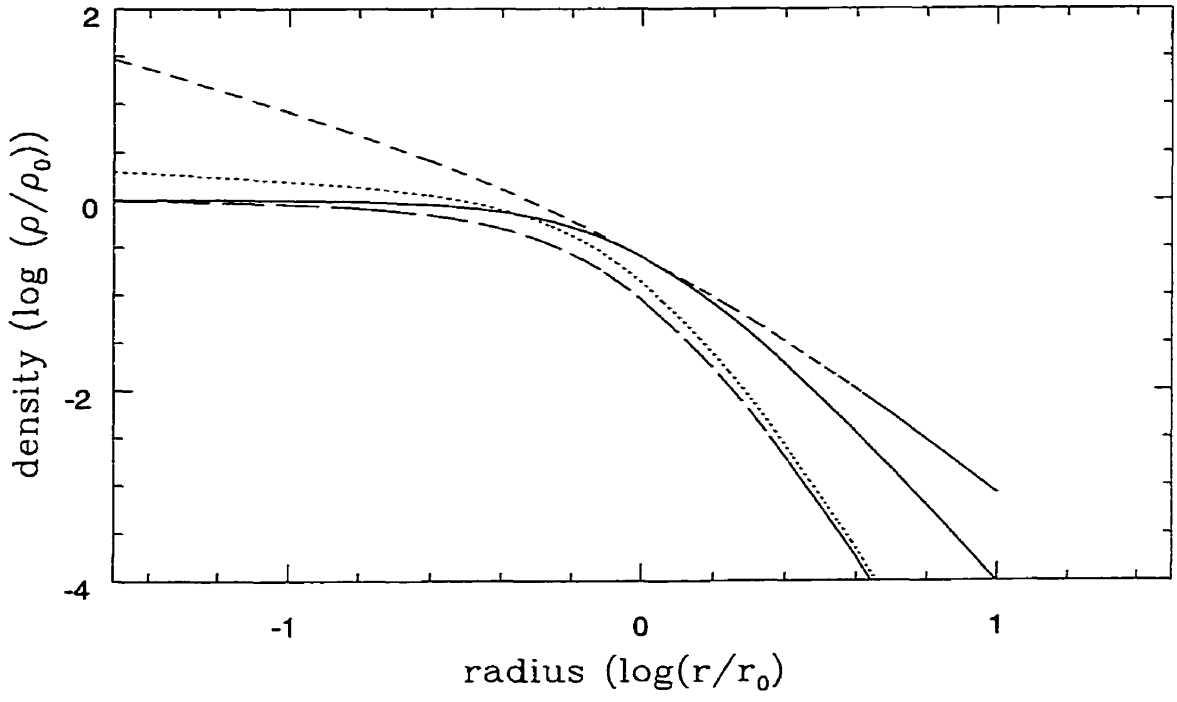

Figure 21: Density profiles of the four models. *solid*: pseudo-isothermal sphere, *dot*: KKBP, *long dash*: Burkert, *short dash*: NFW.

NGC 3109 is particularly well suited for dynamical studies: First because its luminous component is minimal (B–band photometry from Kent, 1987) so that the uncertainties related to the unknown mass–to–light ratio of the disk do not have a significant impact. Second, this galaxy is close enough to allow direct distance estimation via multicolor observation of a large number of Cepheids (Musella et al., 1997). The adopted distance is 1.36 Mpc.

In Fig. 22 and 23, best–fit models are given for the rotation curves of NGC 3109 and IC 2574 respectively. The high resolution data (used up to 410 $''$ for NGC 3109) remove some uncertainties pointed out by Navarro (1997) on the difference in HI curves coming from different generations of radio-telescopes (single dish and aperture synthesis). It confirms the great difficulty to reconcile the cuspy profile with $\gamma \geq 1$ and the rotation curve of a late type spiral like NGC 3109. Either constant density core profiles or mildly cuspy profiles with

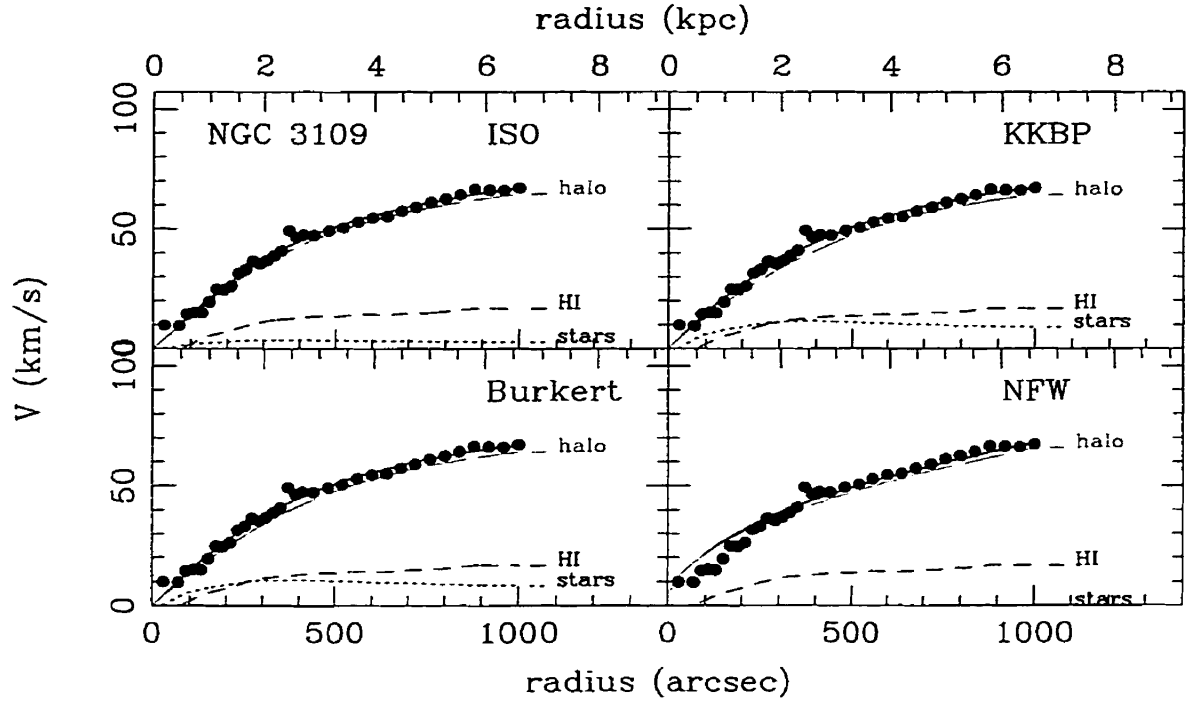

Figure 22: Best fit mass models for NGC 3109 using the Hα rotation curve up to 2.7 kpc and the HI rotation curve for the rest. The dark halos density profiles are *top–left*: pseudo-isothermal sphere, *top–right*: KKBP, *bottom–left*: Burkert, *bottom–right*: NFW.

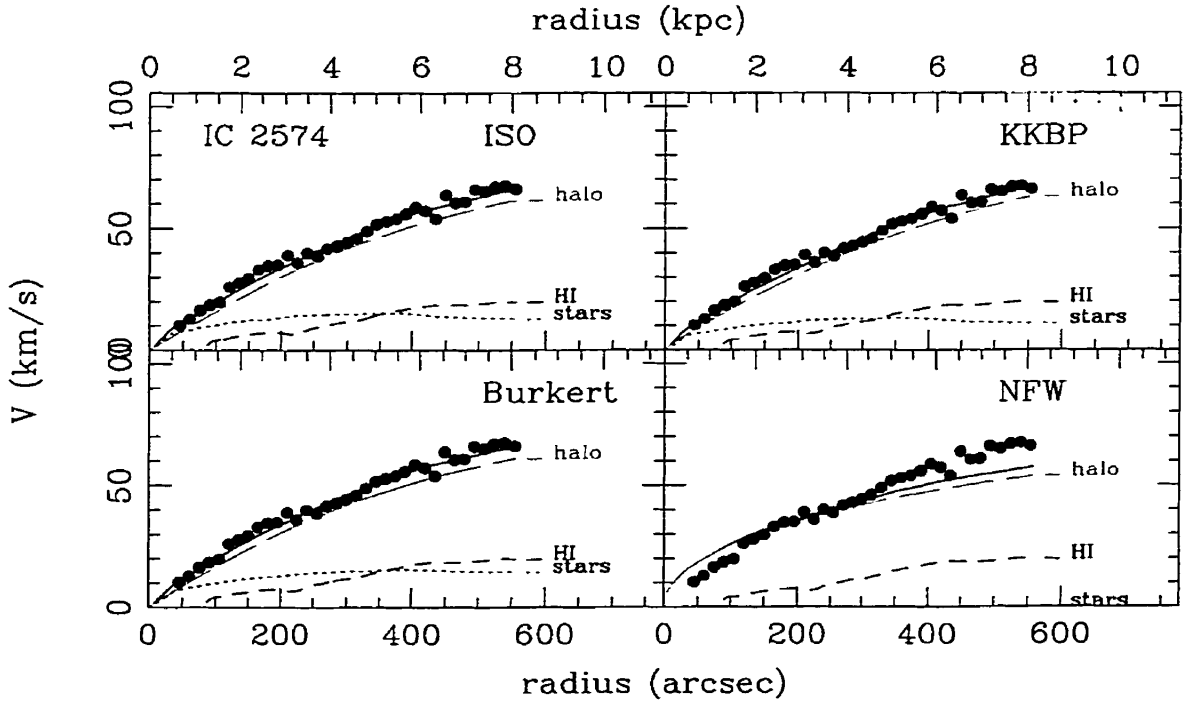

Figure 23: Mass models of IC 2574 using the HI rotation curve only.

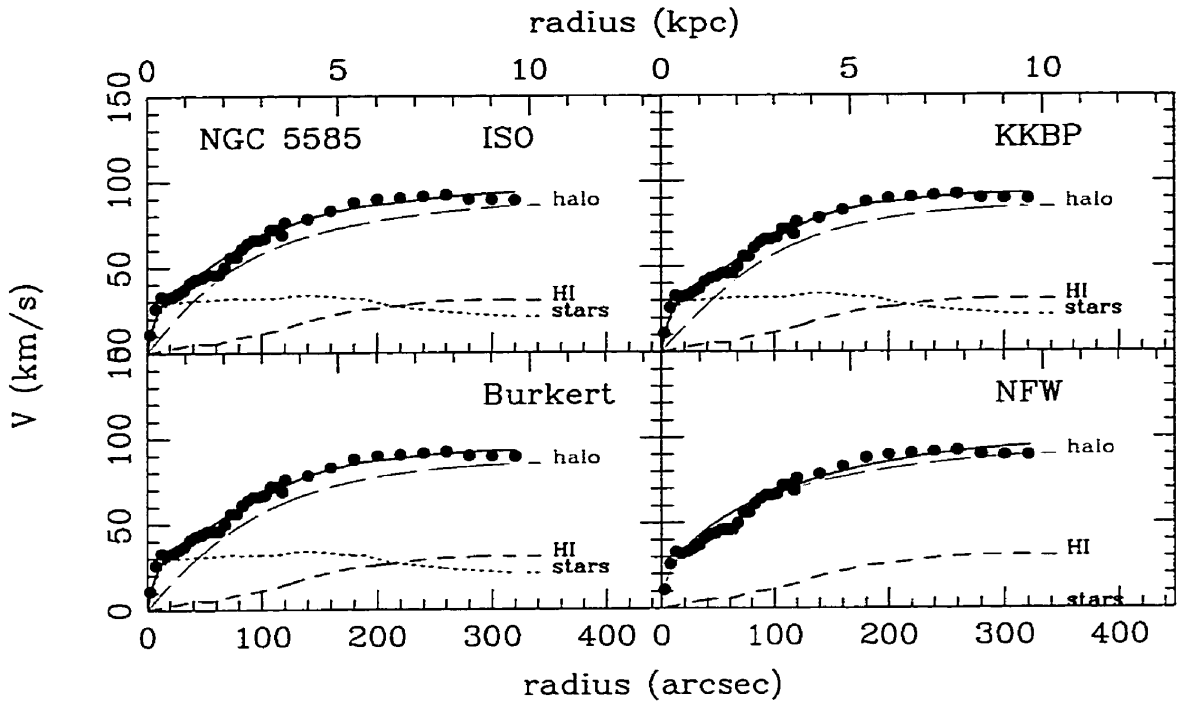

Figure 24: Mass models of NGC 5585 using the Hα rotation curve up to 3.5 kpc and HI for the rest.

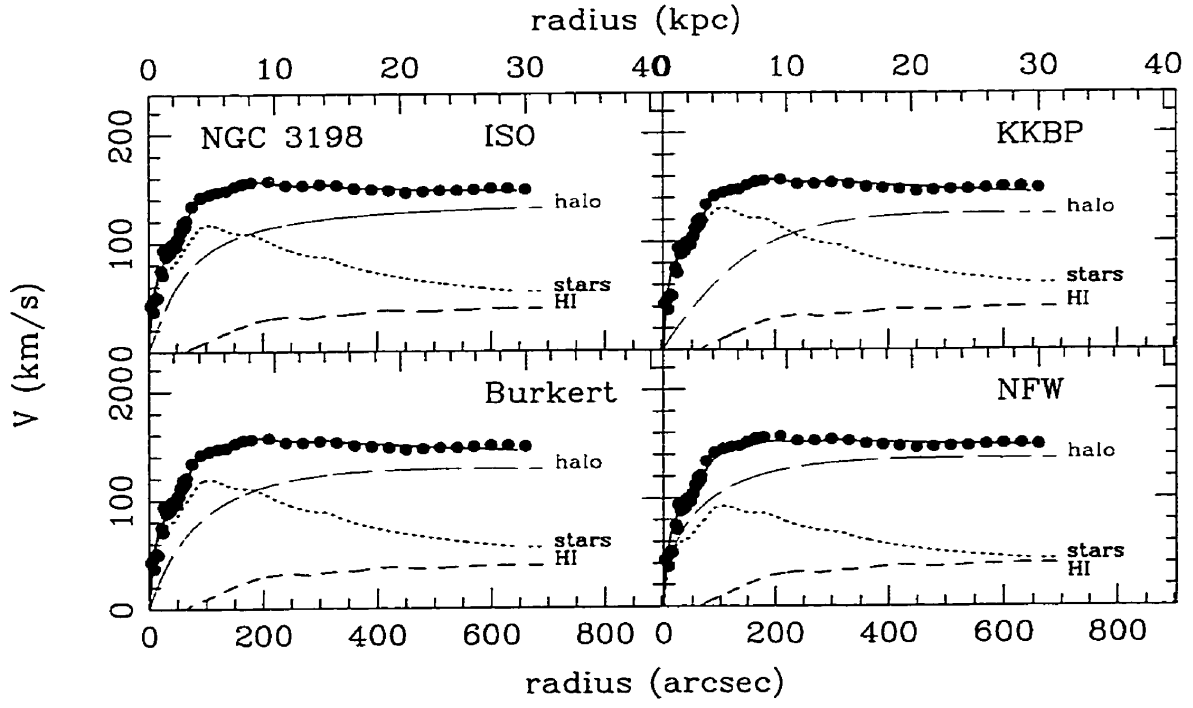

Figure 25: Mass models of NGC 3198 using the Hα rotation curve up to 2.9 kpc and HI for the rest.

$\gamma \ll 1$ can fit the data adequately. It is very difficult to discriminate between a density distribution with a flat core from one with a mild cusp because r_0 can often be stretched to a point where the two types of profile match. One has to go to very small radii ($\lesssim \gamma r_0$) to really probe any incompatibility.

Cuspy profiles with $\gamma \geq 1$ seem naturally obtained from CDM N-body simulations but many models have been suggested that deviate somewhat from the standard CDM assumptions and avoid the creation of a steep central density cusp. As noted by KKBP, Syer & White (1998) showed that γ is sensitive to the past merger rate and to the perturbation power spectrum on the scale of a galactic halo. Therefore a less active merger history or a steeper power spectrum should lead to $\gamma < 1$ on galactic scale. Self-interacting dark matter (Spergel & Steinhardt, 1999) has also been suggested to suppress the formation of high density dark matter cusp but the implied inverse dependency of the core radius on the mass of the galaxy (Dalcanton & Hogan, 2000) is not observed in our sample.

Alternatively, in order to explain the presence of flat density core in dwarf spirals for standard, scale free CDM models, Navarro et al. (1996a) suggested that violent starburst could eject the gas and consequently flatten the inner dark matter distribution. Semi-analytical calculations gives this scenario the right order of magnitude for a low mass galaxy given a sufficient feedback efficiency (van den Bosch et al., 2000).

Another way to reconcile the too steep rotation curves without invoking a flat density CDM core is to add a second, compact object component to the non–baryonic cold dark matter (Burkert & Silk, 1997). Of course this adds some degrees of freedom when fitting rotation curves and a better fit is in this case somewhat meaningless, making this hypothesis hard to test. A better knowledge of the importance and distribution of Massive Compact Halo Objects (MACHOs) in our own Galaxy would address the relevance of this hypothesis.

NGC 5585 is also well fitted by all the profiles but the NFW (24). The slight difference between the $(\mathcal{M}/\mathrm{L}_B)_\star$ found here (0.85) and the one found in paper I (0.80) is due to the use of the equation 3.1 instead of the integration of the Poisson's equation of the isothermal sphere.

In the case of NGC 3198 (Fig. 25), all the profiles are compatible. The Hα curve has been used up to 65 $''$ to rectify the overcorrection of the beam smearing in Begeman (1987). The only remark to be made is that all the profiles are too smooth to account for the small variations in the outer rotation curve, even though they are present in both the HI and the B profile. The detailed gravitational interplay between luminous and dark matter

Table VIII: Parameters of the mass models

Model	Galaxy	Type	$(\mathcal{M}/L_B)_\star$	r_0 kpc	ρ_0 $10{-}3\mathcal{M}_\odot/pc^{-3}$	χ^2
ISO	IC 2574	SABm	0.34	5.4	7.0	2.7
	NGC 3109	SBm	0.04	2.35	2.50	2.8
	NGC 5585	SABd	0.85	2.15	4.25	4.4
	NGC 3198	SBc	4.80	2.54	5.70	7.1
Burkert	IC 2574	SABm	0.6	8.0	8.4	2.5
	NGC 3109		0.35	4.1	2.50	2.9
	NGC 5585		0.086	4.0	4.0	8.21
	NGC 3198		5.0	5.8	7.40	7.70
KKBP	IC 2574	SABm	0.25	9.2	5.0	2.43
	NGC 3109		0.4	4.5	1.45	2.9
	NGC 5585		0.86	3.9	5.6	7.4
	NGC 3198		6.0	9.15	1.14	9.1
NFW	IC 2574	SABm	0.0	35	0.05	44.0
	NGC 3109		0.00	109	0.024	10.18
	NGC 5585		0.00	10.1	0.77	7.86
	NGC 3198		3.0	11.20	1.27	44.4

should be taken into account.

3.3.2 Modified Newtonian Dynamics

Proposed by Milgrom (1983b), a modification of Newtonian gravitation in the low acceleration limit can mimic a large amount of dark matter in spiral galaxies. MOND is a truly falsifiable theory: it contains only one parameter, a_0, that is supposed to be a universal constraint. A lot of work has been done using rotation curves where the quality of the data gives the best opportunity to test the theory (e.g. Begeman et al., 1991; Sanders, 1996; Sanders & Verheijen, 1998; McGaugh & De Blok, 1998).

As a reminder, here is the MOND quantitative prescription. For purely circular motion, one can equate the centripetal acceleration and gravitational acceleration. In the Newtonian regime, we simply get the common

$$\frac{V^2}{R} = \frac{GM_T}{R^2} = g_N \tag{3.2}$$

The MOdified Newtonian Dynamics (MOND) state that the true acceleration is given by

$$\mu(g/a_0)\mathbf{g} = \mathbf{g}_N \tag{3.3}$$

where $\mu(g/a_0)$ is an interpolation function that has the right asymptotic behavior: $\mu(g/a_0 \gg 1) \to 1$ and $\mu(g/a_0 \ll 1) \to g/a_0$.

Table IX: MOND parameters when using the best fitted a_0.

Galaxy	Distance Mpc	a_0 $\times 10^{-13}$ km/s^2	$(\mathcal{M}/L_B)_\star$	χ^2 $\mathcal{M}_\odot/L_\odot$
IC 2574	3.0	2.0	0.02	1.51
NGC 3109	1.36	2.68	0.12	4.99
NGC 5585	6.2	2.45	0.34	5.94
NGC 3198	9.36	0.9	6.71	1.11

The exact form of $\mu(g/a_0)$ has no impact on the mass models of very late type spirals like NGC 3109 and IC 2574 where the gravitational acceleration is well below a_0 at all radii but in general, the commonly used

$$\mu(x) = \frac{x}{\sqrt{1+x^2}} \tag{3.4}$$

is assumed to be the interpolation function.

In the limit of low acceleration the gravitational acceleration is thus given by $g = \sqrt{a_0 g_N}$ and

$$\frac{V^2}{R} = \sqrt{\frac{GM_T}{R^2} a_0} \tag{3.5}$$

or

$$V^4 = GM_T a_0 \tag{3.6}$$

which naturally explains the asymptotic flatness of rotation curves and the Tully-Fisher relation.

A best–fit method, similar to the one used for dark halos has been applied. The stellar luminosity profile and the HI density profile are this time transformed into a mass distribution following equations (3.3) and (3.4). The free parameter of the fit is as always the $(M/L)_\star$ ratio. a_0 is considered as a universal constant but since no fundamental theory exists as of yet to give its true value, four different values are used in the fits. First, the value found by Begeman et al. (1991) that best fits their highly selective and high quality sample (1.2×10^{-13} km s^{-1}). The second value is the one that best fits each present galaxy individually (Table IX). The two other values are educated guesses of what could be a_0 in an underlying theory, as suggested by Milgrom (1998). For instance, $cH_0 = 6.8 \times 10^{-13}$ km/s^2 where c is the speed of light and $H_0 = 71 \pm 6$ km s^{-1} (Mould et al., 2000) and $c^2\sqrt{\Lambda} = 7.8 \times 10^{-13}$ km/s^2 where $\Lambda \simeq 2.3 \times 10^{-51}$ cm^{-2} if $\Omega_M = 0.3$ as indicated by the recent data on high redshift supernovae (Perlmutter et al., 1999). Fig. 26 shows the best fit for each galaxy and Table IX indicates the parameters when using the best fitted a_0.

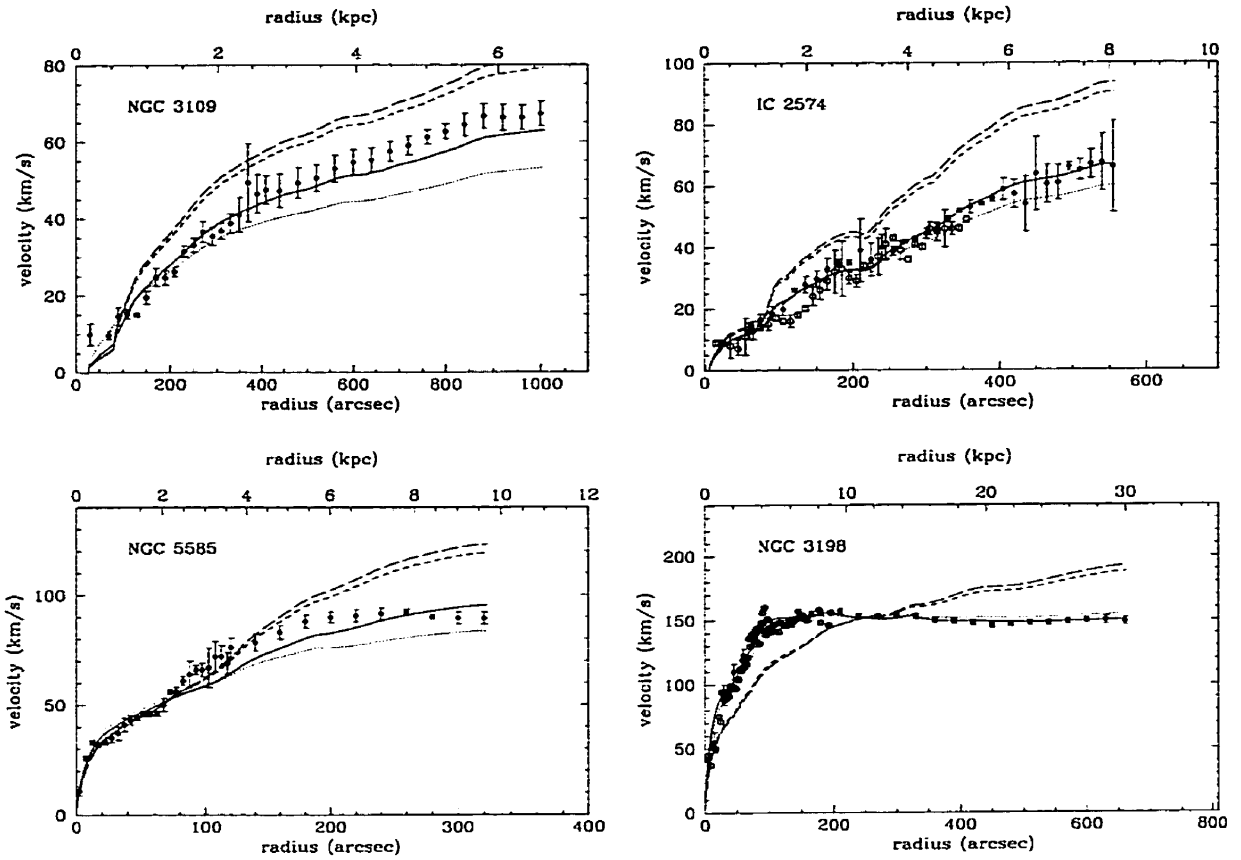

Figure 26: Best fit mass models using the Modified Newtonian Dynamics. Four different values of a_0 are used. Dotted line: 1.2 $\times 10^{-13}$ km/s^2 (from Begeman et al., 1991), continuous line: best fit value (see Table IX), short dash: $cH_0 = 6.8 \times 10^{-13}$ km/s^2 and long dash: $c^2\sqrt{\Lambda} = 7.8 \times 10^{-13}$ km/s^2. The filled circles represent the data used in the fits (HI +Hα for NGC 3109 and 5585 and HI only for IC 2574 and NGC 3198). The open circles indicates the Hα velocities unused in the fits.

IC 2574 and NGC 3198 are fairly well fitted by the MOND law if the "universal constant" a_0 is let free to vary by more than a factor 2. The quality of the fit is especially good in the case of IC 2574 where most of the features of the rotation curve are reproduced in the fit. On the other side, the MOND prescription has more difficulties to account for the mass distribution of NGC 3109 and NGC 5585 whatever the value of a_0. Being for large part in the Newtonian regime, the case of NGC 5585 is somewhat less significant as it probes more the interpolation function than the MOND theory itself. At the opposite, NGC 3109 belongs fully to the MOND regime. Even though the Hα velocities are somewhat higher than the HI near the center, the rise of the rotation curve is still too shallow to be compatible with MOND. The uncertainties on NGC 3109 rotation curve have been seriously narrowed and the improved rotation curve still put the MOND theory in difficulty.

3.4 Summary and Discussion

With the four galaxies studied so far, it is clear that while there is a good agreement between Fabry-Perot and HI data for the shallow rotation curves of the late type galaxies NGC 3109 and IC 2574, the beam smearing plays an important role for the steeper rotation curves. The beam smearing thus seems to depend on at least two factors: the inner slope of the rotation curve and the sampling of the curve, often expressed as the ratio of the Holmberg radius to the beam width (Bosma, 1978). Bosma suggested a ratio greater than 6 to have reliable HI curve. This ratio is about 9 for NGC 5585 and 30 for NGC 3109 and the latter is still slightly affected by beam smearing.

Using the multi-wavelength rotation curves to determine the density profiles of dark matter halos, it appears clearly that cuspy profiles with inner logarithmic slope $\gamma \geq 1$ do not match the observations. The best fits are achieved using either a slightly cuspy profile with a very shallow inner slope or a profile with a flat density core. If most of the simulations describe a realistic CDM evolution, an additional process is needed to destroy or forbid the formation of a central cusp. However, none of the actually proposed scenarios stand out as the most plausible either because they are not easily testable or their predictions do not appear clearly in the data.

The Modified Newtonian Dynamics prescription can fit the rotation curves of IC 2574 and NGC 3198 obtained from the new high resolution data if a_0 is free to vary by a factor of 2. In this case, most of the features of the rotation curve are even reproduced with the right amplitude. Of course, since there is almost no stellar disk, at least in the part fully in the MOND regime, scaling the HI would produce a similar result. Can H_2 be involved here? (Pfenniger et al., 1994). On the other hand, the variations of the stellar and gaseous components also possibly just follow a non–smooth dark matter distribution.

Things are quite different in the case of NGC 3109. The slight increase of the inner velocities brought by the Hα data is not sufficient to significantly improve the compatibility between the MOND theory and this galaxy even if the uncertainties have been seriously narrowed. It has to be noted though, that the amplitude of the features in the curve are also well reproduced here.

There is always a danger to let what should be a universal constant like a_0 vary to fit the data. However, since no underlying theory exists yet, it is interesting to note that for these late type spirals, a_0 seems systematically higher than for the earlier types.

3.5 Conclusion

The present work leads to the following conclusions:

• Observations of the kinematics of the ionized hydrogen in NGC 3109 and IC 2574 is in good agreement with the previous kinematical studies of the atomic hydrogen. This implies that the beam smearing was limited in the HI data although NGC 3109 was slightly affected.

• Overall, beam smearing can be important even for "good sampling" (20 beam widths per Holmberg radius for NGC 5585) depending on the inner slope of the rotation curve.

• The CDM models with a inner density slope $\gamma \geq 1$ are not compatible with the data on NGC 3109 and IC 2574. Flat density core models like the pseudo-isothermal sphere or a model with a shallow inner density slope are compatible with the four galaxies in our sample.

• The MOND prescription can fit the rotation curves of NGC 2574 and NGC 3198 if the "universal constant' a_0 is free to vary by more than a factor of 2. It is however unable to reproduce the mass distribution of NGC 3109 and NGC 5585 whatever the value of a_0.

The present examples give a good idea of the impact of higher resolution rotation curves. There is however large unexplored regions in terms of galaxy mass, surface brightness and morphological types. It is thus imperative to extend this sample to earlier type galaxies covering a large range in surface brightness. This would give, among other things, the opportunity to study precisely at what point the rotation curves stop agreeing with N-body simulations.

We would like to thank the staff of the CFHT for their support during the data acquisition and Daniel Durand from DAO who helped with data acquisition. We also warmly thank Jacques Boulesteix for fruitful discussion on Fabry-Perot reduction and Piotr Popowski for valuable comments. CC acknowledges grants from NSERC (Canada) and FCAR (Québec).

References

Amram, P., Marcelin, M., Boulesteix, J., & Le Coarer, E. 1992, A&A, 266, 106

Begeman, K. 1987, PhD thesis, Rijksuniversiteit Groningen

Begeman, K. G. 1989, A&A, 223, 47

Begeman, K. G., Broeils, A. H., & Sanders, R. H. 1991, MNRAS, 249, 523

Blais-Ouellette, S., Carignan, C., Amram, P., & Côté, S. 1999, AJ, 118, 2123

Bosma, A. 1978, PhD thesis, Rijksuniversiteit Groningen

—. 1981, AJ, 86, 1791

Broeils, A. 1992, PhD thesis, Rijksuniversiteit Groningen

Burkert, A. 1995, ApJ, 447, L25

Burkert, A. & Silk, J. 1997, ApJ, L55

Carignan, C. & Freeman, K. C. 1985, ApJ, 294, 494

Casertano, S. 1983, MNRAS, 203, 735

Corradi, R. L. M., Boulesteix, J., Bosma, A., Amram, P., & Capaccioli, M. 1991, A&A, 244, 27

Côté, S., Carignan, C., & Sancisi, R. 1991, AJ, 102, 904

Dalcanton, J. J. & Hogan, C. J. 2000, astro-ph/0004381

De Vaucouleurs, G., De Vaucouleurs, A., Corwin, Herold G., J., Buta, R. J., Paturel, G., & Fouque, P. 1991, Third Reference Catalogue of Bright Galaxies (Volume 1-3, XII, 2069 pp. 7 figs.. Springer-Verlag Berlin Heidelberg New York)

Fukushige, T. & Makino, J. 1997, ApJ, 477, L9

Jobin, M. & Carignan, C. 1990, AJ, 100, 648

Kent, S. M. 1987, A.J., 93, 816

Kravtsov, A. V., Klypin, A. A., Bullock, J. S., & Primack, J. R. 1998, ApJ, 502, 48

Martimbeau, N., Carignan, C., & Roy, J.-R. 1994, AJ, 107, 543

McGaugh, S. S. & De Blok, W. J. G. 1998, ApJ, 499, 41

Milgrom, M. 1983, ApJ, 270, 365

Milgrom, M. 1998, in Second International Workshop on Dark Matter, ed. H. Klapdor-Kleingrothaus & L. Baudis

More, B., Governato, F., Quinn, T., Stadel, J., & Lake, G. 1998, ApJ, 499, L5

Mould, J. R., Huchra, J. P., Freedman, W. L., Kennicutt, R. C., Ferrarese, L., Ford, H. C., Gibson, B. K., Graham, J. A., Hughes, S. M. G., Illingworth, G. D., Kelson, D. D., Macri, L. M., Madore, B. F., Sakai, S., Sebo, K. M., Silbermann, N. A., & Stetson, P. B. 2000, ApJ, 529, 786

Musella, I., Piotto, G., & Capaccioli, M. 1997, AJ, 114, 976

Navarro, J. F. 1997, in ASP Conf. Ser. 117: Dark and Visible Matter in Galaxies and Cosmological Implications, 404

Navarro, J. F., Eke, V. R., & Frenk, C. S. 1996a, MNRAS, 283, L72

Navarro, J. F., Frenk, C. S., & White, S. D. M. 1996b, ApJ, 462, 563

—. 1997, ApJ, 490, 493

Perlmutter, S., Aldering, G., Goldhaber, G., Knop, R. A., Nugent, P., Castro, P. G., Deustua, S., Fabbro, S., Goobar, A., Groom, D. E., Hook, I. M., Kim, A. G., Kim, M. Y., Lee, J. C., Nunes, N. J., Pain, R., Pennypacker, C. R., Quimby, R., Lidman, C., Ellis, R. S., Irwin, M., McMahon, R. G., Ruiz-Lapuente, P., Walton, N., Schaefer, B., Boyle, B. J., Filippenko, A. V., Matheson, T., Fruchter, A. S., Panagia, N., Newberg, H. J. M., Couch, W. J., & Project, T. S. C. 1999, ApJ, 517, 565

Pfenniger, D., Combes, F., & Martinet, L. 1994, A&A, 285, 79

Sanders, R. H. 1996, ApJ, 473, 117

Sanders, R. H. & Verheijen, M. A. W. 1998, ApJ, 503, 97

Spergel, D. & Steinhardt, P. 1999, astro-ph/9909386

Syer, D. & White, S. D. M. 1998, MNRAS, 293, 337

van den Bosch, F. C., Robertson, B. E., Dalcanton, J. J., & de Blok, W. J. G. 2000, AJ, 119, 1579

Zhao, H. 1996, MNRAS, 278, 488

Chapitre 4

Agrandir l'échantillon

ACCURATE DETERMINATION OF THE MASS DISTRIBUTION IN SPIRAL GALAXIES. III. Fabry-Perot Observations of 6 Spiral Galaxies

SÉBASTIEN BLAIS-OUELLETTE[a,b]
Département de physique and Observatoire du mont Mégantic, Université de Montréal, C.P. 6128, Succ. centre ville, Montréal, Québec, Canada. H3C 3J7 and
Observatoire de Marseille, 2 Place Le Verrier, F–13248 Marseille Cedex 04, France
e–mail: blaisous@llnl.gov

PHILIPPE AMRAM[a]
Observatoire de Marseille, 2 Place Le Verrier, F–13248 Marseille Cedex 04, France
e–mail: amram@observatoire.cnrs-mrs.fr

CLAUDE CARIGNAN[a]
Département de physique and Observatoire du mont Mégantic, Université de Montréal, C.P. 6128, Succ. centre ville, Montréal, Québec, Canada. H3C 3J7
e–mail: carignan@astro.umontreal.ca

To be submitted to Astronomy and Astrophysics Supplement Series

New high resolution Fabry–Perot data of six spiral galaxies are presented in this study. This extends the previous sample of spiral galaxies studied with high resolution 3–D spectroscopy to earlier morphological types. All the galaxies in the sample have published HI data at 21 cm from the VLA or Westerbork. Velocity fields are analyzed and Hα rotation curves are computed and compared to HI curves.
Most of the Hα rotation curves present a significantly steeper inner slope than their HI counterparts. The 21 cm data thus seems affected by moderate to strong beam smearing. The beam smearing seems to have an effect at higher scale-length/beam-width than previously thought (up to 20 km/s at a ratio of 8.5).

---

[a]Visiting Astronomers, Canada–France–Hawaii Telescope, operated by the National Research Council of Canada, the Centre National de la Recherche Scientifique de France, and the University of Hawaii.

[b]Present address: Institute of Geophysics and Planetary Physics, Lawrence Livermore National Laboratory, P.O Box 808, CA 94551-0808.

4.1 Introduction

This is the third paper in a series on high resolution Fabry-Perot spectroscopy of spiral galaxies. The first paper (Blais-Ouellette et al., 1999, hereafter paper I) showed that optical integral field spectroscopy is necessary to estimate correctly the rotation curve in the inner parts of spiral galaxies. The main reason is that HI rotation curves are affected by beam smearing, a natural consequence of their low spatial resolution (Begeman, 1987; Swaters, 1999; van den Bosch et al., 2000). In combination with paper II (Blais-Ouellette et al., 2000a), it also brought to light the great sensitivity of the mass distribution parameters to the inner rotation curve. The ideal rotation curve is therefore a combination of high resolution optical (see also Sofue et al., 1999) integral field spectroscopy and sensitive HI radio observations.

Paper II has also shown the difficulties in reconciling dwarf and late type galaxies rotation curves with standard CDM N-body simulations. Most of them (e.g. Navarro et al., 1996b, 1997; More et al., 1998) predict a much steeper inner slope than observed in these galaxies. Other studies (Kravtsov et al., 1998; Bullock et al., 1999) obtain much shallower profiles, compatible with the observations. Rotation curves of all galaxy types were also shown to be compatible with flat core density profiles. Many dwarf galaxies were also found to be incompatible with MOdified Newtonian Dynamics (MOND Milgrom, 1983b).

Since a low central density profile would be hard to explain in massive galaxies (Navarro et al., 1996a; Burkert & Silk, 1999; Spergel & Steinhardt, 1999; Dalcanton & Hogan, 2000) and since the surface density should directly vary with surface brightness in MOND, it seems now crucial to extend the sample of multi-wavelength rotation curves to earlier morphological types and lower surface brightnesses.

The present study adds six spiral galaxies to the multiwavelength rotation curve sample, all of them having been observed at 21 cm. It extends the sample to earlier types spirals, hence covering most of the morphological types, with an emphasis on late types where the impact of optical data seems the most important. Indeed, the stellar disk and dark halo of these galaxies have comparable contribution to the mass inside the Holmberg radius. Therefore, a slight change in the slope of the rotation curve can dramatically change the dark matter distribution by considerably augmenting or reducing the fitted disk contribution.

Section 4.2 briefly describes the sample while section 4.3 explains the Fabry–Perot observations and data reduction. The subsequent sections present each galaxy in some detail. Computed Hα velocity fields and rotation curves are introduced, briefly described, and compared to HI rotation curves. Dynamical analysis and mass models will be given in a

Table X: Parameters of the sample. Columns 4,5,6,10 and 11 from the main reference unless otherwise specified.

Name	Type	Dist. Mpc	D_{25} $'$	R_{HO} $'$	α^{-1} $''$	i[a] $^\circ$	PA[a] $^\circ$	V_{sys}[a] $km\,s^{-1}$	M_B	L_B $10^8 L_\odot$	Ref.
UGC 2259	SBcd	9.6[i]	2.6	1.9	28.2	41	165	581	-17.03	9.7	b
NGC 2403	SABcd	3.2[c]	21.9	13.0	134	61	126	137	-19.50	93.6	e
NGC 6946	SABcd	6.2[f]	11.5	7.8	115.2	38	60	47	-21.38	530	d
NGC 5055	SAbc	9.2[i]	12.6	9.8	108.9	62	102	501	-21.13	422	g
NGC 2841	SAb	18[h]	11.3	6.2	52	66	150	633	-21.93	880	d
NGC 5985	SABb	33.5[i]	5.5	2.7	29.9	58	15	2515	-21.74	738	a

[a]This study
[b]Carignan et al. (1988)
[c]Freedman (1990)
[d]Begeman (1987)
[e]Carignan et al. (1990)
[f]Sharina et al. (1997)
[g]Thornley & Mundy (1997)
[h]Aaronson & Mould (1983)
[i]$H_0 = 75\,km\,s^{-1}$/Mpc

Col 4: Diameter at the 25 B-mag/arcsec^2 isophote
Col 5: Holmberg radius
Col 6: Scale length
Col 7: Inclination
Col 8: Position angle of the major axis
Col 9: Systemic heliocentric velocity
Col 10: Absolute B magnitude
Col 11: Total B luminosity

forthcoming paper (paper IV).

4.2 The Sample

Table X summarizes the optical parameters of each galaxy in the sample. Neutral hydrogen kinematics and mass models of UGC 2259 and UGC 6946 have been studied by C. Carignan and collaborators (Carignan et al., 1988, 1990) while NGC 2403 and NGC 2841 are part of K. Begeman's thesis (Begeman, 1987). All these studies present rotation curves based on 21 cm observations from the Westerbork Synthesis Radio Telescope (WSRT). NGC 5985, has not yet been the object of a detailed kinematical study and no rotation curve can be found in the literature. However, the HI velocity field is available through the WHISP project (Westerbork HI survey of SPiral galaxies, Swaters private communication) and a rotation curve can be extracted from it. An HI rotation curve of NGC 5055, based on VLA observations, have been presented by Thornley & Mundy (1997).

This sample expand the range of morphological types from the very late types of paper II to late (Sc, Scd) and earlier (Sbc, Sb) type. It is aimed to be a foretaste of the GHASP survey (Gassendi, Hα survey of SPiral galaxies), a Fabry-Perot survey of more than 300 spiral galaxies[a].

[a]http://www-obs.cnrs-mrs.fr

4.3 Fabry–Perot Observations: Data Acquisition and Reduction

All the Fabry-Perot observations have been initially made at the Canada–France–Hawaii Telescope (CFHT) in two successful runs in September 97 and March 98 using the CFHT1 high resolution Fabry-Perot etalon (1162) installed in the Multi–Object Spectrograph (MOS) focal reducer. A narrow–band filter ($\Delta\lambda \simeq 12$ Å), centered around the systemic velocity of the observed object, was placed in front of the etalon. The available field with negligible vignetting was $\approx 8.5' \times 8.5'$, with $0.44''$ pix^{-1}. The free spectral range of 5.66 Å (258 km s^{-1}) was scanned in 27 (+1 overlapping) channels for UGC 2259, NGC 6946 and the blue side of NGC 5055 (see section 4.7), giving a sampling of 0.21 Å (9.6 km s^{-1}) per channel. For the rest of the sample, the objects were scanned in 24 channels, for a sampling of 0.24 Å (10.8 km s^{-1}) that is still sufficient, and more efficient, considering the true finesse of the system and readout noise of the CCD.

Due to the use of an aging filter, NGC 2841 and 5055 had to be re-observed. The details are given in the relevant sections.

Following normal de–biasing and flat–fielding with standard IRAF procedures, a robust 3-D cosmic–ray removal routine, that tracks cosmic rays by spatial (pixel–to–pixel) and spectral (frame–to–frame) analysis, was applied to every data cube. When necessary, ghost reflections were then removed using the technique described in Paper I. A neon line (λ6598.95 Å) was always used to fix the zero point at each pixel.

In order to get sufficient signal–to–noise throughout the images, two different Gaussian smoothings were performed on the cubes ($\sigma = 2$ and 3). Three velocity maps (one for each smoothed cube and for the original) were then obtained from the intensity weighted means of the Hα peaks in each pixel. A final variable resolution velocity map was constructed keeping higher resolution where the signal-to-noise makes it possible. Figs. 28 and 30 show the monochromatic images of the galaxies while Figs. 29 and 31 display their velocity fields. All the velocity maps are available at www.astro.umontreal.ca/~blaisous/vf.html. Table XI lists the complete observing parameters. The rest of the analysis was specific to each object.

To the present date, no convention on the way to represent the errors on rotation curves exists in the literature. Error bars are often simply given as the velocity dispersion in the ring used at each radius. However, the hot gas tends to be found in more disturbed environments than the cold gas. Turbulence, local density variations (like spiral arms) and

Table XI: Parameters of the Fabry–Perot observations.

Date of observations	September 97, March 98
Telescope	3.6 m CFHT
Instrumentation:	
Instrument	MOSFP
CCD detector (STIS2)	2048×2048, $\sigma = 8\,e^{-1}$
Filters:	
UGC 2259:	$\lambda_0 = 6575$ Å, $\Delta\lambda = 13$ Å
NGC 2403:	$\lambda_0 = 6568$ Å, $\Delta\lambda = 12$ Å
NGC 6946:	$\lambda_0 = 6566$ Å, $\Delta\lambda = 12$ Å
NGC 5055 blue:	$\lambda_0 = 6575$ Å, $\Delta\lambda = 13$ Å
red:	$\lambda_0 = 6586$ Å, $\Delta\lambda = 12$ Å
NGC 2841:	$\lambda_0 = 6577$ Å, $\Delta\lambda = 10$ Å
NGC 5985:	$\lambda_0 = 6621$ Å, $\Delta\lambda = 26$ Å
Fabry–Perot unit	Scanning QW1162 (CFHT1)
Calibration lamp	Neon ($\lambda = 6598.95$ Å)
Interference order	1155 @ λ_{NEON}
Mean Finesse in th field	12
Duration:	
UGC 2259:	8 min/channel, total of 3.6 h
NGC 2403:	7.34 min/channel, total of 2.9 h
NGC 6946:	7.5 min/channel, total of 3.4 h
NGC 5055 blue:	9.42 min/channel, total of 3.8 h
red:	6 min /channel, total of 2.7 h
NGC 2841:	5 min/channel, total of 2 h
NGC 5985:	7.7 min/channel, total of 3.1 h
Spatial Parameters	
Field size	$8.5' \times 8.5'$
Pixel scale	$0.44''$ pix^{-1}
Spectral parameters	
Free spectral range	5.66 Å (258 km s^{-1})
NGC 2403, 5055, 5985:	
Number of channels	24
Sampling	0.24 Å (10.8 km s^{-1})/channel
UGC 2259 and NGC 6946:	
Number of channels	27
Sampling	0.21 Å (9.6 km s^{-1})/channel
NGC 2841:	
Free spectral range	8.30 Å (378 km s^{-1})
Number of channels	24
Sampling	.35 Å (15.8 km s^{-1})/channel

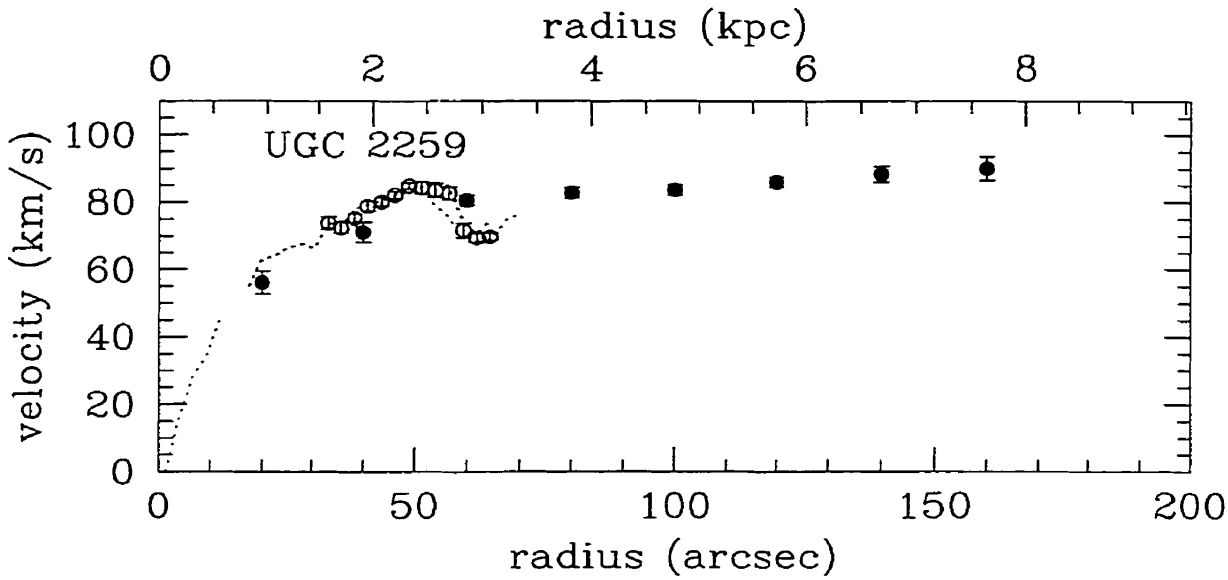

Figure 27: Hα rotation curve of UGC 2259 (open circles) Approaching and receding sides from Hα data are indicated respectively by the dashed and continuous lines. The filled circles represent the HI rotation curve from Carignan et al. (1988).

winds from stars and super-novae of the young stellar forming regions in which the gas is ionized, increase its dispersion. This can lead to the paradox where the fewer points you have (as in long–slit observations) the lower is your dispersion and the smaller are your error bars. As a more direct probe of the uncertainties on the mesured potential, the difference between the two sides of the galaxy is instead sometimes used. Some authors add the error due to uncertainties on inclination and/or position angles.

Since the purpose of this study is to present the data in an unbiased way, the sources of errors are given separately. The error bar itself gives the error on the mean in each ring ($\sigma/\sqrt{N}$) while the solutions for each side of the galaxy are represented by dotted lines (red for the receding side and blue for the approaching). Errors due to inclination uncertainties (often the main contribution to the total error) and to other parameters (Table X) require some assumptions and are not computed here.

4.4 UGC 2259

This small galaxy was observed in September 97 by a fairly photometric night. Eight minutes integration were spent for each channel position and no photometric corrections were needed.

Like in the case of IC 2574 (paper II), dispersion minimizing methods as in ROCUR (Begeman, 1987; Côté et al., 1991) are hardly applicable to determine the rotation curve because of the incomplete coverage of the velocity field. The rotation curve was thus found by comparison of the two sides of the galaxy and analysis of the residual velocity field using the ADHOC package[b]. The inclination, position angle and systemic velocity were fixed at 41°, 158° and 581 $\mathrm{km\,s^{-1}}$, in fairly good agreement with Carignan et al. (1988). The Hα coverage of the field is patchy and mainly concentrated in the center and in the two spiral arms. The net effect is to have only the receding side covering the innermost part of the rotation curve. However, because the two sides cover the outer parts and agree fairly well, this lack of coverage should only affect the determination of the kinematical center. The resulting optical rotation curve at 2.6″ resolution is given in Table XIX while Fig. 27 presents it in combination with the HI rotation curve.

As one can observe, the Hα rotation curve gives access to the very inner kinematics of the galaxy. The solid body rise can now be observed within a few hundreds of parsecs. The Hα curve is higher than the HI by 5 to 10 $\mathrm{km\,s^{-1}}$ up to a radius of 50″, an indication of the presence of beam smearing in the uncorrected HI observations.

The most prominent feature of the Hα rotation curve is the big dip around 60″. This is not observed in the HI curve. It can be seen in the velocity field that the location of this feature corresponds to the two great spiral arms. Spiral arms are known to create such effect, especially on the ionized gas (e.g. Thornley & Mundy, 1997).

Fabry-Perot observations of UGC 2259 by Gonzalez-Serrano & Valentijn (1991) give very similar results but with a somewhat larger dispersion in the rotation velocities. This could be due to the use of only the brightest HII regions, which should have a higher velocity dispersion than the diffuse ionized medium.

4.5 NGC 2403

The object being larger than the available field, two data cubes were acquired during the run of March 98. The same parameters were used for both fields and 440 seconds were spent on each of the 24 channels of each data cube. After the standard data reduction, the final maps (velocity, continuum and monochromatic) were joined using stars in the overlaping region. The coverage of the field was this time complete enough to use ROCUR with bins of 20 arcsec. However, since no significant variations of inclination or position angle were

[b]http://www-obs.cnrs-mrs.fr/adhoc/adhoc.html

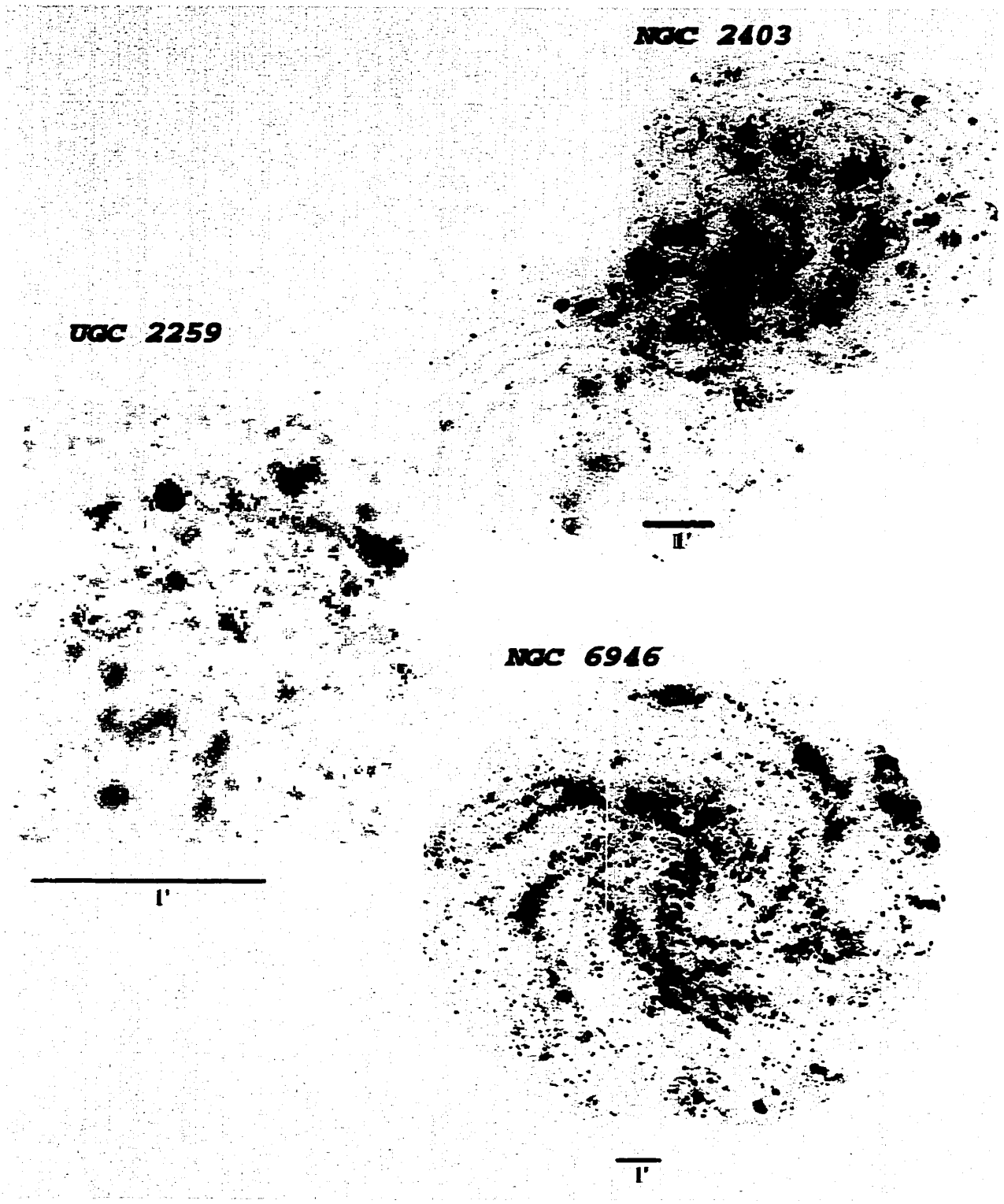

Figure 28: Monochromatic images of the Hα flux of UGC 225·9, NGC 2403 and NGC 6946. Noth is up, East is left.

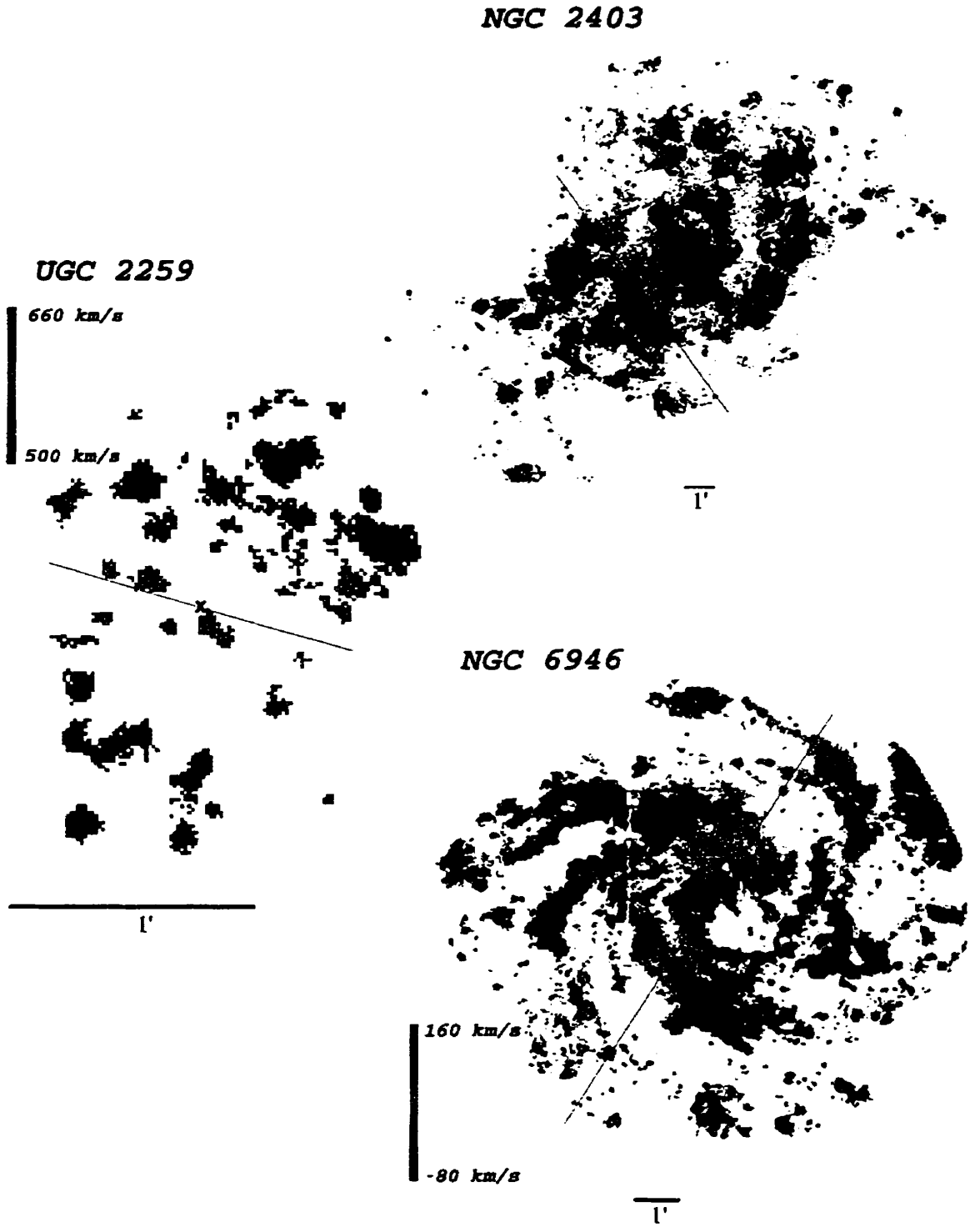

Figure 29: Velocity fields of the same galaxies.The X and the grey line indicate the kinematic center and the axis of separation between the approaching and receding sides.

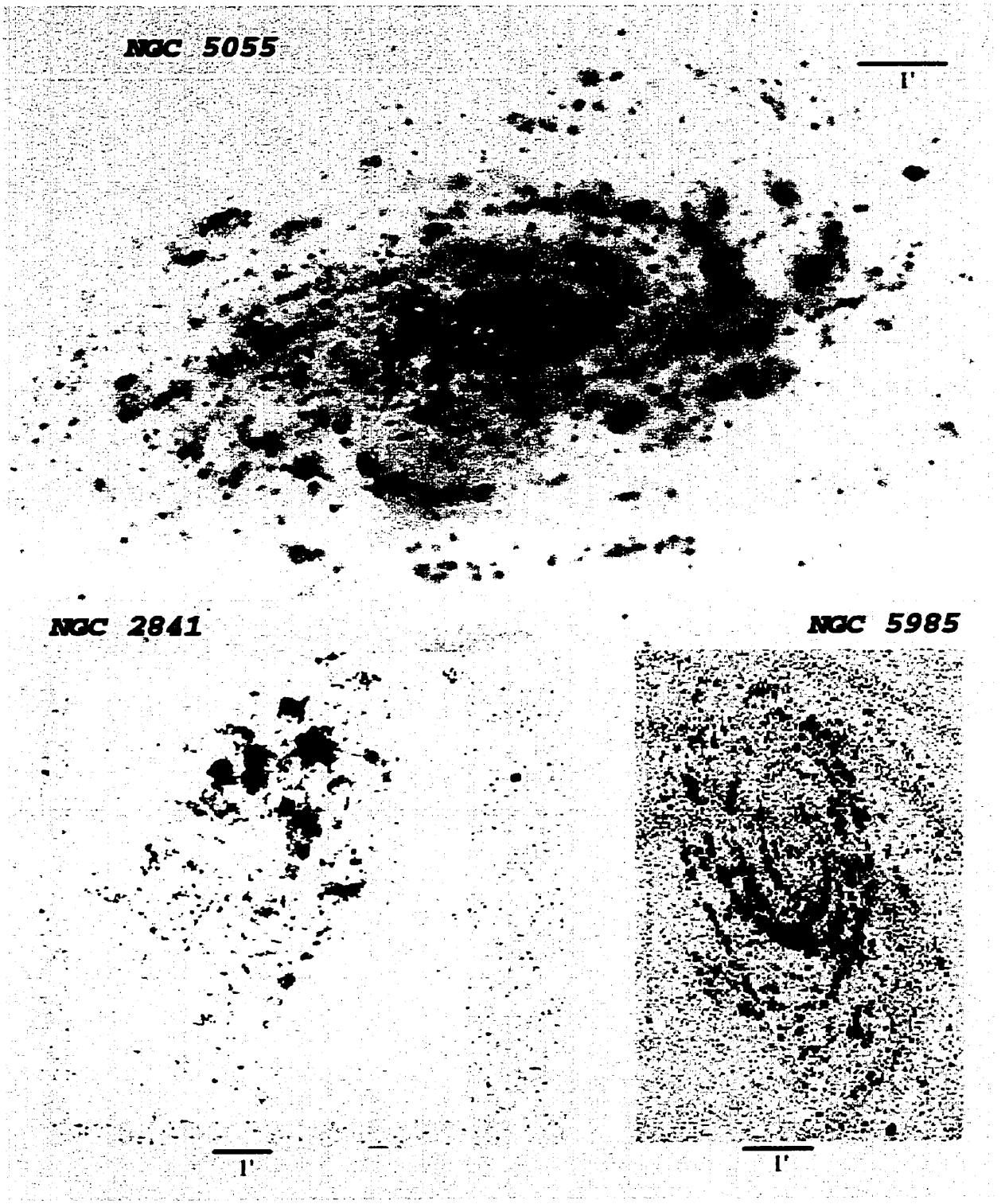

Figure 30: Monochromatic images of the Hα flux of NGC 5055, NGC 2841 and NGC 5985

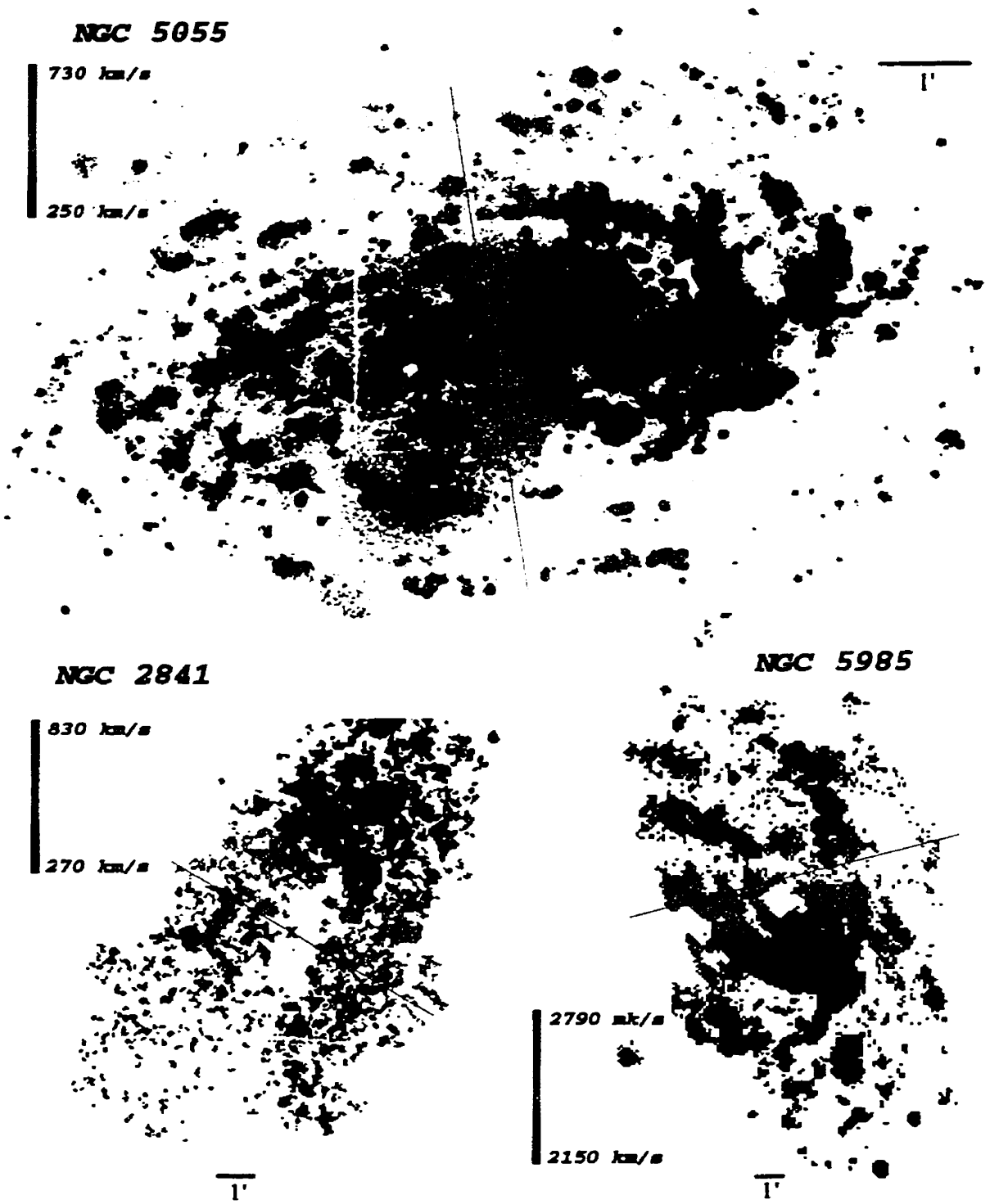

Figure 31: Velocity fields of the same galaxies. The reddest part of NGC 2841 is based on [NII] (λ6548) (*see text*).

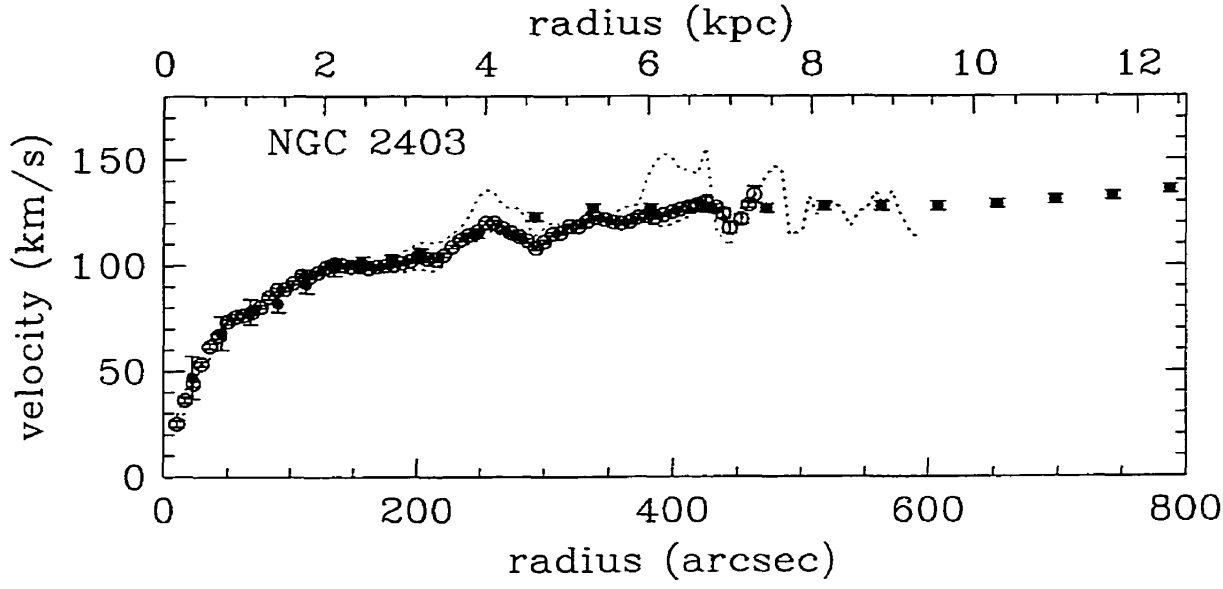

Figure 32: Rotation curves of UGC 2403.

found, ADHOC was used to get a higher precision. The inclination is found to be 61°, the position angle 126°and the systemic velocity 137 $\mathrm{km\,s^{-1}}$, at 3 $\mathrm{km\,s^{-1}}$ of Begeman's value. The shape of the rotation curve is independent of the resolution used and bins of 5 pixels (6.6 ″) offer the clearest picture. Fig. 32 shows the final rotation curve as well as both sides independently. The HI curve is also plotted for comparison.

The Fabry–Perot data give a remarkable agreement between the approaching and receding sides up to 200″. At a greater radius, the number of points on the receding side drops sharply (see Table XX) and the curve then relies mainly on the approaching side. Despite the beam smearing corrections applied to the HI data, optical velocities are still larger ($\sim$ 5 $\mathrm{km\,s^{-1}}$) than the HI velocities between 90″ and 160″. This is well inside the error bars and could be due to residual beam smearing or simply to intrinsic kinematical differences between atomic and ionized gas.

The inner limit of the big external arm is located around 200″ and the effect of the arm can clearly be seen on both sides of the rotation curve. The full resolution velocity map gives an even clearer picture as it shows the effect of the arm at different galactic longitudes. The south–eastern arm is less obvious on the monochromatic image and seems dominated by a few giant HII regions. This explains the bumpy appearance of the receding curve above 200″ where each HII region produces a bump and increase the dispersion. Only the approaching side is seen above 470″ and relies only on a few HII regions.

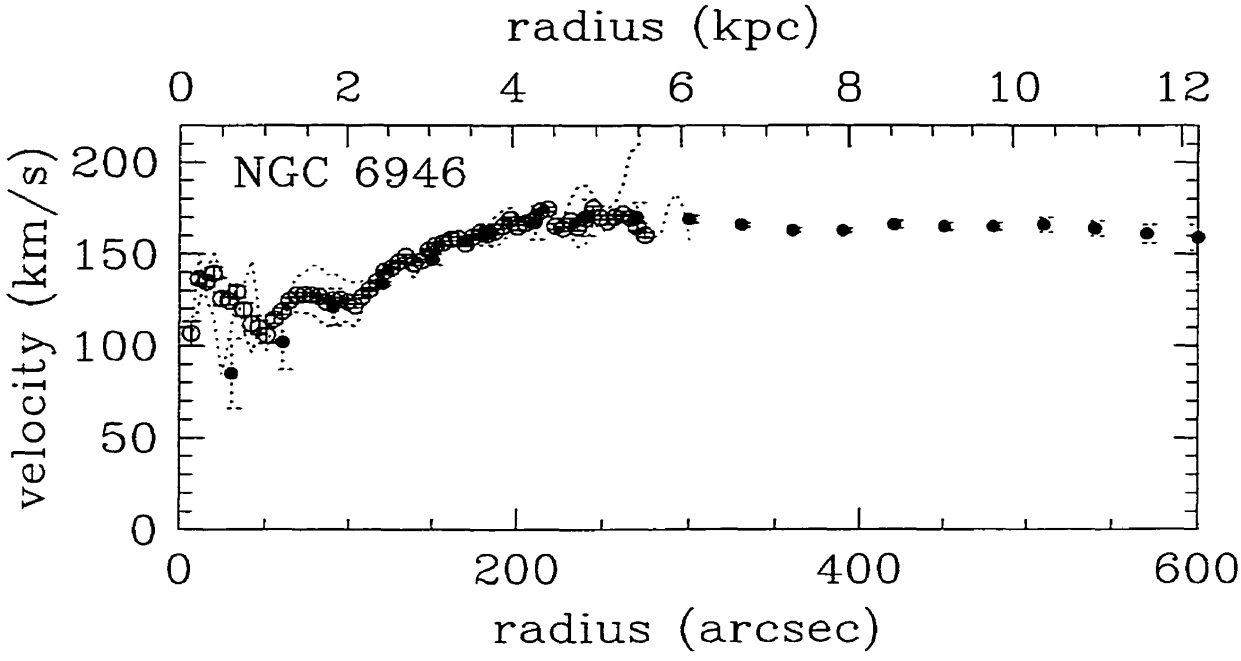

Figure 33: rotation curve of NGC 6946

4.6 NGC 6946

The central part of this bright Scd galaxy suffers from a lack of Hα emission. Despite the 3.5 hours of observation that otherwise gave the sensitivity to reach down to the smaller HII region and the diffuse Hα , few Hα photons were collected up to 50″ in radius. The velocity dispersion is high in that region and makes the true kinematics hard to retrieve. This appears clearly in the rotation curve presented in Fig. 33 and in Table XXI. The high velocities in the inner part of the Hα rotation curve could be caused by gas movement along a central bar (Bonnarel et al., 1988). They could also be purely rotational considering the large amount of molecular hydrogen in the inner parts (Young & Scoville, 1982).

Between 70″ and 100″, the rotation curves on both side are smoother but present a big asymmetry, indicative of non circular motions. The rest of the rotation curve (resolution of 4.4″) matches the HI curve. The systemic velocity is found to be 47 $\mathrm{km\,s^{-1}}$ in agreement with Carignan et al. (1990) but not consistent with the 38 $\mathrm{km\,s^{-1}}$ found by Bonnarel et al. (1988). However, the inclination and position angles are less constrained due to the uncertainties caused by the global asymmetry. They are compatible with both Bonnarel (I = 32°and PA = 58°) and Carignan et al. (I = 38°and PA = 60°). They were fixed to the latter for ease of comparison. It has to be noted that the uncertainty on the inclination can affect dramatically

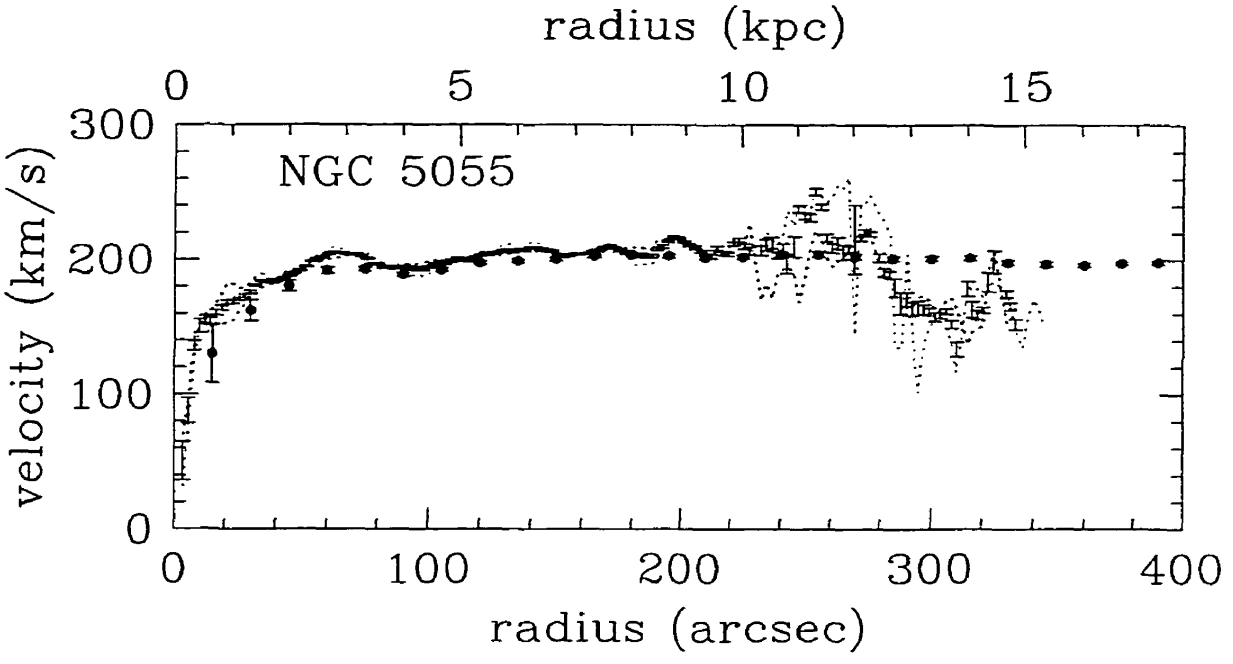

Figure 34: Rotation curves of NGC 5055.

(as $\sin i$) the velocities. For example, Sofue (1996) uses an optically determined inclination of 30°for his CO data along the major axis and ends up with velocities 20% higher. It seems therefore very important to have a complete 2-D coverage to allow an independent determination of optical parameters.

4.7 NGC 5055

This object has first been observed in March 98 but the interference filter used had apparently blueshifted from its quoted central wavelength, probably due to ageing effect. The flux from the receding half of the galaxy was therefore almost totally blocked. To complete the data set, it has been observed again in April 99 using a redder filter. Both sets of data were analyzed following the standard procedure and two variable resolution velocity fields were produced. They have then been combined using the field stars.

Whether inclination and position angles were kept fixed at the value derived by Thornley & Mundy (1997) or let free to vary (in wich case the averages are 64° and 99°), the Hα rotation curve (Fig. 34 and XXII) ranges systematically from 2 to 11 $\mathrm{km\,s^{-1}}$ above the HI curve. This fact is hard to understand especially in regards of the otherwise general good agreement between the two curves. Pismis et al. (1995) published a long-slit based rotation

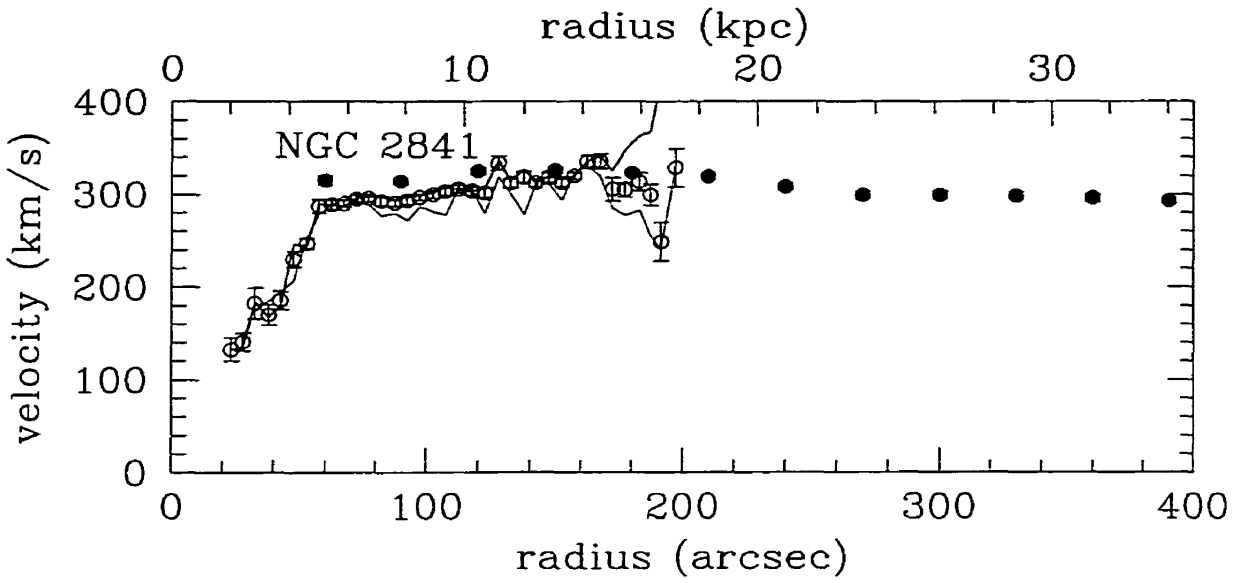

Figure 35: Rotation curves of NGC 2841.

curve that tends to be sligthly lower than the present Fabry-Perot curve. However, because of its optically fixed position angle (99°) and its limit in radius (70″), it is hard to rely on it to solve the discrepancy.

If one normalizes the HI and Fabry-Perot Hα curves to their flat part, two important differences still exist between them. First, the central Hα points are still higher than their HI conterparts. This can be once more naturally associated with beam smearing in the 21 cm observations. Second, it can be noticed that the amplitude of the velocity variations due to the passage of the spiral arms, are much more pronounced in the Hα data than in HI . This is again an illustration of the sensitivity of the ionized gas to its environment. The effects of the arms of this Sc galaxy on the kinematics have been also observed and extensively studied by Thornley & Mundy (1997).

4.8 NGC 2841

First observed at CFHT with the same blueshifted filter than NGC 5055, this galaxy was reobserved in March 2000 at the Observatoire de Haute-Provence (France) in the context of the GHASP survey.

The GHASP instrumentation is basically the same that the MOSFP used elsewhere in this paper whereas a photon counting camera is used instead of a CCD. Because photon

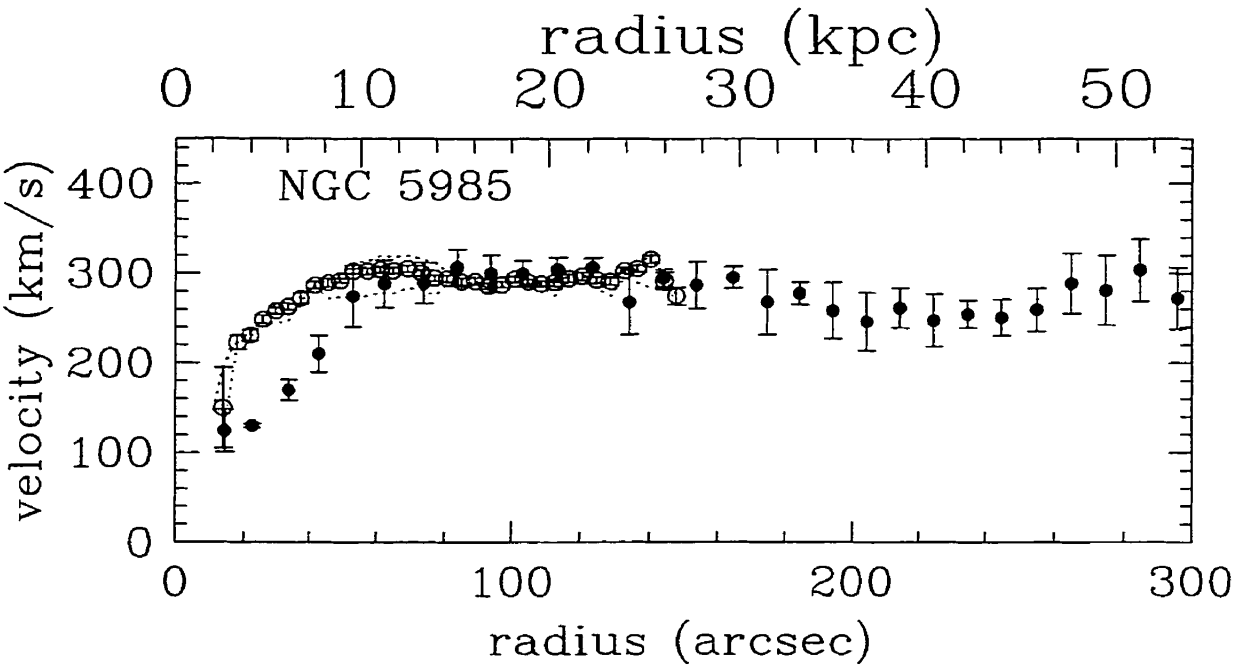

Figure 36: Hα Rotation curves of NGC 5985.

counting cameras have intrinsically no read-out noise, it is possible to rapidly scan through the 24 channels several times, averaging photometric variations of the sky. It is then easy to remove night sky emission lines and background light (Amram et al., 1995). An almost complete velocity field was retrieved using the weighted mean of the Hα peak in each pixel although the available filter was not perfectly matched to the galaxy. The rotation curve was found using fixed values of the inclinaison and position angle, giving the galaxy an inclination of 66°, a position angle of 150° and a systemic velocity of 633, identical to the values found by Begeman inside a radius of 180″. The kinematical center was found to be centered on the bright nucleus. The final Hα curve (Tab. 35 and Tab. XXIII) is based on a gaussian smoothed ($\sigma = 3''$) version of the velocity field.

Despite the very similar parameters, the Hα velocities stay up to 26 km s^{-1} below the beam smearing corrected HI in the inner part of the galaxy. Due to the low radio resolution (>32″) and the steepness of the rotation curve, it is conceivable that the first HI points have been over-corrected for beam smearing. This points out to the large uncertainties associated to software corrections of 21 cm data.

4.9 NGC 5985

This massive galaxy was observed with a wider filter (26Å) but centered 3Å bluer than the galaxy central wavelength. That, in conjunction with the high rotational velocity, prevented the reddest flux to reach the CCD. The velocity field is thus slightly incomplete on the receding side but a complete and reliable rotation curve can be derived.

This galaxy has not yet been the object of a detailed kinematical study. The HI velocity field comes from the WHISP project (Westerbork HI survey of SPiral galaxies) (Swaters, private communication). The Hα (Tab. XXIV) and HI (Tab. XXV) rotation curves were computed in the same manner with, respectively, 4″ and 10″ bins. They are shown superimposed in Fig. 36. It is clear that the uncorrected HI observations suffer from large systematic uncertainties, only part of it beeing beam smearing. The difference of more than 100 $\mathrm{km\,s^{-1}}$ is not surprising for an early–type spiral galaxy that lacks HI in its center and rises to its maximum velocity inside 65″, only twice the radio beam width (30″).

4.10 Discussion and Summary

It is clear from the available data that uncorrected HI observations are commonly affected by beam smearing. A useful test to estimate the reliability of HI observations is to compare the size of the radio beam width to the size of the galaxy. Bosma (1978) introduced the ratio $R_B \equiv R_H/\mathrm{S}$ where R_H is the Holmberg radius and S is the radio beam major axis width. A more surface brightness independent ratio was introduced by van den Bosch et al. (2000): $R_{vdB} \equiv \alpha^{-1}/\mathrm{S}$ where α^{-1} is the B–band stellar disk scale length. Table XII compares the two ratios to the maximum difference between Hα and HI curve in the rising part of the galaxies.

Despite the limited size of the sample, it is clear that even in the cases where the HI data sample well the rotation curve, strong beam smearing can still be found. As expected, the effect also increases with the slope of the inner rotation curves. Correcting the HI rotation curve for beam smearing is possible, but the reliability remains uncertain as illustrated by NGC 2841.

Amid the uncertainties that can affect rotation curves, non-circular motions like bars and local phenomena such as expanding bubbles or spiral arms can be efficiently tracked by the 2-D spectroscopic coverage from Fabry-Perot data. Following their orientation, bars can change the radial velocities in the inner parts of galaxies. Their signature may however be

Table XII: Beam–to–galaxy size and beam smearing importance. R_B is the ratio between the Holmberg radius and the beam width while R_{vdB} is the scale length over the beam width. ΔV_{max} is the maximum velocity difference between the Hα and HI data in the rising part of the rotation curve.

Galaxy name	Beam width $''$	R_B	R_{vdB}	ΔV_{max} km s^{-1}
UGC 2259	13.2	5.2	1.29	8
NGC 2403[a]	26	26	4.62	7
NGC 6946	24.5	19	4.70	17
NGC 5055	12.8	46	8.51	24
NGC 2841[a]	25	15	2.08	-9
NGC 5985	30	5.3	1	101

[a]HI corrected for beam smearing

seen in the velocity field as a regular deviation from the typical projected circular velocities. None of our SB or SAB shows signs of these deviations but some of them have very low signal to noise in the center (UGC 2259 and NGC 5985) or very high dispersion (NGC 6946).

Complete 2-D velocity fields also allow independent determinations of inclination and position angles, kinematical centers and systemic velocities. This is a major gain considering the sensitivity of the rotation curves to these parameters.

Beam smearing can have major repercussions on many conclusions drawn using HI data only. It often dramatically changes the relative importance of luminous and dark matter in a given galaxy, as shown in paper I and II. Also, as already pointed out by Swaters (1999) and by van den Bosch et al. (2000), it raises some questions about the strong claims made using HI observations of low surface brightness galaxies (McGaugh & de Blok, 1998; Kravtsov et al., 1998).

4.11 Conclusions

This study provides high accuracy Hα rotation curves for six spiral galaxies ranging from Scd to Sb. It leads to the following conclusions.

- HI observations are subject to important beam smearing even for beam width smaller than a eighth of the scale length.

- Because computed circular velocities strongly depend on the optical parameters (inclination, position angles and kinematic center), independent determinations of these parameters via complete 2-D velocity fields are necessary.

- Software corrections of beam smearing in HI observations can improve their accuracy but remain quite uncertain.

We are indebted to Stéphanie Côté for the opportunity to re-observe NGC 5055. We also warmly thank Jacques Boulesteix for his software and for fruitful discussions on Fabry-Perot data reduction. We would like to thank the staff of the CFHT for their support during the FP data acquisition and Steeve Godbout who helped with the data acquisition. CC acknowledges grants from NSERC (Canada) and FCAR (Québec).

References

Aaronson, M. & Mould, J. 1983, ApJ, 265, 1

Amram, P., Boulesteix, J., Marcelin, M., Balkowski, C., Cayatte, V., & Sullivan, W. 1995, A&AS, 113, 35

Begeman, K. 1987, PhD thesis, Rijksuniversiteit Groningen

Blais-Ouellette, S., Carignan, C., Amram, P., & Côté, S. 1999, AJ, 118, 2123

—. 2000, AJ, submitted to AJ

Bonnarel, F., Boulesteix, J., Georgelin, Y. P., Lecoarer, E., Marcelin, M., Bacon, R., & Monnet, G. 1988, A&A, 189, 59

Bosma, A. 1978, PhD thesis, Rijksuniversiteit Groningen

Bullock, J., Kolatt, T., Sigad, Y., Somerville, R., Kravtsov, A., Klypin, A., J.R., P., & Dekel, A. 1999, astro-ph/9908159

Burkert, A. & Silk, J. 1999, in Dark matter in astro and particle physics, ed. H. Klapdor-Kleingrothaus

Carignan, C., Charbonneau, P., Boulanger, F., & Viallefond, F. 1990, A&A, 234, 43

Carignan, C., Sancisi, R., & Van Albada, T. S. 1988, AJ, 95, 37

Côté, S., Carignan, C., & Sancisi, R. 1991, AJ, 102, 904

Dalcanton, J. J. & Hogan, C. J. 2000, astro-ph/0004381

Freedman, W. L. 1990, ApJ, 355, L35

Gonzalez-Serrano, J. & Valentijn, E. 1991, A&A, 334

Kravtsov, A. V., Klypin, A. A., Bullock, J. S., & Primack, J. R. 1998, ApJ, 502, 48

McGaugh, S. S. & de Blok, W. J. G. 1998, ApJ, 499, 66

Milgrom, M. 1983, ApJ, 270, 365

More, B., Governato, F., Quinn, T., Stadel, J., & Lake, G. 1998, ApJ, 499, L5

Navarro, J. F., Eke, V. R., & Frenk, C. S. 1996a, MNRAS, 283, L72

Navarro, J. F., Frenk, C. S., & White, S. D. M. 1996b, ApJ, 462, 563

—. 1997, ApJ, 490, 493

Pismis, P., Mampaso, A., Manteiga, M., Recillas, E., & Cruz Gonzalez, G. 1995, AJ, 109, 140

Sharina, M. E., Karachentsev, I. D., & Tikhonov, N. A. 1997, Pis ma Astronomicheskii Zhurnal, 23, 430

Sofue, Y. 1996, ApJ, 458, 120

Sofue, Y., Tutui, Y., Honma, M., Tomita, A., Takamiya, T., Koda, J., & Takeda, Y. 1999, ApJ, 523, 136

Spergel, D. & Steinhardt, P. 1999, astro-ph/9909386

Swaters, R. 1999, PhD thesis, Rijksuniversiteit Groningen

Thornley, M. D. & Mundy, L. G. 1997, ApJ, 484, 202

van den Bosch, F. C., Robertson, B. E., Dalcanton, J. J., & de Blok, W. J. G. 2000, AJ, 119, 1579

Young, J. S. & Scoville, N. 1982, ApJ, 258, 467

Chapitre 5

MOND et les halos sombres à l'épreuve

ACCURATE DETERMINATION OF THE MASS DISTRIBUTION IN SPIRAL GALAXIES.

IV. Multi-wavelength Rotation Curves to Test Dark Halos Profiles and Modified Dynamics

SÉBASTIEN BLAIS-OUELLETTE

Département de physique and Observatoire du mont Mégantic, Université de Montréal, C.P. 6128, Succ. centre ville, Montréal, Québec, Canada. H3C 3J7 and
Observatoire de Marseille, 2 Place Le Verrier, F–13248 Marseille Cedex 04, France

e–mail: blaisous@llnl.gov

CLAUDE CARIGNAN

Département de physique and Observatoire du mont Mégantic, Université de Montréal, C.P. 6128, Succ. centre ville, Montréal, Québec, Canada. H3C 3J7

e–mail: carignan@astro.umontreal.ca

PHILIPPE AMRAM

Observatoire de Marseille, 2 Place Le Verrier, F–13248 Marseille Cedex 04, France

e–mail: amram@observatoire.cnrs-mrs.fr

To be submitted to Astronomical Journal

A sample of 10 rotation curves of spiral galaxies observed in both Fabry-Perot spectroscopy and aperture synthesis radio observations is used to investigate the mass distribution of luminous and dark matter. The individual mass models are presented using 4 different parametrizations. It is shown that galaxies with a maximal rotation velocity $V_{max} \lesssim 90$ km s^{-1} have a dark halo with an inner density slope $\gamma \lesssim 0.6$. Also, a strong correlation with moderate scatter is found between the characteristic density and radius, the two free parameters of halo functional forms. The sample is also modeled with the MOND prescription which gives good fits for 8 galaxies but fails to reproduce the rotation curve of UGC 2259 and NGC 3109. Nonetheless, the "universal constant" a_0 needs to be systematically higher for lower surface brightness galaxies which is in contradiction with MOND as a universal law.

5.1 Introduction

Spiral galaxies are known to present an important mass discrepancy between their dynamical and visible masses. The commonly accepted hypothesis is to assume a more or less spherical halo of unseen matter in addition to the stars and gas. Improved observational capabilities combined with an increase of the numerical simulations' accuracy have made the exact density distribution of these halos an important and much debated issue. On one side, N-body simulations of the cosmological evolution of the Cold Dark Matter (CDM) have now reached a sufficient resolution so that they can predict the dark halos density profiles down to the innermost parts of spiral galaxies. They almost always show dense cuspy halos (Navarro et al., 1996b, 1997; Fukushige & Makino, 1997; More et al., 1998) although a few others give a shallower profile (e.g. Kravtsov et al., 1998). On the other side, observations of dwarf and late type spiral galaxies present a shallow inner rotation curve, compatible with a flat density core. In order to resolve this discrepancy, a plethora of scenarios have been suggested. One can invoke, among other possibilities, a second dark component (Burkert & Silk, 1997) or some feedback process that relaxes the halo concentration in the center (Puche et al., 1992; Navarro et al., 1996a). Self-interacting (Spergel & Steinhardt, 1999) or annihilating (Kaplinghat et al., 2000) dark matter also possibly lead to much shallower inner density profiles.

Many of these hypothesis predict some relation between the dark halo profiles and observables in the galaxies. For example, a feedback process can only take place efficiently in relatively shallow potential well so that the cuspiness of the density profile should increase with galaxy mass (van den Bosch et al., 2000). Similarly, self-interacting dark matter leads to an inverse dependency of the core radius on the mass of the galaxy (Dalcanton & Hogan, 2000).

On the other hand, an alternative explanation of the mass discrepancy have been the object of much attention lately. The MOdified Newtonian Dynamics (MOND, Milgrom, 1983b) have been used, among other things, to explain the shallow rotation curve of the low surface brightness galaxies (McGaugh & De Blok, 1998). Because LSB galaxies can have important masses, these rotation curves, if accurate, could indeed put the standard CDM evolution scenario in some trouble.

Rotation curves of spiral galaxies offer a powerful tool for probing the density profiles of dark halos. However, few galaxies had their kinematics studied with both a sufficient sensitivity to probe the gravitational potential beyond the optical disk and a high enough

spatial resolution to accurately determine the inner, rising part of their rotation curve. As shown in Blais-Ouellette et al. (1999, 2000a), both are crucial to constraint the halo mass distribution. Only a complete, well sampled rotation curve can rule out a particular halo model (Burkert & Silk, 1997; Swaters, 1999; van den Bosch et al., 2000). As pointed out by Persic et al. (1996), increasing the spatial resolution is also necessary to establish reliable correlations between the properties of dark and visible matter.

This study is the forth of a series on spiral galaxies rotation curves and mass models using multi-wavelength rotation curves. A reasonable sample of spiral galaxies observed in both Hα and HI is now available from the previous papers (Blais-Ouellette et al., 1999, 2000a,b, hereafter paper I, II and III). For NGC 5585, NGC 3198, NGC 3109 and IC 2574, the rotation curves and mass models are directly taken from papers I and II. The composite rotation curves and brightness profiles for the objects studied in paper III are explained in section 5.2. Best–fit mass models are then used in section 5.3 to determine which parameterizations of dark halos are consistent with the observations and to what extent they are compatible with the steep central cusp of the N-body simulations. Mass models using MOND are also investigated in the second part of section 5.3. Then systematics in the halo profiles as well as relations between the visible part of the galaxies and the dark mass distribution are explored in section 5.4.

5.2 MULTI-WAVELENGTH ROTATION CURVES

The problem of "beam smearing" in radio observations is well known but its consequences on rotation curves and mass modeling have often been underestimated. While it is commonly thought that a beam–width/scale–length ratio of 1 or 2 was sufficient to get a reliable rotation curve (Bosma, 1978; Persic et al., 1996), paper III showed that galaxies with ratios as high as 8 can still show significant beam smearing.

The use of high resolution Fabry-Perot spectroscopy gives the opportunity not only to increase the resolution but also to have the same full 2-D coverage than with radio aperture synthesis observations. This helps to avoid errors on the inclination and position angles to which spectroscopy along the major axis (long–slit or submillimiter) are more sensitive. Non–circular motions and asymmetries in the rotational pattern of the galaxies are also much more easily tackled.

Table XIII: Parameters of the sample (including the galaxies from Paper I and II). From the main references unless specified.

Name	Type	Dist.	D_{25}	R_{HO}	$\alpha^{-1}{}^{P4}$	$B(0)_c^{P4}$	M_B	L_B	References		
		Mpc	$'$	$'$	$''$	mag/$''^2$	mag	$10^8 L_\odot$	HI	Hα	phot.
IC 2574**	SABm	3.0	9.8	8.6	151.3	23.4	-16.77	7.9	Ma	P2	Ma
NGC 3109**	SBm	1.4^{Mu}	14.4	13.3	181.3	23.2	-16.35	5.2	Jo	P2	Jo
NGC 5585**	SABd	6.2	5.3	3.6	49.5	21.9	-17.50	14.8	Cot	P1	Cot
UGC 2259	SBcd	9.6*	2.6	1.9	24.1	21.8	-17.03	9.7	C88	P3	C88
NGC 2403	SABcd	3.2^{Fr}	21.9	13.0	137.4	21.8	-19.50	93.6	Be	P3	Ke
NGC 6946	SABcd	6.2^{Sh}	11.5	7.8	114.2	20.3	-20.85	324	C90	P3	C90
NGC 3198**	SBc	9.2^{P1}	8.4	11.9	55.2	21.9	-19.90	139	Be	Cor	Ke
NGC 5055	SAbc	9.2*	12.6	9.8	95	21.1	-21.13	422	Th	P3	Ke
NGC 2841	SAb	18^{Aa}	11.3	6.2	51	20.1	-21.93	880	Be	P3	Mo/Ke
NGC 5985	SABb	37.1*	5.5	2.6^{P4}	29.9^{P4}	21.4	-21.74	738	P3	P3	Ke

^{P1}Paper I
^{P2}Paper II
^{P3}Paper III
^{P4}This study
^{Ma}Martimbeau et al. (1994)
^{Mu}Musella et al. (1997)
^{Jo}Jobin & Carignan (1990)
^{Cot}Côté et al. (1991)
^{C88}Carignan et al. (1988)
^{Fr}Freedman (1990)
^{Be}Begeman (1987)
^{Ke}Kent (1987)
^{C90}Carignan et al. (1990)
^{Cor}Corradi et al. (1991)
ThThornley & Mundy (1997)
^{Aa}Aaronson & Mould (1983)
^{Mo}Moriondo et al. (1998)
^{Sh}Sharina et al. (1997)
Col 4: Diameter at 25 B-mag/arcsec^2
Col 5: Holmberg Radius
Col 6: Scale length
Col 6: Corrected Central Surf. Bright.
Col 7: Absolute B magnitude
Col 8: B Luminosity
*$H_0 = 75\,km\,s^{-1}\,Mpc{-}1$
**Mass models from Paper II

UGC 2259

The crossing of the spiral arms is known to create wiggles in the isovelocity contours and S-shape patterns in rotation curves deduced from the gas kinematics. This effect is especially acute for ionized gas since it is concentrated around the abundant star forming regions that flourish in the spiral arms. However, the complete 2-D velocity field obtained with Fabry-Perot spectroscopy, gives the opportunity to diagnose in details the location and effect of arms and avoid confusion with true gravitational rotation. The neutral gas being more evenly distributed throughout the disk than the ionized gas, the local fluctuations are averaged out and the effect of spiral arms are much less acute.

UGC 2259 has a spiral arm around $55''$ but the Hα coverage stops before the end of the arm and cannot reliably account for the real rotational velocities in this region. In order to diminish the impact of these local perturbations but still correcting for beam smearing, the final rotation curve is composed of the Hα curve up to $46''$ and the HI complete the curve further out.

NGC 2403

As observed in paper III, the big north-western arm begins around 200″. This corresponds to the radius where the two sides of the Hα rotation curve cease to be in good agreement. The limit of the Hα data in the composite curve is thus fixed to 195″. The HI complete the curve for r>200″.

NGC 6946

Because of the strong dispersion in the inner parts of this galaxy, the optical rotation curve is only used from 50″ to 178″. The HI curve is used from 180″. This galaxy contains a small bulge component but given its size and the uncertainties in the center, no attempt to decompose the brightness profile is done.

NGC 5055

In addition to the exponential disk, this Sb galaxy also clearly contains a spheroidal component. Because bulges are likely to have different mass–to–light ratio than disks and because the rotation curve seems reliable down to the very center, it is important to accurately decompose the luminosity profile into its two components via a χ^2 minimization.

An exponential disk:

$$\mu_D(r) = \mu_0 + 1.0857(r/r_0)$$

is used where μ_D is the disk surface brightness, μ_0 and r_0 are characteristic surface brightness and radius. A de Vaucouleurs law, truncated at large radius to avoid any significant contribution of the bulge in the outer part of the galaxy, accounts for the bulge:

$$\mu_B = \mu_e + 8.3268\left[(r/r_e)^{1/4} + (r/r_t)^4\right]$$

where μ_B is the surface brightness of the bulge and μ_e and r_e and r_t are respectively the effective surface brightness and radius and the outer truncation radius.

However, structures and wiggles in the luminosity profile, if they represent variations in luminous mass and not change in $(\mathcal{M}/\mathrm{L}_B)_\star$, can translate into structures in the rotation curve. In order to keep this information, the total luminosity profile is used at large radii where the bulge is negligible. In the inner parts, the fitted exponential disk is subtracted to retrieve the final bulge contribution. The results are shown in Fig. 37 for NGC 5055.

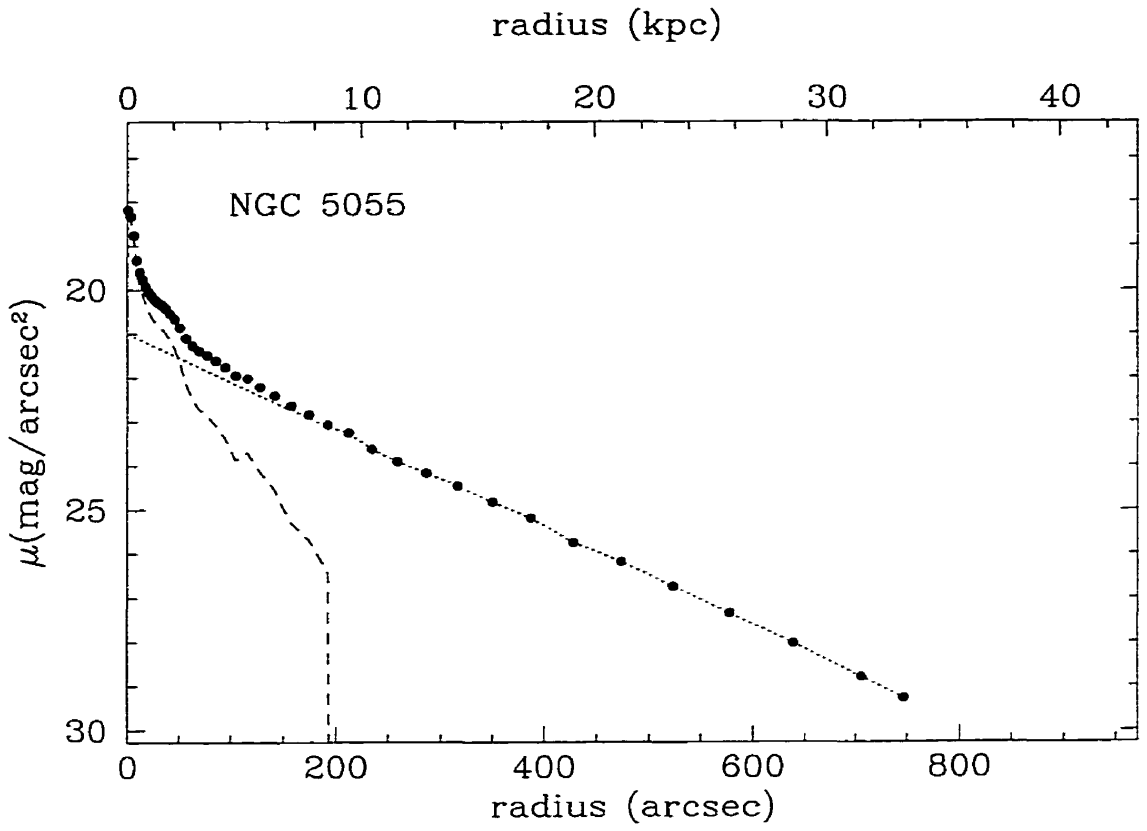

Figure 37: Decomposition of the brightness profile of NGC 5055. The dashed curve represents the final profile of the bulge contribution while the dotted line shows the fit to the disk profile.

Based on Paper III results, the most reliable rotation curve for NGC 5055 must be composed of the Hα curve up to 52″ to avoid the first wiggle and be completed with the HI curve (Thornley & Mundy, 1997) from 75″ outward.

NGC 2841

This Sb galaxy also clearly has a spheroidal stellar bulge component. Like many spiral galaxies, a depression in the luminosity profile marks the transition between the bulge and the disk. This feature is however far less acute when using K–band photometry, less sensitive to internal absorption by dust and more representative of the mass dominant old stellar population.

The luminosity profile used here comes from K–band surface photometry from Moriondo et al. (1998) in the inner part and r–band major axis photometry from Kent

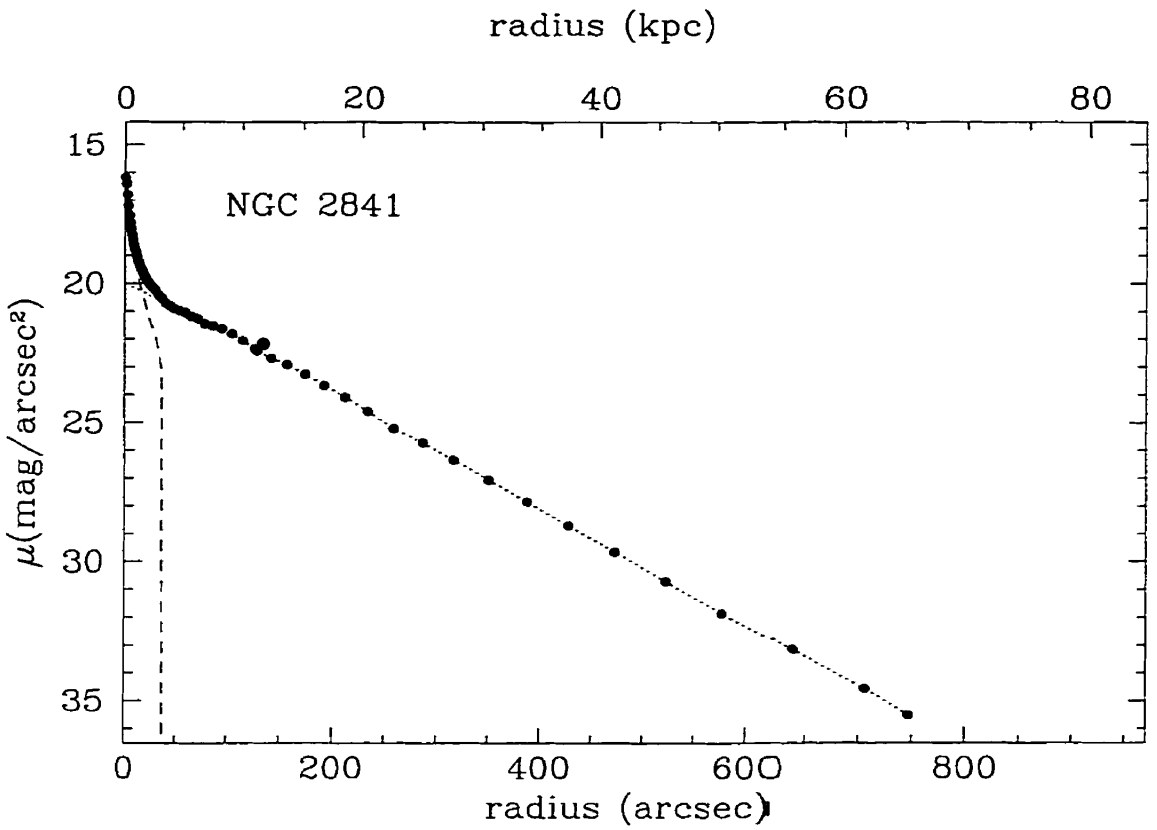

Figure 38: Decomposition of the brightness profile of NGC 2841. The dashed curve represents the final profile of the bulge contribution while the dotted line shows the fit to the disk profile.

(1984) at larger radii. The quoted (r-K)=3 is used in addition of the Kent's B=r+.9 rule of thumb in order to obtain a B–band equivalent luminosity profile. The two profiles match almost perfectly but a slight change in the slope of the exponential disk is seen in the K–band data. For the decomposition, the disk is fitted to its inner part, just before the bulge becomes important. The final contributions are calculated as for NGC 5055. The result is shown in (Fig. 38).

On the kinematics side, the Hα observations rectified the over-corrected HI data up to 160″ and are therefore used up to this point. The HI data complete the rotation curve. Sofue et al. (1999) note a steep decline of the rotational velocities in the inner 45″ in their CO observations. This is not seen in the Hα curve but reliable coverage starts around 25″, leaving some unknown for the innermost part. Taking into account the submilimiter data, a massive punctual central component have been added to the mass models. The maximum allowed central mass, found to be around $5\times10^8\mathcal{M}_\odot$, is fixed in all the NGC 2841 models

to reduce the degrees of freedom.

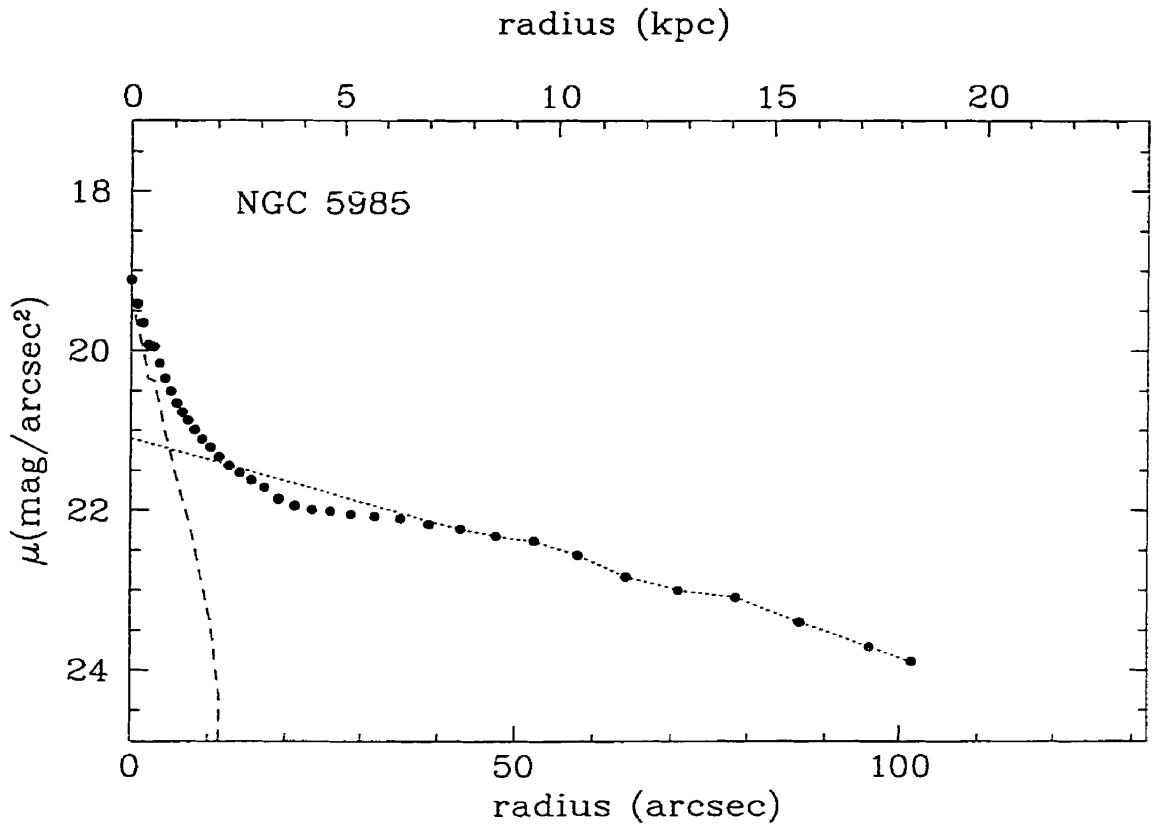

Figure 39: Decomposition of the brightness profile of NGC 5985. The dashed curve represents the final profile of the bulge contribution while the dotted line shows the fit to the disk profile.

NGC 5985

The brightness profile of this galaxy is based on r band major axis photometry from Kent (1984). Once again, an important depression is seen at the transition between the bulge and the disk. As we have seen in the preceding case, this tends to disappear when using near-infrared photometry. It was therefore decided to "correct" that feature, extrapolating the exponential disk down to the center of the galaxy (Fig. 39).

In Paper III it was seen that the optical data brought a strong correction to the low resolution HI observations. Since the Hα data behave very well up to 128″, HI data are just used from 130″.

5.3 Mass models

5.3.1 CDM halos

Mass models of the paper III sample were derived following the method described in paper II and presented in Fig. 40 to 45. Each galaxy is modeled with the pseudo–isothermal sphere, the Burkert profile (Burkert & Silk, 1997), the KKPB profile (Kravtsov et al., 1998) and the NFW profile (Navarro et al., 1996b). In the fitting process, the same weight has been given to the rising and flat parts of the galaxies. The error bars are only given when they exceed the size of the marker ($\sim 8\,\mathrm{km\,s^{-1}}$) and just include the uncertainties related to the dispersion in each bin. See Paper III for a more complete discussion on uncertainties.

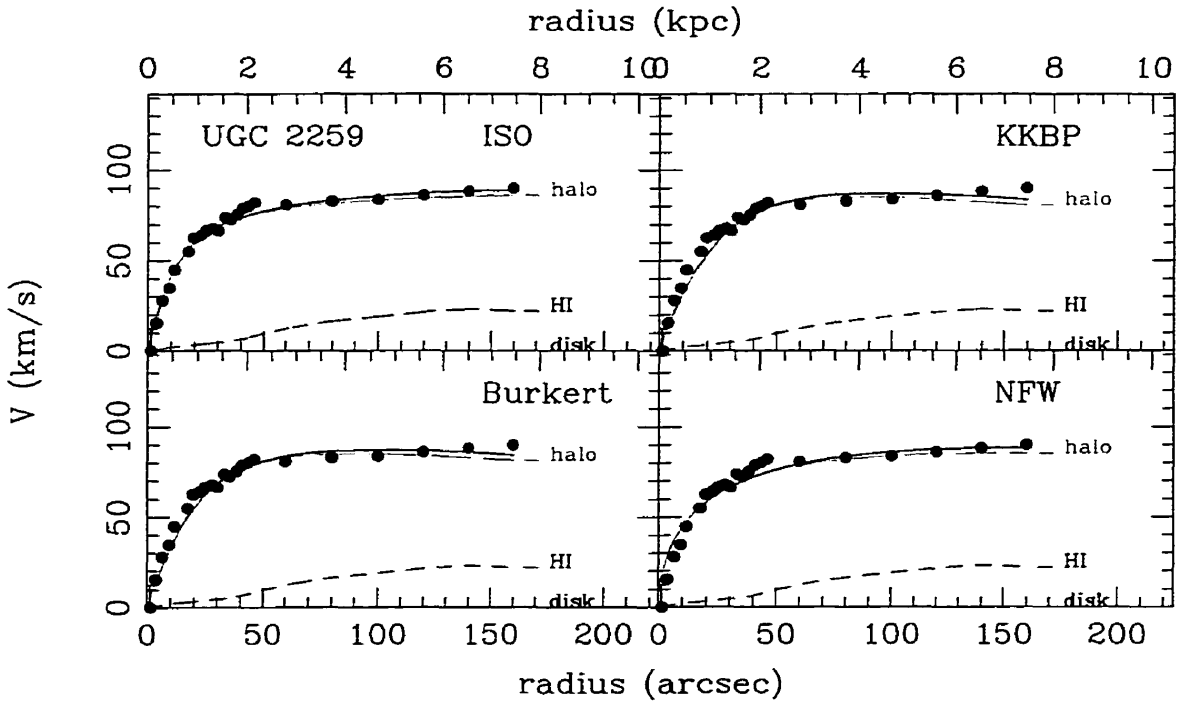

Figure 40: Mass model of UGC 2259. The fit gives a unrealistic value of $(\mathcal{M}/\mathrm{L}_B)_\star = 0$ for the disk.

The three bulgeless galaxies (UGC 2259, NGC 2403, NGC 6946) offer the best constraints on the mass distribution. In particular, the small Sc galaxy UGC 2259 has a rotation curve too shallow to be compatible with NFW model. It also appears to continue rising gently after the turnover, closer to a $\beta = 2$ model (isothermal sphere) than with a higher β as in the Burkert's or KKBP models. However, even with the present high resolution rotation curves, the other, more massive galaxies, offer few constraints on the models. This

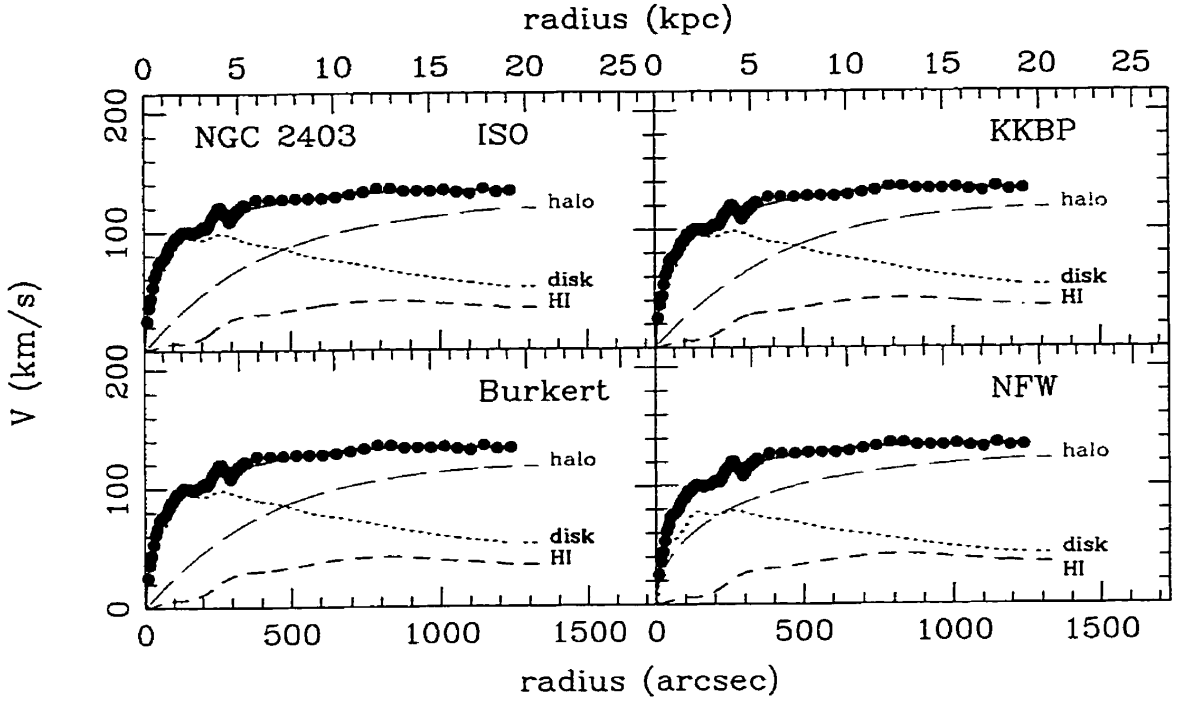

Figure 41: Mass model of NGC 2403

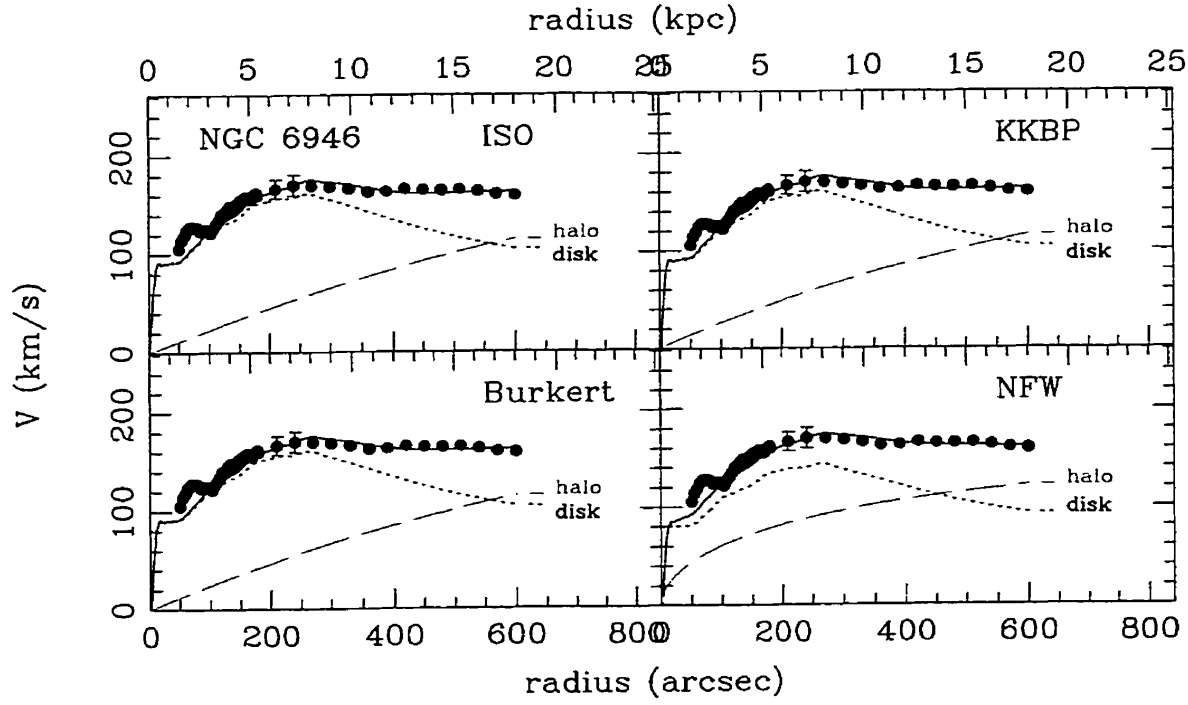

Figure 42: Mass model of NGC 6946

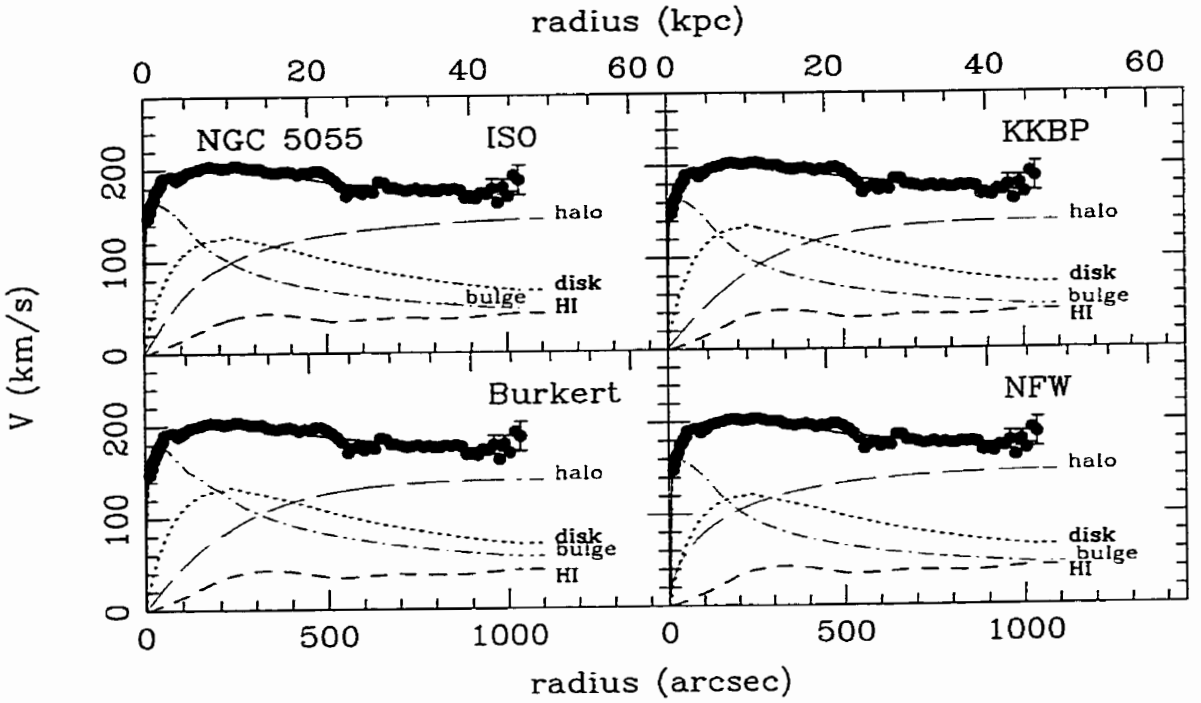

Figure 43: Mass model of NGC 5055

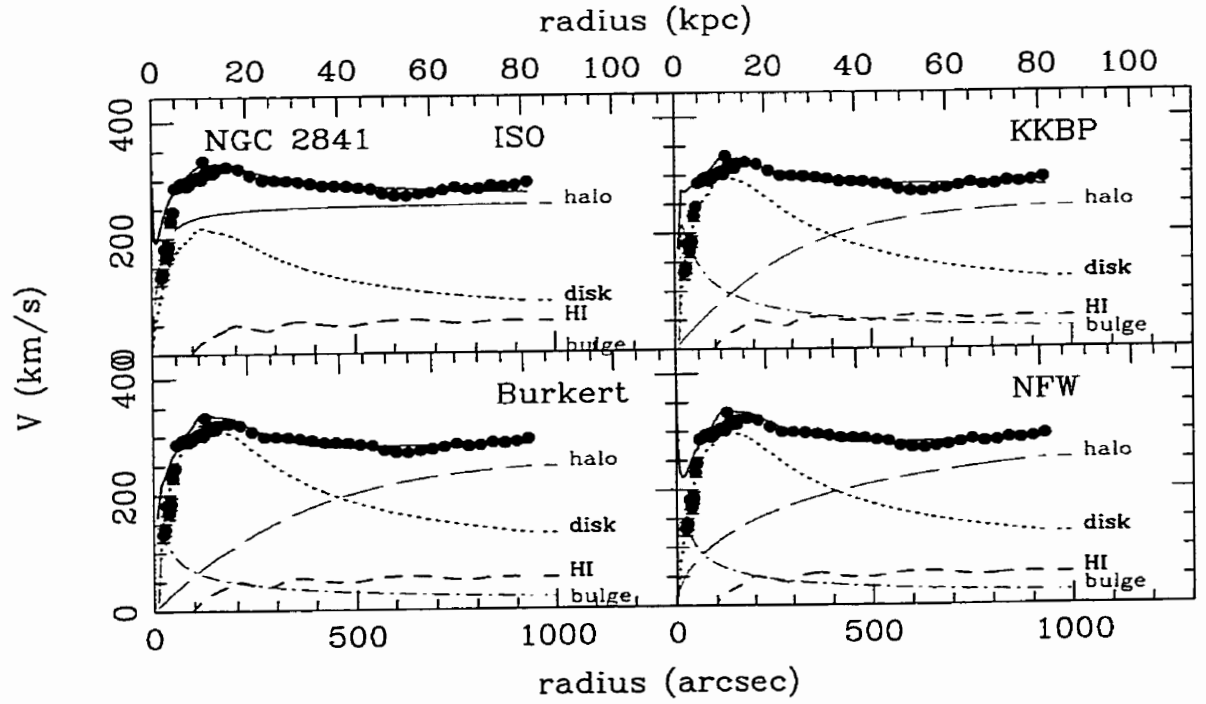

Figure 44: Mass model of NGC 2841

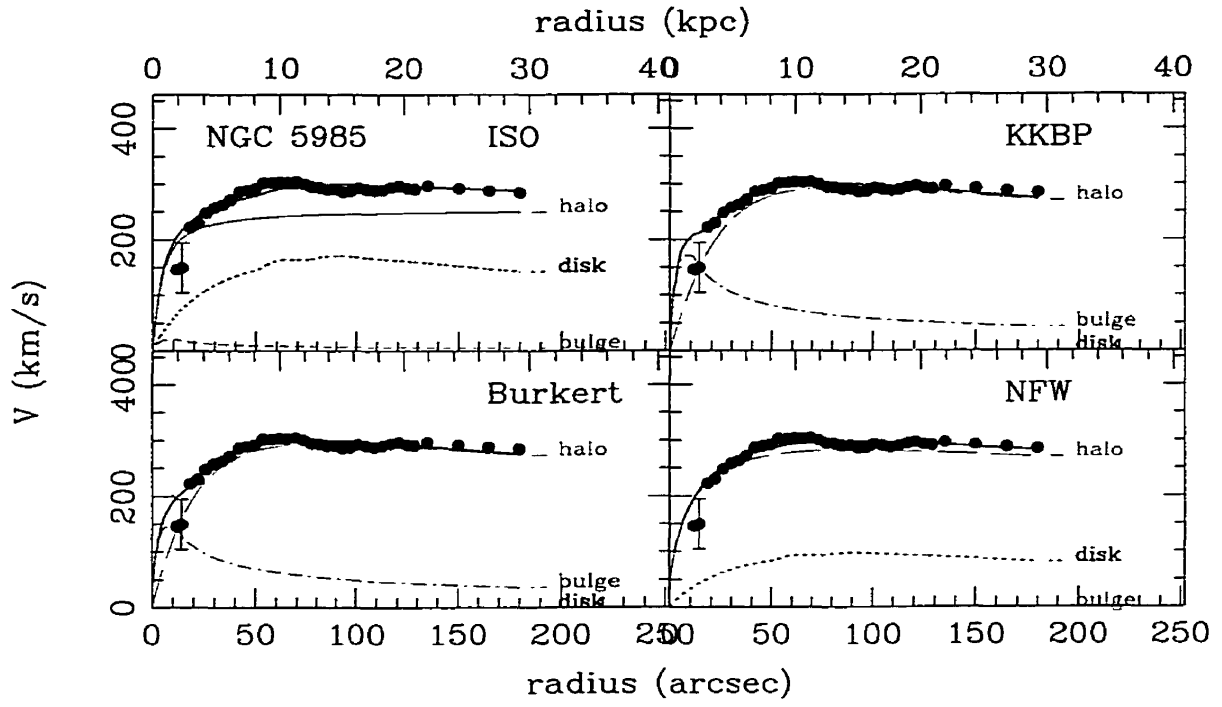

Figure 45: Mass model of NGC 5985

is especially true for the objects where the contribution of the bulge is not negligible. The rather simple approach taken here in regard of the light profile decomposition is not accurate enough to separate the disk and bulge contribution adequately. Ideally, one should do the decomposition simultaneously with the mass distribution fitting, taking the rotation curve and the light profile as constraints.

In addition to these models, the steepest cuspy profile compatible with each individual rotation curve (i.e. the maximum value of γ at 95% confidence level) is used to model each galaxy, including those from paper I and II. If the shallow profiles of dwarf galaxies are produced by matter ejection near the center, the ability of the process to destroy the central cusp should decrease with the central galactic potential well. This γ_{max} (plotted against the maximum velocity in Fig. 46) is thus expected to increase with the galaxy mass to eventually reach at least the value predicted by the N-body simulations.

As one can see, γ_{max} is very low for galaxies up to $V_{max} \simeq 100\,\mathrm{km\,s^{-1}}$. Moreover, the rotation curves of IC 2574 and NGC 3109 are still rising and their total mass could be higher. Unfortunately, no galaxy probes what seems to be a steep transition around V_{max}=110-120 $\mathrm{km\,s^{-1}}$. The low γ_{max} of NGC 5985 is more likely an artifact due to the use of the wrong distance (based on $H_0 = 75\ \mathrm{km\,s^{-1}\,Mpc^{-1}}$).

Table XIV: Parameters of the mass models

Model	Galaxy	Type	$(\mathcal{M}/L_B)_\star$ bulge	$(\mathcal{M}/L_B)_\star$ disk	r_0 kpc	ρ_0 $10^{-3}\mathcal{M}_\odot/pc^{-3}$	χ^2
ISO	UGC 2259	SBcd	no bulge	0.0	4.8	65.8	1.2
	NGC 2403	SABcd	no bulge	0.04	2.4	2.5	2.8
	NGC 6946	SABcd	no bulge	1.6	38.4	0.24	21
	NGC 5055	SABbc	3.2	2.3	6.3	1.2	31
	NGC 2841	SAb	0.0	2.7	1.1	98.5	96
	NGC 5985	SABb	0.1	3.7	0.7	274.0	76
Burkert	UGC 2259		no bulge	0.0	1.3	38.0	4.8
	NGC 2403		no bulge	2.5	8.6	1.7	6.1
	NGC 6946		no bulge	1.6	38.4	0.32	21
	NGC 5055		3.2	2.5	14.6	0.79	32
	NGC 2841		0.47	6.0	40.9	.34	91
	NGC 5985		5.2	0.0	4.16	43.2	38
KKBP	UGC 2259		no bulge	0.0	1.5	20.6	6.0
	NGC 2403		no bulge	2.5	9.3	1.0	6.1
	NGC 6946		no bulge	1.6	47.4	0.18	20
	NGC 5055		3.2	2.6	16.6	0.43	33
	NGC 2841		1.3	5.2	36.2	.28	128
	NGC 5985		7.1	0.0	4.9	21.7	42
NFW	UGC 2259		no bulge	0.0	3.3	5.7	4.2
	NGC 2403		no bulge	1.6	17.0	0.48	5.7
	NGC 6946		no bulge	1.3	38.4	0.12	20
	NGC 5055		2.95	2.06	28.2	0.23	33
	NGC 2841		0.52	5.4	134.0	0.041	89
	NGC 5985		0.0	1.2	6.7	15.2	50

r_0: core radius of the dark halo
ρ_0: central density of the dark halo

Such a low γ_{max} for a medium size galaxy like NGC 5585 is a challenge to the "feedback" theory. For $\gamma = 1$, van den Bosch et al. (2000) showed that one need a very efficient dark matter displacement by the baryonic expulsion, to destroy the central cusp in a $V_{200} \gtrsim 90$ galaxy.

5.3.2 MOND

The MOdified Newtonian Dynamics is often (Begeman et al., 1991), but not always (Broeils (1992), paper II) successful in describing rotation curves from the luminous matter alone. Even though this is a truly falsifiable theory, finding even a few galaxies with low enough uncertainties (especially on the distance determination) to rule out MOND is not obvious. Mass models of the galaxies from paper III are presented in Fig. 47 using MOND with both the value of $a_0 = 1.2 \times 10^{-10}$m s^{-2} from Begeman et al. (1991) and the a_0 that

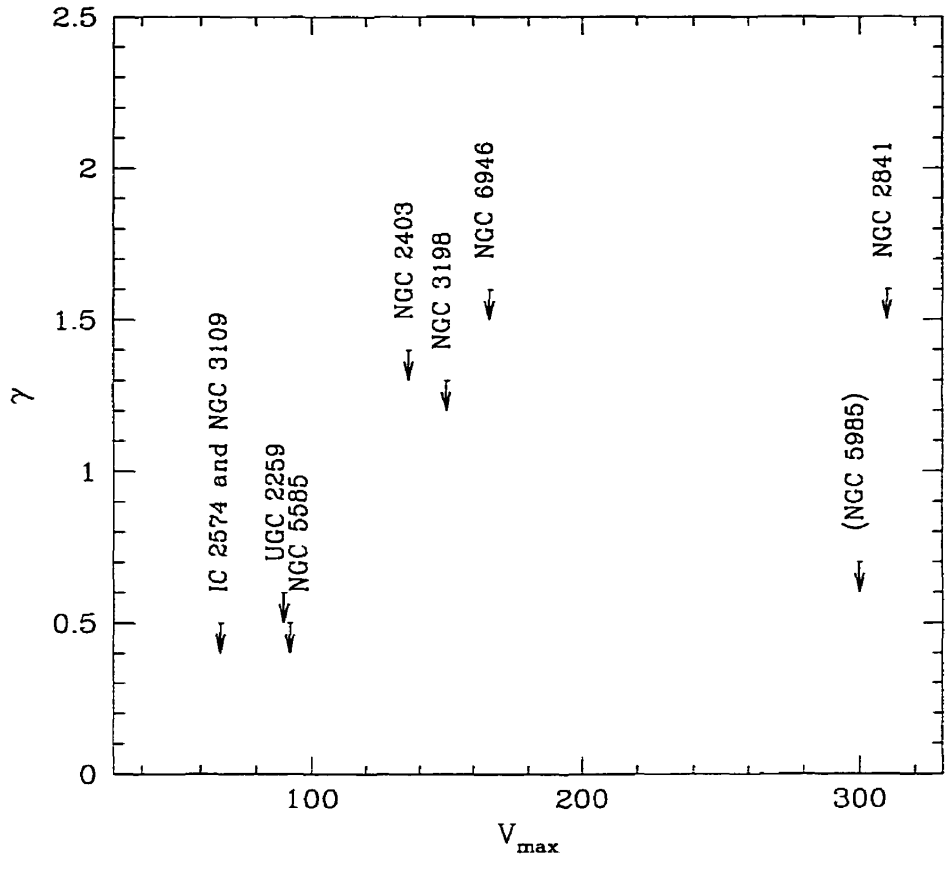

Figure 46: Permitted inner logarithmic slope (γ) of the CDM halos. Start of arrows give the maximum allowed value at a 95% confidence level. Note that most of the N-body simulations give $\gamma \geq 1$. NGC 5055 has a maximum γ well above 2.5 and is not plotted.

best fit each rotation curve (Table XV). One can see that UGC 2259, NGC 5985 and maybe NGC 5055 are not compatible with MOND. Nevertheless, these are not the galaxies with the best distance determination in the sample (only based on H_0=75 $\mathrm{km\,s^{-1}}$).

On the other hand, one strong prediction of MOND is the relation between the surface density and the surface brightness of the luminous disk. Indeed, since there is no dark matter, the acceleration is regulated by the surface mass density alone. Following McGaugh & De Blok (1998), the MOND characteristic surface density parameter ξ (Milgrom, 1983a) is plotted against the central surface brightness in Fig. 48. The scatter should only be related to the spread in $(\mathcal{M}/L_B)_\star$ ratios. A fit through the data gives a slope of -0.18 for a fixed value of a_0, compatible with the prediction of -0.20. In the middle panel, the best-fit value of a_0 is used and the slope drops to -0.32, a natural consequence of the tendency of the

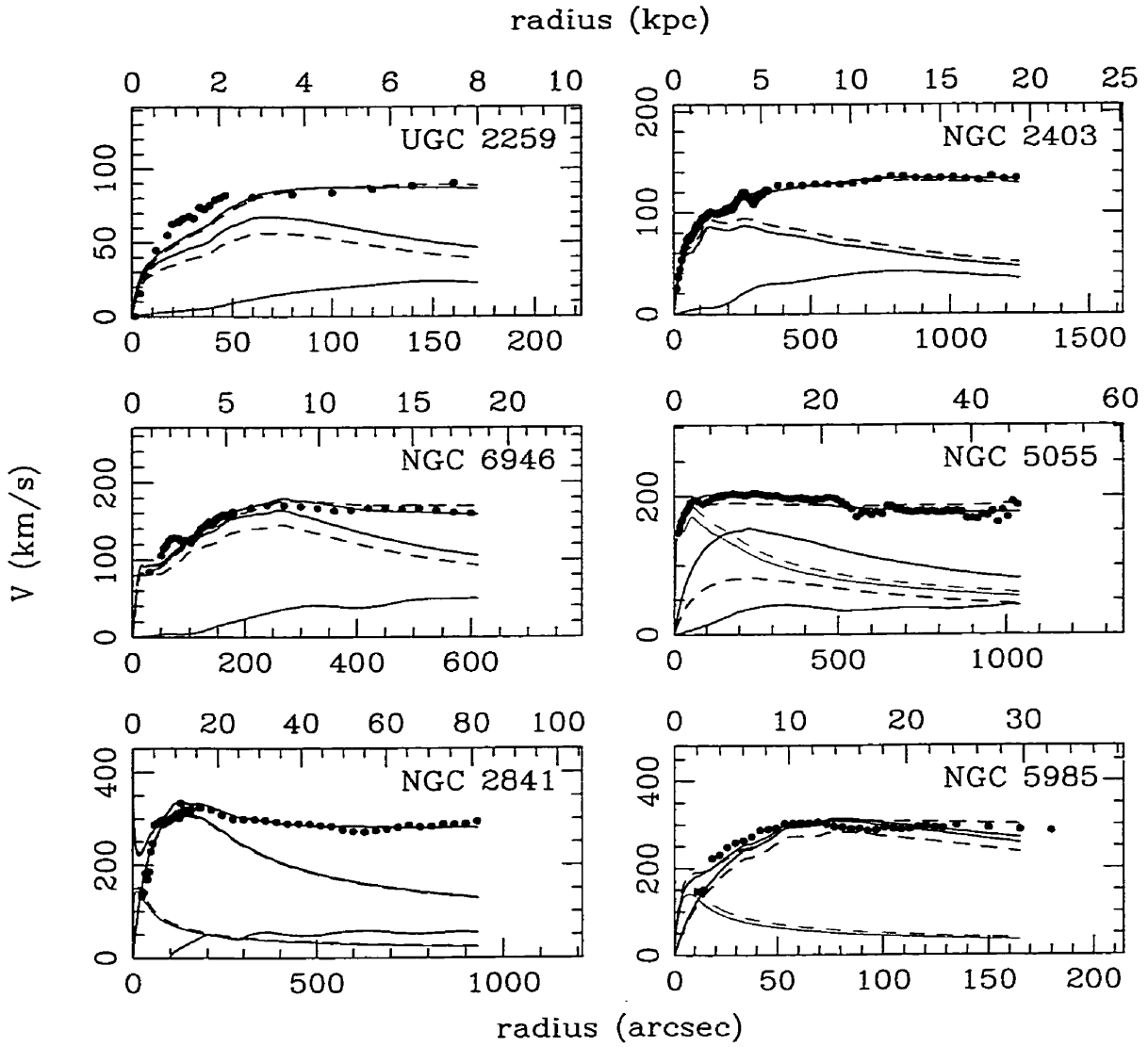

Figure 47: Mass models using MOND law with $a_0 = 1.2 \times 10^{-13}$ (dotted line) and best fit a_0 (continuous line). The Newtonian contributions of the disk, bulge and gas are represented in blue, cyan and green respectively.

Table XV: MOND parameters when using the best fitted a_0.

Galaxy	Distance Mpc	a_0 $\times 10^{-13}$ km/s^2	$(\mathcal{M}/L_B)_\star$ disk $\mathcal{M}_\odot/L_\odot$	$(\mathcal{M}/L_B)_\star$ bulge
UGC 2259	9.6	0.80	3.4	no bulge
NGC 2403	3.2	1.48	2.0	no bulge
NGC 6946	6.2	0.69	5.4	no bulge
NGC 5055	9.2	0.58	3.4	2.8
NGC 2841	18.0	1.22	5.7	3.1
NGC 5985	33.5	0.32	12.0	4.7

best-fit a_0 to increase for lower surface brightness galaxies (lower panel). This dependence of a_0 on the surface brightness is on clear contradiction of the MOND principle. However, the tight correlations shown in most of the MOND oriented studies are probably revealing some profound link between the total mass distribution and the luminous matter of galaxies.

5.4 Trends and Correlations

5.4.1 Halo Parameters

The standard cosmological theories predict that all halos should be well described by a two parameter family. The halos hierarchical formation can lead to some correlations between these parameters for a given cosmology but the detailed evolution should induce a fair amount of scatter (see for e.g. Bullock et al., 1999). However, claims have been made that a strong relation exists between these parameters and that only one could be sufficient to entirely describe the dark mass distribution of a galaxy (Burkert, 1995; Kravtsov et al., 1998). This parameter can be equivalently the central density, the core radius or the mass of the galaxy. All these studies used rotation curves affected to some extent by beam smearing or by the uncertainties of long–slit observations. In order to check the existence of such correlations in our limited but accurate sample, Fig. 49 shows ρ_o vs r_0 for all the galaxies and models.

As one can see, the two parameters do show a strong correlation and the scatter is only moderately larger than the observational uncertainties, probably less than expected from standard halos merging. The correlation coefficients are indicated for each model.

This also means that the core radius (r_0) increase with galaxy mass suggesting that self-interacting dark matter is not the cause of low density halo cores since you expect the opposite in this case (Dalcanton & Hogan, 2000).

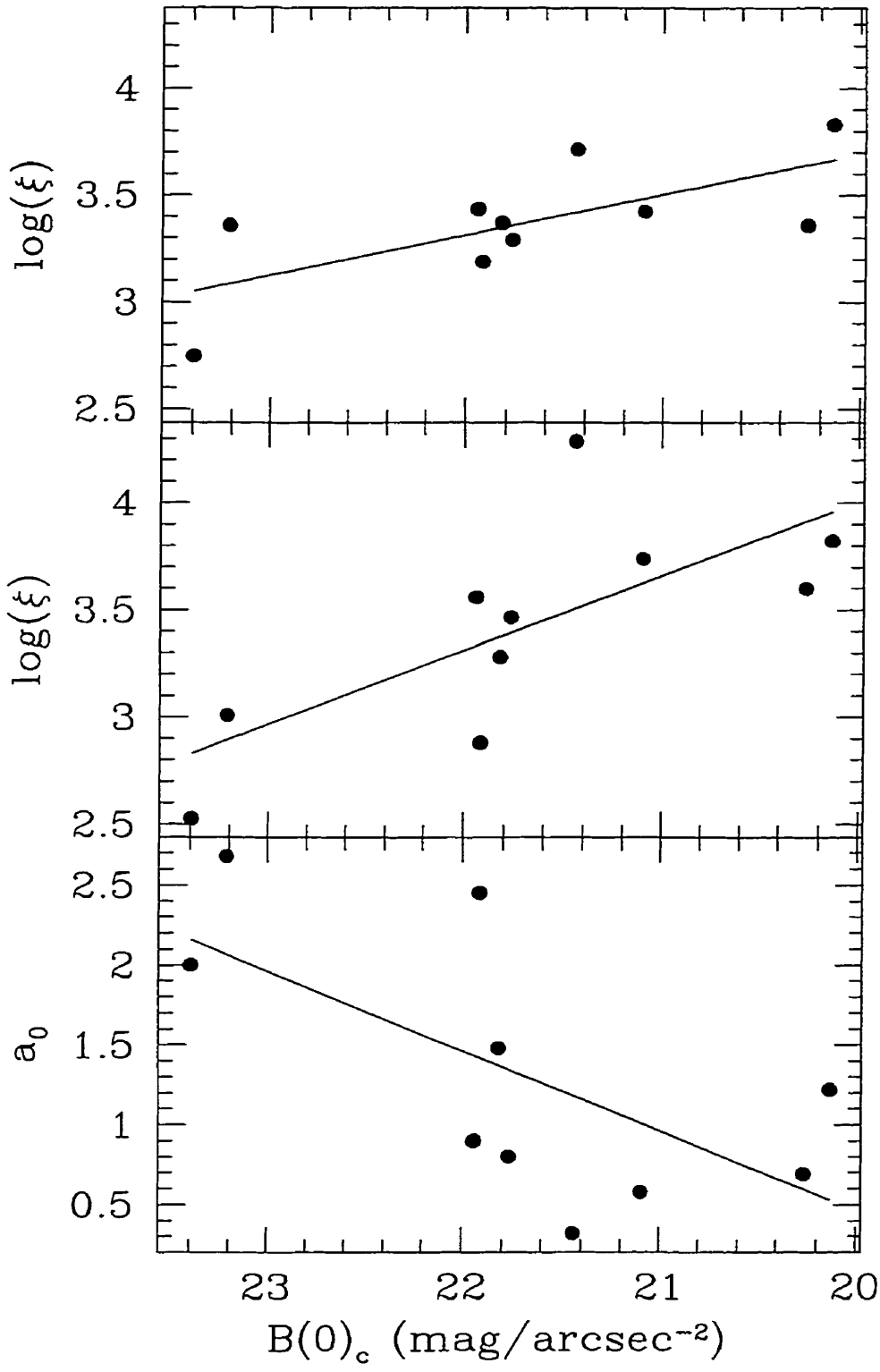

Figure 48: *Top:* MOND characteristic surface density ξ vs central surface brightness. a_0 is fixed at 1.2 $\times 10^{-10}$ m/s^2(Begeman et al., 1991); *middle:* same but the best fit value of a_0 is used; *bottom:* variation of the best fitted a_0 with the surface brightness.

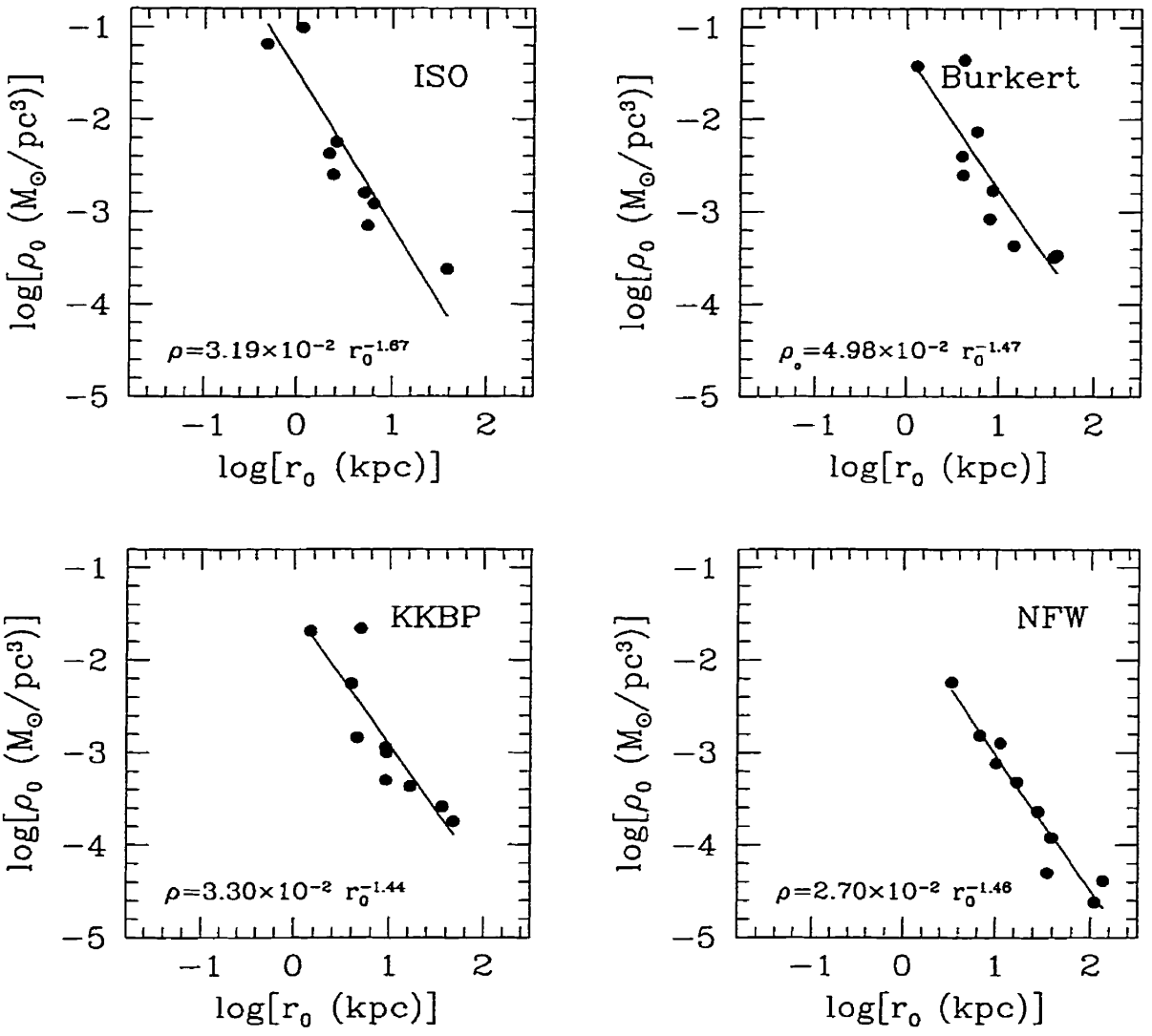

Figure 49: Characteristic (central) density (ρ_0) vs characteristic (core) radius (r_0), taken as the two "independent" parameters in the mass models.

5.4.2 Dark Matter vs Luminous matter

Even if a unique parameter could describe the CDM halos, it does not say much about the amount and distribution of luminous matter that should be embedded in these halos. If one could extend the above one parameter description not only to the dark halos but to the entire rotation curve (as in Persic et al., 1996), it would constrains the CDM+galaxy evolution to a very narrow class of scenarios. To investigate these possible links, the inner slope of the rotation curves, from the center to the turnover point, is plotted against the central surface brightness (top panel) and the absolute magnitude (bottom panel) in Fig. 50.

A clear correlation is seen in both cases, whereas the scatter gives ample room for some independence of the galaxy formation from the parent halo mass, but it is clear that the inner slope is proportional to $B(0)_c$ and/or to $-M_B$.

5.5 Discussion and Summary

As a first result, this study confirms the incompatibility between CDM N-body simulations and observations of latest type spiral galaxies. This includes the small Sc galaxy UGC 2259, often described as the smallest grand design spiral. On the other hand, more massive galaxies are compatible with any of the halo models studied here.

More precisely, when using well sampled, multiwavelength rotation curves, galaxies with a maximum rotational velocity $V_{max} \lesssim 90$ km s^{-1} have dark halos with an inner logarithmic slope $\gamma \lesssim 0.6$ which is significantly less than the standard N-body CDM simulations results ($\gamma \gtrsim 1$). Since no beam–smearing is present in the data, this result puts the standard CDM in some difficulties.

Besides involving new physics, very few scenarios can lead to such a behavior. Among them, a promising one is the destruction of the central density cusp by intense baryonic processes (van den Bosch et al., 2000). However, in order to create shallow density profiles in potential wells such as in NGC 5585, any baryonic process would need to be very efficient in dragging out the dark matter from the central part of the galaxy. It is interesting though to compare Fig. 8 of van den Bosch et al. (2000) to Fig. 46 shown here to see how similar the semi-analytical calculations and the observations behave.

On the other hand, a strong correlation is found between the two free parameters of the dark halos. For all the halo parametrizations, $\rho_0 = 2.7$ to $5.0 \times 10^{-2} \frac{\mathcal{M}_\odot}{pc^3 kpc} \times r_0^{-1.5}$ to $r_0^{-1.7}$. This is true even for low mass galaxies which is hard to understand if the central

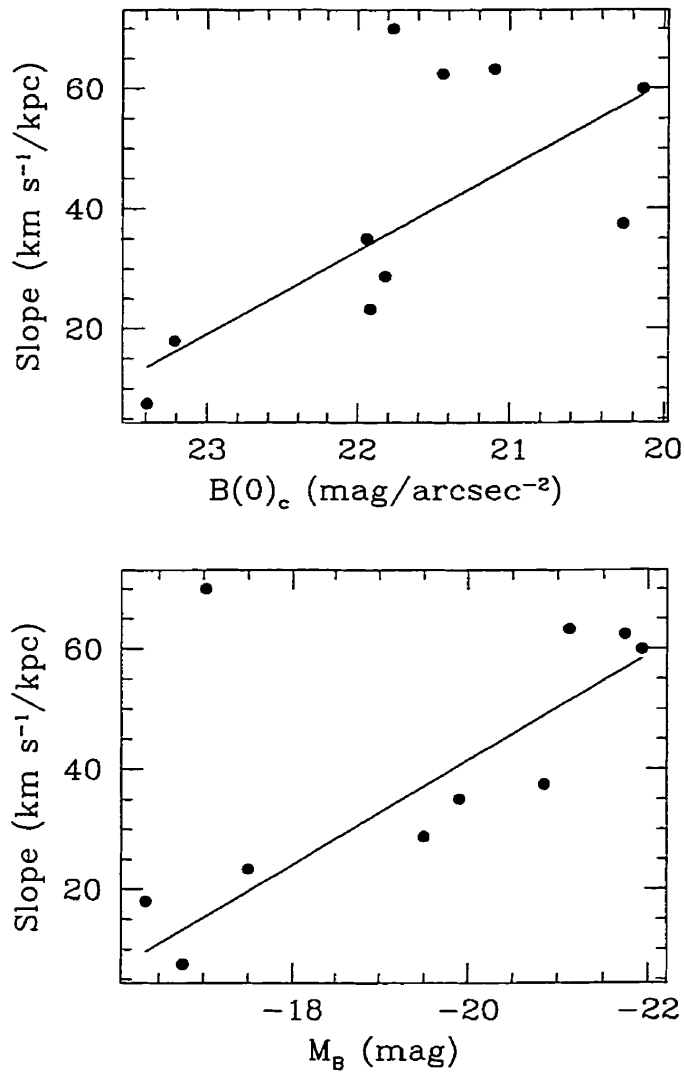

Figure 50: *Top:* the inner slope of the rotation curve vs surface brightness; *bottom:* the inner slope vs absolute magnitude

density is modified by baryonic agitation unless the latter is finely tuned to the parent halo mass.

This correlation also means that the core radius increases with mass, contrary to the expected $r_0 = 1/\sqrt{\sigma}$ from self-interacting dark matter (Dalcanton & Hogan, 2000).

The MOND law gives satisfactory fit for only half of the galaxies even if the "universal" constant a_0 is let free to vary. In this case, a_0 seems to be systematically higher for low surface brightness galaxies. Because of the composition of the sample, a_0 could instead possibly be related to the luminosity. In any case, this is in direct contradiction with the MOND prescription but reveals some underlying relations between the luminous matter and the parent halo characteristics. This is also suggested by the dependence of the inner slope of the rotation curves on the luminosity and surface brightness of galaxies.

5.6 Conclusion

In summary, the present study reaches these conclusions:

• The inner density slope is $\gamma \lesssim 0.6$ for galaxies with maximum rotational velocity $V_{max} \lesssim 90\,\mathrm{km\,s^{-1}}$.

• A strong correlation exists between the characteristic (core) radius and the characteristic (central) density of dark halos: $\rho_0 = 4\pm1 \times 10^{-2}(\frac{\mathcal{M}_{\odot} kpc^{1.5\pm0.1}}{pc^3}) \times r_0^{-1.5\pm0.1}$.

• The preceding conclusion also implies that the core radius grows with mass, contrarily to the expected $r_0 = 1/\sqrt{\sigma}$ from self-interacting dark matter.

• The inner slopes of rotation curves are related to the galaxy surface brightnesses (slope $(\mathrm{km\,s^{-1}}/\mathrm{kpc}) \propto -13B(0)_c(\mathrm{mag/arcsec^{-2}})$) and to galaxy luminosities (slope $(\mathrm{km\,s^{-1}}/\mathrm{kpc}) \propto -8.8M_B(\mathrm{mag})$).

• The MOND theory gives satisfying fits for only half of the present sample even using a "best-fitted" a_0. When doing so, a_0 decreases with surface brightness, in contradiction with MOND.

References

Aaronson, M. & Mould, J. 1983, ApJ, 265, 1

Begeman, K. 1987, PhD thesis, Rijksuniversiteit Groningen

Begeman, K. G., Broeils, A. H., & Sanders, R. H. 1991, MNRAS, 249, 523

Blais-Ouellette, S., Carignan, C., Amram, P., & Côté, S. 1999, AJ, 118, 2123

—. 2000a, AJ, submitted to AJ

—. 2000b, A&As, submitted to A&A supp.

Bosma, A. 1978, PhD thesis, Rijksuniversiteit Groningen

Broeils, A. 1992, PhD thesis, Rijksuniversiteit Groningen

Bullock, J., Kolatt, T., Sigad, Y., Somerville, R., Kravtsov, A., Klypin, A., J.R., P., & Dekel, A. 1999, astro-ph/9908159

Burkert, A. 1995, ApJ, 447, L25

Burkert, A. & Silk, J. 1997, ApJ,488, L55

Carignan, C., Charbonneau, P., Boulanger, F., & Viallefond, F. 1990, A&A, 234, 43

Carignan, C., Sancisi, R., & Van Albada, T. S. 1988, AJ, 95, 37

Corradi, R. L. M., Boulesteix, J., Bosma, A., Amram, P., & Capaccioli, M. 1991, A&A, 244, 27

Côté, S., Carignan, C., & Sancisi, R. 1991, AJ, 102, 904

Dalcanton, J. J. & Hogan, C. J. 2000, astro-ph/0004381

Freedman, W. L. 1990, ApJ, 355, L35

Fukushige, T. & Makino, J. 1997, ApJ, 477, L9

Jobin, M. & Carignan, C. 1990, AJ, 100, 648

Kaplinghat, M., Knox, L., & Turner, M. S. 2000, astro-ph/0005210

Kent, S. M. 1984, ApJS, 56, 105

Kent, S. M. 1987, A.J., 93, 816

Kravtsov, A. V., Klypin, A. A., Bullock, J. S., & Primack, J. R. 1998, ApJ, 502, 48

Martimbeau, N., Carignan, C., & Roy, J.-R. 1994, AJ, 107, 543

McGaugh, S. S. & De Blok, W. J. G. 1998, ApJ, 499, 41

Milgrom, M. 1983a, ApJ, 270, 371

—. 1983b, ApJ, 270, 365

More, B., Governato, F., Quinn, T., Stadel, J., & Lake, G. 1998, ApJ, 499, L5

Moriondo, G., Giovanardi, C., & Hunt, L. K. 1998, A&AS, 130, 81

Musella, I., Piotto, G., & Capaccioli, M. 1997, AJ, 114, 976

Navarro, J. F., Eke, V. R., & Frenk, C. S. 1996a, MNRAS, 283, L72

Navarro, J. F., Frenk, C. S., & White, S. D. M. 1996b, ApJ, 462, 563

—. 1997, ApJ, 490, 493

Persic, M., Salucci, P., & Stel, F. 1996, MNRAS, 281, 27

Puche, D., Westpfahl, D., Brinks, E., & Roy, J. R. 1992, AJ, 103, 1841

Sharina, M. E., Karachentsev, I. D., & Tikhonov, N. A. 1997, Pis ma Astronomicheskii Zhurnal, 23, 430

Sofue, Y., Tutui, Y., Honma, M., Tomita, A., Takamiya, T., Koda, J., & Takeda, Y. 1999, ApJ, 523, 136

Spergel, D. & Steinhardt, P. 1999, astro-ph/9909386

Swaters, R. 1999, PhD thesis, Rijksuniversiteit Groningen

Thornley, M. D. & Mundy, L. G. 1997, ApJ, 484, 202

van den Bosch, F. C., Robertson, B. E., Dalcanton, J. J., & de Blok, W. J. G. 2000, AJ, 119, 1579

Conclusion

Prenant l'exemple de la galaxie spirale NGC 5585, cette étude a d'abord montré le biais considérable de la basse résolution spatiale des observations radio sur la modélisation de la distribution de masse de cette galaxie. En effet, l'ajout de données Fabry-Perot de haute résolution a pour effet d'accentuer de façon importante la pente de la partie montante de la courbe de rotation. Cela permet une augmentation substantielle du ratio masse-luminosité du disque stellaire, modifiant grandement les importances relatives des composantes sombre et lumineuse. Ainsi, le ratio masse sombre–masse lumineuse diminue de près de 30% pour cette galaxie.

Après l'étude d'un échantillon d'une dizaine de galaxies, il apparaît clairement que la basse résolution spatiale, par le truchement de l'étalement du faisceau des observations à 21 cm, a un effet sur presque toutes les courbes de rotation. S'il était coutume de considérer comme fiables les observations dont le faisceau radio était plus petit que la longueur d'échelle, il est surprenant d'observer la correction importante apportée par les observations à haute résolution dans la plupart des cas étudiés. Le cas extrême est sans doute NGC 5055 pour laquelle le faisceau radio n'est que le huitième de la longueur d'échelle et où la pente interne de la courbe de rotation était clairement sous-évaluée par les données centimétriques. Par contre, l'impact de ces corrections sur la mesure de la distribution de masse demeure inégal. La sensibilité à la partie montante des courbes de rotation semble particulièrement aiguë pour les galaxies spirales tardives pour lesquelles la courbe de rotation est souvent trop à pic pour les observations radio mais dont la masse sombre reste importante dans les parties internes.

Un effort considérable a été fourni pour développer des outils originaux de traitement des données Fabry-Perot. Ainsi, les réflexions fantômes, les raies du ciel nocturne et surtout les variations photométriques en cours de nuit ont fait l'objet d'une étude poussée et leur traitement a réduit grandement les incertitudes qui leur sont généralement reliées

L'utilisation combinée des courbes de rotation composites (Fabry-Perot+radio)

et d'une paramétrisation malléable des halos sombres ont permis l'élaboration précise de modèles de masse dans les galaxies observées. Ils ont confirmé, en tout premier lieu, la difficulté de réconcilier les résultats des simulations de l'évolution cosmologique avec les observations des galaxies de faible masse. Il a été déterminé que les galaxies ayant une vitesse de rotation maximale $V_{max} \lesssim 100$ km s^{-1} possèdent des halos dont la pente logarithmique interne se limite à $\gamma \lesssim 0.6$. Cette valeur est bien au-dessous des valeurs prédites par les simulations numériques ($\gamma \gtrsim 1$). De plus, l'ampleur des puits de potentiel gravitationnel de ces galaxies rend difficile mais non impossible un "aplanissement" de la densité centrale par une éjection violente de matière baryonique.

L'observation d'une forte corrélation entre la densité centrale et le rayon caractéristique des halos mine quelque peu l'idée d'une perturbation des parties centrales par un processus baryonique. Peu importe le modèle utilisé, il semble que $\rho_0 = 4 \pm 1 \times 10^{-2} (\frac{\mathcal{M}_\odot kpc^{1.5\pm0.1}}{pc^3}) \times r_0^{-1.5\pm0.1}$ quelle que soit la masse de la galaxie. Il faudrait donc qu'un processus d'éjection centrale, qui ne peut avoir lieu que dans les galaxies de faible masse, réarrange le coeur des galaxies de façon à préserver exactement cette relation.

Par ailleurs, l'idée que la matière sombre ait une interaction collisionnelle non nulle avec elle-même n'est probablement pas la cause des faibles densités internes des galaxies. Cette théorie prédit en effet une proportionnalité inverse entre le rayon de coeur et la masse des galaxies, exactement à l'opposé des présents résultats.

La dynamique newtonienne modifiée (MOND) ne semble pas non plus être adéquate pour expliquer les courbes de rotation observées. Si cette loi de gravité permet une reproduction correcte de la moitié seulement des courbes de rotation de l'échantillon, c'est au prix de l'ajustement de la constante "universelle" a_0. Cette constante se doit d'être légèrement plus élevée pour les galaxies à faible brillance de surface en contradiction avec les fondements et l'universalité de cette théorie alternative. La quasi-réussite de MOND est toutefois un indice indéniable d'un lien profond entre les caractéristiques de la matière lumineuse et la distribution de la masse obscure. Cette relation est aussi suggérée par la corrélation entre la pente caractéristique des courbes de rotation et la luminosité (ou la brillance de surface) des galaxies de l'échantillon. Cette pente est fixée presque exclusivement par la matière lumineuse dans les galaxies massives alors qu'elle ne dépend que de la matière sombre pour les galaxies de faible masse.

Ce lien entre les composantes sombre et lumineuse pourrait bien être l'existence d'une composante non négligeable de masse sombre baryonique dont la distribution, possiblement isotherme, viendrait expliquer les densités constantes des centres galactiques tout

en laissant la possibilité d'un halo non-baryonique distribué selon les prédictions du modèle standard de la masse sombre froide. Malheureusement, les indications actuelles provenant des études de micro-lentilles gravitationelles tendent à montrer que la composante de MACHOs dans notre galaxie est insuffisante pour jouer un rôle dynamiquement *significatif*.

Fort de ces contraintes et à moins d'invoquer une modification en profondeur de notre compréhension de la masse et de l'inertie de la matière, il ne reste que peu de scénarios en lice pour expliquer les faibles densités au centre des galaxies peu massives. Il est toujours possible de troquer l'élégance d'un théorie simple et universelle pour une combinaison bien ajustée de multiples facteurs. Une composante modeste de MACHOs rendrait par exemple plus facile un phénomène d'éjection baryonique en rendant moins critique la surdensité centrale. Il est aussi possible qu'une solution simple ait été négligée ou oubliée. On peut entre autres se demander quel serait l'effet d'un gradient du ratio masse–luminosité dans les parties centrales du disque ou encore s'interroger sur l'impact d'un halo non sphérique.

Peu importe la créativité des solutions proposées, la clé demeurera toujours la disponibilité de données de qualité en quantité statistiquement suffisante. La combinaison des projets GHASP (Gassendi observations of Hα in SPiral galaxies) et WHISP (Westerbork observations of neutral Hydrogen in Irregular and SPiral galaxies), dont cette thèse était un avant-goût, permettra l'élaboration d'une base de données homogène de la cinématique de centaines de galaxies spirales. Cela s'avérera un outil précieux non seulement pour l'étude de la masse sombre mais aussi pour notre compréhension de la formation et de l'évolution des galaxies et, par le fait même, de notre univers.

Annexe A

Tableaux reportés

Table XVI: Optical rotation curve of NGC 5585 at 5″ binning

Radius ″	N_{app}	V_{app} km s^{-1}	N_{rec}	V_{rec} km s^{-1}	V_c km s^{-1}
2	27	10 ± 2	20	9 ± 2	11 ± 2
8	70	26 ± 1	59	25 ± 2	26 ± 1
12	104	33 ± 1	100	34 ± 1	33 ± 1
18	160	31 ± 1	99	33 ± 1	32 ± 1
22	198	33 ± 1	86	34 ± 1	33 ± 1
28	201	36 ± 1	100	32 ± 1	35 ± 2
32	195	40 ± 1	137	34 ± 1	37 ± 3
38	217	44 ± 1	173	38 ± 1	41 ± 3
42	211	44 ± 1	131	41 ± 1	43 ± 2
48	206	43 ± 1	125	46 ± 1	44 ± 1
52	194	46 ± 1	93	46 ± 1	46 ± 1
58	178	47 ± 1	103	45 ± 1	46 ± 1
62	193	46 ± 1	91	48 ± 1	46 ± 1
68	225	51 ± 1	54	45 ± 2	50 ± 3
72	270	57 ± 1	62	54 ± 2	56 ± 1
78	267	57 ± 1	72	53 ± 2	56 ± 2
82	285	61 ± 1	29	62 ± 2	61 ± 2
88	265	64 ± 1	6	43 ± 8	64 ± 6
92	288	66 ± 1	18	60 ± 4	66 ± 2
98	196	68 ± 1	70	62 ± 2	66 ± 3
102	86	71 ± 1	36	51 ± 4	67 ± 9

Table XVI *continued*

Radius $''$	N_{app}	V_{app} $km\,s^{-1}$	N_{rec}	V_{rec} $km\,s^{-1}$	V_c $km\,s^{-1}$
108	131	73 ± 1	17	55 ± 7	72 ± 7
112	105	72 ± 1	4	60 ± 2	72 ± 5
118	89	72 ± 1	37	61 ± 2	69 ± 5
122	86	74 ± 1	38	68 ± 3	73 ± 3
128	121	76 ± 1	48	59 ± 3	73 ± 8
132	179	73 ± 1	52	61 ± 1	70 ± 5
138	170	88 ± 1	62	65 ± 1	82 ± 1
142	160	87 ± 1	27	79 ± 1	86 ± 4
148	124	82 ± 1	56	77 ± 1	80 ± 2
152	72	84 ± 1	27	75 ± 2	81 ± 4
158	24	85 ± 1	113	76 ± 1	77 ± 4
162	44	82 ± 1	80	77 ± 1	79 ± 2
168	29	83 ± 1	35	79 ± 2	81 ± 2
172	1	86 ± 1	17	87 ± 2	87 ± 2
178	5	78 ± 5	67	77 ± 2	77 ± 2
182	12	90 ± 6	19	77 ± 3	82 ± 7
188	1	88 ± 1	20	79 ± 2	80 ± 5
192	0		30	80 ± 2	80 ± 2
198	0		13	73 ± 4	73 ± 4

*derived with $i = 52°$, $PA = 43°$

Table XVII: Optical rotation curve of NGC 3109 at 20″ binning from ROCUR. The two sides and the global rotational velocities are computed independently. The latter are corrected for asymetric drift.

R_{sides} ″	V_{app} km s^{-1}	V_{rec} km s^{-1}	R ″	V km s^{-1}
35	8 ± 1	3 ± 1	30	10 ± 2
65	6 ± 1		70	10 ± 1
95	15 ± 1		90	15 ± 1
			110	15 ± 1
125	14 ± 1		130	15 ± 1
155	22 ± 2		150	20 ± 1
			170	25 ± 1
185	25 ± 1		190	25 ± 1
215	26 ± 1		210	26 ± 1
			230	32 ± 1
245	32 ± 1		250	33 ± 1
275	34 ± 1	33 ± 1	270	37 ± 2
			290	35 ± 2
305	35 ± 1	32 ± 135	310	37 ± 2
335	39 ± 2	37 ± 1	330	39 ± 2
			350	41 ± 4
365	46 ± 6	40 ± 8	370	49 ± 10
395	52 ± 9	42 ± 4	390	47 ± 2
			410	48 ± 1
425	46 ± 2	45 ± 11		

*derived with $V_s = 402$ km s^{-1}

Table XVIII: Optical rotation curve of IC 2574 at 9.4″ binning from ADHOC. The two sides are computed independently and the total is their mean averaged by the number of points. The velocity dispersion and the number of points appear for both sides while the error is the two σ/N added in quadrature.

R arcsec	N_{app}	V_{app} km s^{-1}	σ_{ring} km s^{-1}	N_{rec}	V_{rec} km s^{-1}	σ_{ring} km s^{-1}	V km s^{-1}
8				2	22	8	22 ± 5
12				3	34	9	34 ± 5
15	22	8	20				8 ± 4
24	36	15	10	79	10	7	11 ± 1
33	26	12	12	81	3	27	5 ± 3
43	22	2	10				2 ± 2
52	62	10	15	144	3	22	5 ± 2
61	101	17	22	206	6	17	10 ± 2
70	139	27	24	228	9	16	16 ± 1
80	151	30	29	200	14	14	21 ± 2
89	113	42	37	202	16	16	25 ± 2
99	62	43	23	174	29	13	33 ± 2
108	75	33	23	157	30	16	31 ± 2
118	78	31	25	144	32	20	32 ± 2
127	72	33	27	137	31	19	32 ± 2
137	53	53	28	206	25	12	30 ± 2
146	40	66	26	423	26	9	30 ± 1
155	41	79	33	646	28	8	31 ± 1
165	45	54	40	739	31	13	32 ± 2
174	68	37	46	734	32	11	33 ± 2
183	81	25	18	712	34	10	33 ± 1
193	94	30	15	593	36	6	35 ± 1
202	102	31	22	510	36	8	35 ± 1
212	141	32	29	457	37	12	36 ± 1
221	193	34	24	410	40	13	38 ± 1
230	155	30	22	309	44	16	40 ± 1
240	147	42	34	418	48	12	47 ± 2
249	139	42	34	487	48	14	46 ± 1
259	185	43	28	497	46	15	45 ± 1
268	190	40	21	372	43	12	42 ± 1

Table XVIII *continued*

R arcsec	N_{app}	V_{app} km s^{-1}	σ_{ring} km s^{-1}	N_{rec}	V_{rec} km s^{-1}	σ_{ring} km s^{-1}	V km s^{-1}
278	138	44	23	234	40	21	41 ± 2
287	245	39	20	262	34	19	36 ± 1
296	287	44	13	258	34	28	39 ± 1
306	289	42	10	279	45	24	44 ± 1
314	279	38	11	218	42	23	40 ± 1
325	188	36	20	172	40	24	38 ± 2
334	347	37	20	195	45	31	40 ± 2
343	258	36	20	177	45	29	40 ± 2
352	159	40	13	183	47	27	44 ± 2
362	182	42	8	181	44	24	43 ± 1
372	327	44	15	175	46	23	45 ± 1
381	440	43	12	205	47	25	45 ± 1
390	255	40	18	217	53	28	46 ± 2
400	225	39	20	223	49	25	44 ± 2
409	162	41	29	291	52	26	48 ± 2
418	174	47	20	360	57	29	54 ± 1
428	162	50	42	424	60	32	57 ± 2
437	159	52	33	446	58	36	57 ± 2
446	171	46	31	367	55	27	52 ± 2
456	167	52	25	317	45	24	48 ± 2
466	173	55	23	343	48	28	51 ± 2
475	224	55	29	332	52	30	53 ± 2
484	240	59	45	339	54	28	56 ± 2
494	214	60	28	363	59	28	59 ± 2
503	171	64	36	434	60	22	61 ± 2
512	126	77	33	437	58	31	62 ± 2
522	96	70	15	504	59	37	61 ± 2
531	87	63	12	519	63	36	63 ± 2
540	85	73	32	511	62	37	64 ± 2
550	90	81	45	537	64	41	66 ± 2
559	65	71	30	505	65	39	66 ± 2
568	36	77	17	549	68	36	68 ± 2
578	17	85	25	553	64	35	65 ± 2
587	18	81	4	517	63	35	64 ± 2
595	3	79	4	433	55	42	55 ± 2

Table XVIII *continued*

R arcsec	N_{app}	V_{app} km s^{-1}	σ_{ring} km s^{-1}	N_{rec}	V_{rec} km s^{-1}	σ_{ring} km s^{-1}	V km s^{-1}
606				465	60	38	60 ± 2
616				496	67	36	67 ± 2
625				521	76	37	76 ± 2
634				531	79	35	79 ± 2
645	8	60	78	518	82	36	82 ± 4
653	19	101	75	513	82	41	82 ± 4
663				478	71	43	71 ± 2
672				476	70	36	70 ± 2
682				462	69	42	69 ± 2
691				465	78	38	78 ± 2
700				465	88	38	88 ± 2
710				460	87	39	87 ± 2
719				421	83	31	83 ± 1
728				348	85	29	85 ± 2
738				342	94	20	94 ± 1
747				323	94	20	94 ± 1
757				282	95	24	95 ± 1
766				280	93	25	93 ± 2
776				255	92	34	92 ± 2
785				268	97	33	97 ± 2
794				277	97	40	97 ± 2
803				215	99	46	99 ± 3
813				163	101	42	101 ± 3
823				115	110	32	110 ± 3
869				61	120	14	119 ± 2
877				24	103	12	102 ± 2

*derived with $V_s = 53$ km s^{-1}, i = 75 °, PA = 52°

Table XIX: Optical rotation curve of UGC 2259 at 2.6″ binning.

R arcsec	N_{app}	V_{app} $km\,s^{-1}$	σ_{ring} $km\,s^{-1}$	N_{rec}	V_{rec} $km\,s^{-1}$	σ_{ring} $km\,s^{-1}$	V $km\,s^{-1}$
1				5	0	28	0 ± 12
4				15	15	9	16 ± 2
6				17	28	13	28 ± 3
9				7	35	9	35 ± 3
12				15	45	15	45 ± 4
14				2	80	8	80 ± 5
17	14	55	5				55 ± 1
20	18	63	8				63 ± 2
23	16	64	10				64 ± 2
25	14	66	10				66 ± 3
28	41	68	12				68 ± 2
30	79	66	13				66 ± 1
33	80	74	14	6	73	10	74 ± 2
36	51	73	11	23	72	8	72 ± 2
38	57	78	12	53	72	6	75 ± 1
41	72	79	14	59	78	8	79 ± 1
44	92	81	13	74	80	9	80 ± 1
46	84	82	11	73	82	8	82 ± 1
49	65	83	9	51	87	5	85 ± 1
51	46	85	14	38	84	9	84 ± 2
54	45	86	14	24	79	10	84 ± 2
57	35	85	10	12	76	9	83 ± 2
59	25	74	12	13	68	6	72 ± 2
62	19	71	9	38	69	5	69 ± 1
64	7	75	5	41	69	6	70 ± 1
67				28	75	15	75 ± 3
69				15	76	16	76 ± 4

Table XX: Optical rotation curve of NGC 2403 at 6.6″ binning.

R arcsec	N_{app}	V_{app} km s^{-1}	σ_{ring} km s^{-1}	N_{rec}	V_{rec} km s^{-1}	σ_{ring} km s^{-1}	V km s^{-1}
10	49	29	13	48	21	9	25 ± 2
17	79	41	14	79	32	11	36 ± 1
23	116	45	15	116	43	15	44 ± 1
30	148	55	16	148	52	14	53 ± 1
36	178	67	18	179	56	15	62 ± 1
43	209	68	22	209	65	15	67 ± 1
50	251	75	23	251	72	16	73 ± 1
56	274	78	23	274	73	19	76 ± 1
63	312	77	20	312	76	20	76 ± 1
69	342	79	19	342	77	18	78 ± 1
76	361	83	17	375	78	14	80 ± 1
83	379	88	20	408	82	15	85 ± 1
89	425	91	19	441	86	15	88 ± 1
96	451	91	20	471	87	14	89 ± 1
102	479	94	15	506	90	18	92 ± 1
109	538	98	21	540	93	18	95 ± 1
116	576	96	20	574	93	19	95 ± 1
122	600	98	22	583	95	21	97 ± 1
129	629	102	19	598	97	22	99 ± 1
135	659	104	20	627	97	22	101 ± 1
142	695	103	19	651	96	19	100 ± 1
149	728	102	20	634	97	18	100 ± 1
155	762	100	20	610	100	16	100 ± 1
162	788	98	21	667	100	18	99 ± 1
168	806	98	20	711	102	19	100 ± 1
175	852	99	21	766	101	19	100 ± 1
182	870	98	20	779	103	18	100 ± 1
188	926	97	23	753	107	19	101 ± 1
195	918	98	23	690	108	22	102 ± 1
201	948	99	28	698	111	22	104 ± 1
208	949	98	30	661	111	20	103 ± 1
215	1010	98	30	656	111	20	103 ± 1

Table XX *continued*

R arcsec	N_{app}	V_{app} km s^{-1}	σ_{ring} km s^{-1}	N_{rec}	V_{rec} km s^{-1}	σ_{ring} km s^{-1}	V km s^{-1}
221	1069	101	28	644	112	22	105 ± 1
228	1084	106	23	600	115	21	109 ± 1
234	1076	109	24	510	118	22	112 ± 1
241	1150	110	23	462	124	21	114 ± 1
247	1204	112	26	321	132	25	116 ± 1
254	1133	116	28	304	136	21	120 ± 1
261	1089	116	30	291	134	20	120 ± 1
267	1058	115	30	236	128	20	118 ± 1
274	1127	114	31	163	127	24	115 ± 1
281	1130	112	30	158	127	23	114 ± 1
287	1032	110	27	202	118	21	112 ± 1
294	1009	107	24	182	114	18	108 ± 1
300	1085	110	23	208	118	18	111 ± 1
307	1043	113	24	264	121	15	115 ± 1
313	935	114	25	240	119	16	115 ± 1
320	1015	118	26	269	118	16	118 ± 1
327	1068	118	24	202	117	12	118 ± 1
333	1076	121	23	232	121	14	121 ± 1
340	833	122	25	201	124	12	123 ± 1
346	776	121	25	176	123	12	122 ± 1
353	853	120	24	159	124	18	120 ± 1
360	834	119	20	160	127	11	120 ± 1
366	789	119	23	148	128	11	121 ± 1
373	691	122	25	141	129	29	123 ± 1
380	640	120	25	116	141	10	123 ± 1
386	748	119	22	105	149	7	123 ± 1
393	725	118	23	142	153	13	124 ± 1
399	759	120	21	172	150	12	125 ± 1
406	620	122	29	166	145	17	126 ± 1
413	492	123	32	127	145	33	128 ± 2
419	485	125	29	106	143	33	128 ± 2
425	453	128	28	39	156	29	130 ± 2
433	307	128	26	11	115	2	127 ± 1
439	270	125	40	23	113	5	124 ± 2
444	281	118	45	2	109	0	118 ± 3

Table XX *continued*

R arcsec	N_{app}	V_{app} km s^{-1}	σ_{ring} km s^{-1}	N_{rec}	V_{rec} km s^{-1}	σ_{ring} km s^{-1}	V km s^{-1}
453	310	121	42	31	129	4	122 ± 2
459	318	128	29	40	131	4	129 ± 2
463				5	133	9	133 ± 4
465	304	134	29				134 ± 2
472	278	142	30				142 ± 2
478	220	147	33				147 ± 2
484	107	145	32				145 ± 3
490	15	114	16				114 ± 4
500	3	116	15				116 ± 9
506	66	133	35				133 ± 4
512	139	124	34				124 ± 3
518	170	128	29				128 ± 2
525	173	130	33				130 ± 2
531	148	126	34				126 ± 3
538	91	118	19				118 ± 2
545	96	125	19				125 ± 2
551	128	127	22				127 ± 2
558	152	135	25				135 ± 2
564	144	129	27				129 ± 2
571	130	135	28				135 ± 2
577	72	125	26				125 ± 3
584	18	117	21				117 ± 5
590	7	114	21				114 ± 8

Table XXI: Optical rotation curve of NGC 6946 at 4.4″ binning.

R arcsec	N_{app}	V_{app} $km\,s^{-1}$	σ_{ring} $km\,s^{-1}$	N_{rec}	V_{rec} $km\,s^{-1}$	σ_{ring} $km\,s^{-1}$	V $km\,s^{-1}$
7	70	103	28	66	110	71	107 ± 7
11	109	124	27	105	150	22	136 ± 2
15	156	141	27	113	126	34	135 ± 3
20	201	150	30	88	115	47	140 ± 3
24	243	139	33	76	84	56	126 ± 4
29	247	134	31	119	104	28	124 ± 2
33	184	128	39	151	131	41	129 ± 3
37	150	108	27	118	134	53	120 ± 4
42	155	96	33	71	146	52	112 ± 4
46	217	109	44	78	113	48	110 ± 4
51	292	108	46	96	97	62	106 ± 4
55	390	113	45	221	116	38	114 ± 2
59	428	120	38	301	117	28	119 ± 2
64	420	118	35	423	131	26	125 ± 1
68	449	118	38	421	138	20	128 ± 1
73	529	118	24	425	140	19	128 ± 1
77	626	117	25	419	144	19	128 ± 1
81	707	114	22	579	143	20	127 ± 1
86	682	111	23	615	138	22	124 ± 1
90	682	111	21	668	139	24	125 ± 1
95	652	113	26	674	137	21	125 ± 1
99	723	113	29	703	135	19	124 ± 1
103	635	111	26	553	135	22	122 ± 1
108	609	120	20	522	135	23	127 ± 1
112	598	128	18	561	134	22	131 ± 1
117	703	134	17	552	136	20	135 ± 1
121	661	139	18	649	142	17	141 ± 1
125	661	139	20	800	145	16	142 ± 1
130	700	143	20	925	148	19	146 ± 1
134	680	146	26	1016	150	29	149 ± 1
139	675	137	22	1052	150	24	145 ± 1
143	713	143	18	1068	148	23	146 ± 1

Table XXI *continued*

R arcsec	N_{app}	V_{app} $km\,s^{-1}$	σ_{ring} $km\,s^{-1}$	N_{rec}	V_{rec} $km\,s^{-1}$	σ_{ring} $km\,s^{-1}$	V $km\,s^{-1}$
147	668	147	17	1031	155	21	152 ± 1
152	661	152	15	924	157	32	155 ± 1
156	782	153	15	719	159	38	156 ± 1
161	807	155	14	706	162	36	158 ± 1
165	830	156	17	689	161	38	158 ± 1
169	863	155	18	684	156	35	155 ± 1
174	837	162	16	553	156	37	159 ± 1
178	706	164	18	495	160	42	162 ± 1
183	533	166	19	399	155	37	161 ± 1
187	408	171	21	430	154	30	162 ± 1
191	382	174	19	420	158	29	165 ± 1
196	396	176	17	309	161	26	169 ± 1
200	317	169	15	329	160	35	165 ± 2
205	235	171	14	342	164	23	167 ± 1
209	295	172	17	346	165	32	168 ± 1
213	312	175	16	429	172	20	174 ± 1
218	250	174	14	332	175	23	175 ± 1
222	193	172	13	504	163	38	165 ± 2
227	227	169	16	380	161	23	164 ± 1
231	272	180	20	411	160	27	168 ± 1
235	286	187	24	607	154	35	165 ± 1
240	344	188	27	471	156	26	169 ± 1
244	497	182	26	443	167	24	175 ± 1
249	572	177	34	542	163	24	170 ± 1
253	409	175	35	628	163	24	168 ± 1
257	270	178	32	743	168	24	170 ± 1
262	140	188	30	816	169	26	172 ± 1
266	154	206	44	797	163	31	170 ± 2
270	57	208	46	745	162	28	165 ± 2
275	19	238	15	675	158	30	160 ± 1
279				563	159	29	159 ± 1
284				469	162	30	162 ± 1
288				380	178	28	178 ± 1
292				283	183	30	183 ± 2
297				162	175	31	175 ± 2

Table XXI *continued*

R arcsec	N_{app}	V_{app} $km\,s^{-1}$	σ_{ring} $km\,s^{-1}$	N_{rec}	V_{rec} $km\,s^{-1}$	σ_{ring} $km\,s^{-1}$	V $km\,s^{-1}$
301				48	154	26	154 ± 26

Table XXII: Optical rotation curve of NGC 5055 at 2.2″ binning.

R arcsec	N_{app}	V_{app} km s^{-1}	σ_{ring} km s^{-1}	N_{rec}	V_{rec} km s^{-1}	σ_{ring} km s^{-1}	V km s^{-1}
3	38	69	95	37	31	80	50 ± 14
6	59	96	66	54	79	74	88 ± 9
8	88	145	23	80	126	42	136 ± 4
10	111	148	56	110	152	49	150 ± 5
12	136	159	26	133	151	43	155 ± 3
14	161	162	24	125	144	43	154 ± 3
17	187	168	18	184	154	31	161 ± 2
19	212	176	14	212	152	28	164 ± 2
21	238	183	14	238	154	26	168 ± 1
23	262	182	16	262	155	24	169 ± 1
25	283	178	17	282	163	22	171 ± 1
28	306	179	16	295	167	21	173 ± 1
30	342	183	15	337	169	20	176 ± 1
32	358	187	14	354	174	16	181 ± 1
34	383	190	12	383	179	15	184 ± 1
36	416	186	11	416	181	13	183 ± 1
39	435	184	9	435	182	14	183 ± 1
41	459	186	10	458	183	12	185 ± 1
43	488	190	10	486	183	10	186 ± 0
45	512	192	9	495	184	9	188 ± 0
47	527	193	10	478	187	12	190 ± 0
50	567	194	11	500	190	13	192 ± 1
52	584	196	12	512	194	15	195 ± 1
54	605	198	10	551	199	14	199 ± 0
56	624	198	10	577	203	12	200 ± 0
58	651	199	11	631	205	13	202 ± 0
60	658	200	12	639	208	17	204 ± 1
63	668	201	12	637	210	18	205 ± 1
65	697	202	12	668	208	16	205 ± 1
67	717	202	12	665	207	14	204 ± 1
69	747	204	12	604	204	16	204 ± 1
72	770	204	13	529	204	17	204 ± 1
74	785	202	13	592	204	21	203 ± 1

Table XXII *continued*

R arcsec	N_{app}	V_{app} km s^{-1}	σ_{ring} km s^{-1}	N_{rec}	V_{rec} km s^{-1}	σ_{ring} km s^{-1}	V km s^{-1}
76	828	197	12	627	205	21	201 ± 1
78	881	194	12	665	201	21	197 ± 1
80	876	194	12	651	201	18	197 ± 1
83	903	192	14	684	197	24	194 ± 1
85	934	194	9	699	196	24	195 ± 1
87	929	195	10	658	191	28	193 ± 1
89	912	196	10	624	191	28	194 ± 1
91	896	196	11	663	192	27	195 ± 1
93	843	196	10	651	188	28	193 ± 1
96	898	197	10	580	190	27	194 ± 1
98	941	197	10	702	187	32	193 ± 1
100	946	199	10	812	190	29	195 ± 1
102	966	200	11	850	193	28	197 ± 1
105	946	200	12	854	196	24	198 ± 1
107	922	199	11	904	195	29	197 ± 1
109	843	200	11	942	198	30	199 ± 1
111	916	200	11	900	201	29	201 ± 1
113	978	200	12	894	200	31	200 ± 1
115	1038	200	14	821	198	34	199 ± 1
118	1088	201	14	771	201	33	201 ± 1
120	1112	203	13	794	202	33	203 ± 1
122	1170	204	13	801	205	29	204 ± 1
124	1266	204	14	880	203	31	204 ± 1
127	1304	203	14	951	207	26	205 ± 1
129	1338	202	14	960	210	24	206 ± 1
131	1403	204	13	874	212	25	207 ± 1
133	1425	206	14	700	206	33	206 ± 1
135	1369	207	16	680	207	32	207 ± 1
137	1301	207	16	655	208	31	207 ± 1
140	1247	207	16	630	212	22	209 ± 1
142	1233	206	16	685	213	21	209 ± 1
144	1165	206	16	667	210	26	207 ± 1
146	1153	207	16	605	206	30	207 ± 1
149	1125	207	16	658	204	31	206 ± 1
151	1089	204	16	711	202	28	203 ± 1

Table XXII *continued*

R arcsec	N_{app}	V_{app} km s^{-1}	σ_{ring} km s^{-1}	N_{rec}	V_{rec} km s^{-1}	σ_{ring} km s^{-1}	V km s^{-1}
153	1141	203	15	612	202	28	202 ± 1
155	1202	203	17	587	204	25	203 ± 1
157	1173	204	16	545	205	24	204 ± 1
160	1134	204	14	555	204	23	204 ± 1
162	1043	206	12	516	201	25	204 ± 1
164	1018	208	13	660	202	25	205 ± 1
166	957	209	12	635	203	21	207 ± 1
168	983	210	12	608	206	18	209 ± 1
171	1007	212	12	558	207	20	210 ± 1
173	993	211	12	550	204	17	209 ± 1
175	979	208	12	617	204	18	207 ± 1
177	860	209	11	652	201	27	205 ± 1
179	747	208	10	627	200	30	205 ± 1
181	693	209	11	568	196	33	203 ± 1
184	661	209	13	525	196	32	203 ± 1
186	644	207	13	512	197	28	202 ± 1
188	534	208	13	506	197	31	202 ± 1
190	522	215	15	535	201	28	208 ± 1
192	533	213	32	599	207	26	210 ± 1
195	474	216	22	613	212	19	214 ± 1
197	487	218	12	591	216	19	217 ± 1
199	410	216	14	668	216	18	216 ± 1
201	332	208	11	693	216	18	213 ± 1
204	314	207	14	655	213	20	211 ± 1
206	334	208	15	585	211	20	210 ± 1
208	349	205	17	452	208	23	206 ± 1
210	250	205	15	277	205	29	205 ± 1
212	197	203	19	222	202	29	203 ± 2
215	232	208	16	236	209	25	209 ± 1
217	208	206	21	263	204	21	205 ± 1
219	92	208	13	314	203	20	204 ± 1
221	68	215	6	348	212	25	212 ± 1
223	56	212	12	376	215	27	215 ± 1
225	58	213	12	319	210	30	210 ± 2
227	13	227	33	239	206	31	207 ± 3

Table XXII *continued*

R arcsec	N_{app}	V_{app} $km\,s^{-1}$	σ_{ring} $km\,s^{-1}$	N_{rec}	V_{rec} $km\,s^{-1}$	σ_{ring} $km\,s^{-1}$	V $km\,s^{-1}$
232	25	170	51	222	211	24	207 ± 4
234	50	183	54	142	221	20	211 ± 4
236	5	171	33	76	215	17	212 ± 4
239	39	190	6	68	211	23	203 ± 2
241	32	192	14	48	219	28	208 ± 3
243	51	195	5	2	237	52	197 ± 7
245	38	190	53	49	225	46	210 ± 8
247	9	168	22	172	242	27	238 ± 3
250	26	189	31	193	239	14	233 ± 2
252	33	210	28	115	238	18	231 ± 3
254	5	222	4	126	252	27	251 ± 2
256	37	215	9	116	247	23	239 ± 2
258	102	201	22	58	243	27	216 ± 3
261	162	195	23	58	247	42	209 ± 3
263	133	199	31	42	256	46	213 ± 4
265	140	202	32	12	254	59	206 ± 5
267	135	207	30	3	262	3	208 ± 3
270	89	217	21	2	144	244	215 ± 26
272	91	215	16	2	241	3	216 ± 2
274	98	219	20	8	242	7	221 ± 2
276	102	218	19	4	248	2	219 ± 2
280	123	197	32	17	234	16	202 ± 3
282	195	185	40	31	228	18	191 ± 3
284	249	186	40	24	218	11	189 ± 2
286	226	181	32	6	135	96	180 ± 7
288	159	169	25	5	135	98	168 ± 8
290	119	165	27	22	204	51	171 ± 5
293	106	166	26	10	140	48	163 ± 5
295	105	172	28	13	101	47	164 ± 5
297	87	173	38	36	138	13	163 ± 4
299	54	170	22	42	151	13	162 ± 3
301	44	162	16	60	154	28	158 ± 3
304	57	163	14	52	154	18	159 ± 2
306	56	171	13	45	150	16	161 ± 2
308	23	171	12	29	136	17	152 ± 3

Table XXII *continued*

R arcsec	N_{app}	V_{app} $km\,s^{-1}$	σ_{ring} $km\,s^{-1}$	N_{rec}	V_{rec} $km\,s^{-1}$	σ_{ring} $km\,s^{-1}$	V $km\,s^{-1}$
310	4	164	4	7	116	17	134 ± 5
314	1	137	0	10	182	18	178 ± 5
316	10	147	27	12	176	7	163 ± 6
318	26	148	12	14	179	18	159 ± 4
320	30	152	9	34	172	14	163 ± 2
322	44	187	59	29	178	16	183 ± 7
324	28	209	57	21	184	16	198 ± 8
329	3	153	2	42	176	17	175 ± 3
331	7	154	8	53	167	19	166 ± 3
333	1	164	0	29	152	21	152 ± 4
333				21	149	9	149 ± 2
336				3	134	13	134 ± 8
338				16	158	16	158 ± 4
340				32	171	12	171 ± 2
342				26	164	11	164 ± 2
343				4	153	23	153 ± 11

Table XXIII: Optical rotation curve of NGC 2841 at 4.4″ binning.

R arcsec	N_{app}	V_{app} $km\,s^{-1}$	σ_{ring} $km\,s^{-1}$	N_{rec}	V_{rec} $km\,s^{-1}$	σ_{ring} $km\,s^{-1}$	V $km\,s^{-1}$
24	14	133	46				133 ± 12
28	13	134	59	41	143	37	141 ± 9
33	30	184	98	18	180	61	183 ± 17
38	40	167	55	8	184	52	170 ± 11
43	30	180	44	20	195	53	186 ± 10
48	72	246	70	52	207	62	230 ± 8
53	136	244	54	57	253	57	247 ± 6
58	214	290	102	65	279	68	287 ± 7
63	244	288	85	93	289	49	289 ± 5
68	274	287	38	97	299	58	290 ± 4
72	268	296	46	93	292	69	295 ± 4
77	304	297	31	91	289	72	295 ± 4
82	242	298	36	75	277	75	293 ± 5
88	269	294	27	71	280	65	291 ± 4
92	395	298	51	89	272	74	293 ± 4
97	425	298	44	59	287	57	297 ± 3
103	464	302	31	49	281	86	300 ± 4
107	444	308	41	78	278	91	303 ± 4
112	420	305	45	57	307	78	305 ± 4
118	392	304	43	58	306	84	304 ± 4
123	420	306	34	92	280	110	301 ± 5
128	374	336	137	71	319	74	334 ± 7
132	342	315	50	90	301	89	312 ± 5
138	399	326	88	78	278	92	318 ± 6
142	381	312	35	63	311	84	312 ± 4
148	294	319 4	8	51	311	89	318 ± 5
152	331	317	40	74	294	74	312 ± 4
157	257	319 2	3	67	323	64	320 ± 4
162	170	336	77	43	331	60	335 ± 7
167	115	341	58	42	320	80	336 ± 8
172	49	325	56	48	285	111	305 ± 13
177	33	348	49	52	277	54	305 ± 8
183	28	363	36	45	283	73	314 ± 10

Table XXIII *continued*

R arcsec	N_{app}	V_{app} $km\,s^{-1}$	σ_{ring} $km\,s^{-1}$	N_{rec}	V_{rec} $km\,s^{-1}$	σ_{ring} $km\,s^{-1}$	V $km\,s^{-1}$
187	30	368 3	8	46	255	94	299 ± 12
191	2	422	8	47	241	146	249 ± 21
197				31	329	115	329 ± 21

Table XXIV: Optical rotation curve of NGC 5985 at 4″ binning.

R arcsec	N_{app}	V_{app} km s^{-1}	σ_{ring} km s^{-1}	N_{rec}	V_{rec} km s^{-1}	σ_{ring} km s^{-1}	V km s^{-1}
12	1	146	0				146 ± 0
14	6	197	20	10	121	179	150 ± 45
18	11	223	34	32	222	37	223 ± 8
22	29	233	44	43	228	27	230 ± 6
26	73	250	38	43	246	31	248 ± 5
30	82	265	28	44	244	29	258 ± 4
34	89	270	17	38	247	36	263 ± 4
38	89	274	24	33	267	60	272 ± 6
42	105	287	22	36	286	42	287 ± 4
46	125	293	16	29	272	57	289 ± 5
49	134	298	27	45	273	25	292 ± 3
53	147	312	31	45	272	25	302 ± 3
58	155	313	49	60	275	24	302 ± 4
61	169	319	50	104	279	29	304 ± 3
65	141	318	33	88	278	38	303 ± 3
69	130	320	32	89	283	46	305 ± 4
73	112	315	30	93	282	40	300 ± 3
77	125	313	39	117	276	31	295 ± 3
81	108	301	45	109	287	28	294 ± 4
85	82	298	50	103	284	33	290 ± 4
89	86	292	45	113	290	35	291 ± 4
93	102	283	37	116	288	31	286 ± 3
97	141	284	34	92	292	37	287 ± 3
101	169	292	27	63	298	39	294 ± 3
105	160	288	29	55	297	34	290 ± 3
109	153	289	33	64	287	30	288 ± 3
113	124	295	30	45	275	43	290 ± 4
117	128	296	29	36	291	46	294 ± 4
121	108	298	22	26	294	43	297 ± 4
125	91	296	22	29	283	33	293 ± 4
129	93	294	36	14	275	25	291 ± 4
133	93	304	18	19	295	31	303 ± 3

Table XXIV *continued*

R arcsec	N_{app}	V_{app} $km\,s^{-1}$	σ_{ring} $km\,s^{-1}$	N_{rec}	V_{rec} $km\,s^{-1}$	σ_{ring} $km\,s^{-1}$	V $km\,s^{-1}$
137	85	309	24	20	289	30	305 ± 4
140	76	322	37	15	284	18	316 ± 4
144	21	296	52	10	282	13	291 ± 10
148	9	276	36	6	272	10	275 ± 10
76	18	290	43				290 ± 10
78	21	314	14				314 ± 3
80	17	296	64				296 ± 16
82	30	310	13				310 ± 2
164	19	303	17				303 ± 4
168	4	275	10				275 ± 5

Table XXV: HI rotation curve of NGC 5985 at $\sim 10''$ binning ($30''$ resolution).

R arcsec	N_{app}	V_{app} km s^{-1}	σ_{ring} km s^{-1}	N_{rec}	V_{rec} km s^{-1}	σ_{ring} km s^{-1}	V km s^{-1}
15	2	124	33				124 ± 24
23	2	189	4	2	71	2	130 ± 2
34	3	170	20				170 ± 11
43	5	210	45				210 ± 20
53	5	272	34	5	276	104	274 ± 35
62	6	300	45	6	277	80	288 ± 26
74	9	287	40	9	291	88	289 ± 23
84	8	310	59	8	303	54	306 ± 20
94	9	289	33	9	310	79	300 ± 20
103	9	293	23	9	306	57	300 ± 14
114	12	297	23	12	312	63	304 ± 14
124	12	299	14	12	314	49	307 ± 10
134	14	300	16	14	236	190	268 ± 36
144	13	301	12	13	288	49	295 ± 10
154	16	307	16	16	266	147	287 ± 26
165	17	299	35	17	292	59	296 ± 12
175	17	252	204	17	284	58	268 ± 36
184	17	284	64	16	271	34	278 ± 13
194	19	253	182	19	264	65	258 ± 31
204	20	229	192	20	263	69	246 ± 32
214	19	251	126	21	271	62	261 ± 22
225	13	227	156	21	261	70	248 ± 29
235	6	281	26	20	246	73	254 ± 15
245	3	286	15	19	245	95	251 ± 20
256	1	165	0	14	266	94	260 ± 24
265	4	255	102	13	299	94	289 ± 34
274	3	234	109	13	292	110	281 ± 39
285	4	219	89	8	347	81	304 ± 35
297	4	177	8	6	336	109	272 ± 35
306	2	178	8	5	332	90	288 ± 34
317	1	189	0	5	306	32	286 ± 13
				5	294	7	294 ± 3

Table XXV *continued*

R arcsec	N_{app}	V_{app} km s^{-1}	σ_{ring} km s^{-1}	N_{rec}	V_{rec} km s^{-1}	σ_{ring} km s^{-1}	V km s^{-1}
				4	295	8	295 ± 4
				1	287	0	287 ±0
				1	362	0	362 ±0
				2	367	10	367 ± 7
				2	380	12	380 ± 8
				1	402	0	402 ± 0
				2	408	13	408 ± 9
				3	413	19	413 ± 11
				4	400	22	400 ± 11
				6	383	27	383 ± 11
				6	380	26	380 ± 11
				5	370	20	370 ± 9
				5	368	19	368 ± 9
				5	366	18	366 ± 8
				4	381	17	381 ± 8
				3	385	13	385 ± 8
				2	389	9	389 ± 7
				3	393	14	393 ± 8
				3	404	14	404 ± 8
				2	407	10	407 ± 7
				1	411	0	411 ± 0